

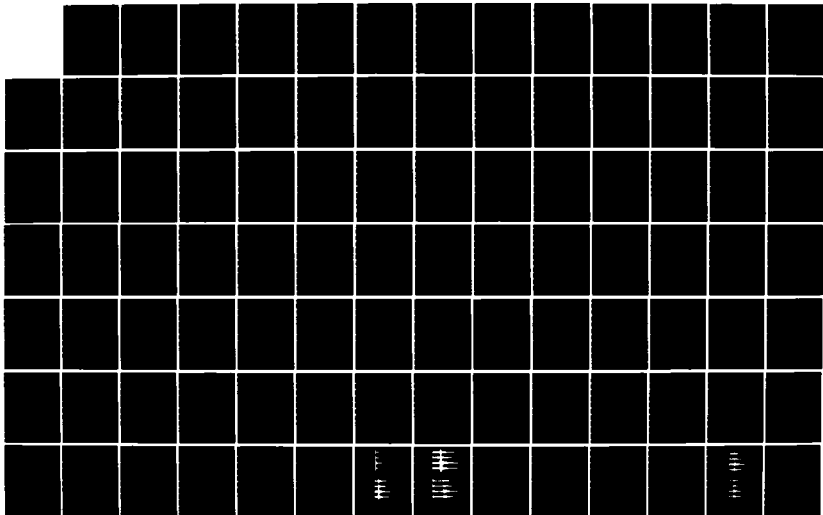
AD-A148 284

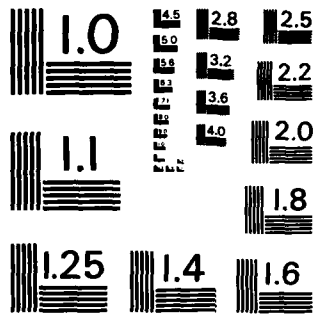
EFFECTS OF HETEROGENEITIES ON THE PROPAGATION
SCATTERING AND ATTENUATION O. (U) MASSACHUSETTS INST OF
TECH CAMBRIDGE EARTH RESOURCES LAB K AKI ET AL.
30 JUN 84 AFOSR-TR-84-1023 F49620-83-C-0038 F/G 8/11

1/2

UNCLASSIFIED

NL





MICROCOPY RESOLUTION TEST CHART
NATIONAL BUREAU OF STANDARDS-1963-A

UNCLASSIFIED
SECURITY CLASSIFIC.

AD-A148 284

6

1a. REPORT SECURITY CLASSIFICATION UNCLASSIFIED		1b. RESTRICTIVE MARKINGS	
2a. SECURITY CLASSIFICATION AUTHORITY		3. DISTRIBUTION/AVAILABILITY OF REPORT Approved for public release; distribution unlimited.	
2b. DECLASSIFICATION/DOWNGRADING SCHEDULE		5. MONITORING ORGANIZATION REPORT NUMBER(S) AFOSR-TR-84-1023	
4. PERFORMING ORGANIZATION REPORT NUMBER(S)		7a. NAME OF MONITORING ORGANIZATION AFOSR/NP	
6a. NAME OF PERFORMING ORGANIZATION Massachusetts Institute of Technology	6b. OFFICE SYMBOL (If applicable)	7b. ADDRESS (City, State and ZIP Code) Building 410 Bolling AFB, DC 20332-6448	
6c. ADDRESS (City, State and ZIP Code) Earth Resources Lab Dept of Earth, Atmospheric & Planetary Sciences Cambridge, Massachusetts 02139		9. PROCUREMENT INSTRUMENT IDENTIFICATION NUMBER F49620-83-C-0038	
8a. NAME OF FUNDING/SPONSORING ORGANIZATION Advanced Research Projects Agency	8b. OFFICE SYMBOL (If applicable)	10. SOURCE OF FUNDING NOS.	
8c. ADDRESS (City, State and ZIP Code) 1400 Wilson Boulevard Arlington, VA 22-09		PROGRAM ELEMENT NO. 61101E	PROJECT NO. 2309
11. TITLE (Include Security Classification) EFFECTS OF HETEROGENEITIES ON THE PROPAGATION, SCATTERING & ATTENUATION OF SEISMIC WAVES & THE CHARACTERIZATION OF SEISMIC SOURCE		TASK NO. A1	WORK UNIT NO.
12. PERSONAL AUTHOR(S) Drs Keiiti Aki, Vernon F. Cormier & M. Nafi Toksoz			
13a. TYPE OF REPORT SEMI-ANNUAL	13b. TIME COVERED FROM 1 Jan 84 to 30 Jun 84	14. DATE OF REPORT (Yr., Mo., Day) 30 Jun 84	15. PAGE COUNT 105
16. SUPPLEMENTARY NOTATION			
17. COSATI CODES		18. SUBJECT TERMS (Continue on reverse if necessary and identify by block number)	
FIELD	GROUP	SUB. GR.	
19. ABSTRACT (Continue on reverse if necessary and identify by block number) This study has examined the attenuation of local/regional S codas from 0.25 Hz to Hz in the Hindu Kush region. A goal study was to separate the relative contribution of scattering versus intrinsic anelasticity to the attenuation of coda waves. Coda attenuation has been analyzed in the frequency domain using a radiative transfer equation technique, which includes multiple scattering, and in the time domain using weak and strong scattering approximations.			
20. DISTRIBUTION/AVAILABILITY OF ABSTRACT UNCLASSIFIED/UNLIMITED <input checked="" type="checkbox"/> SAME AS RPT. <input type="checkbox"/> DTIC USERS <input type="checkbox"/>		21. ABSTRACT SECURITY CLASSIFICATION UNCLASSIFIED	
22a. NAME OF RESPONSIBLE INDIVIDUAL Dr. Henry R. Radoski, Directorate of Physical & Geophysical Sciences		22b. TELEPHONE NUMBER (Include Area Code) 202/767-4906	22c. OFFICE SYMBOL NP

DTIC FILE COPY

DTIC
DEC 07 1984

84 11 27 028

AFOSR-TR- 84 - 1023

SEMI-ANNUAL TECHNICAL REPORT

1 January 1984 - 30 June 1984

ARPA Order - 4397

Program Code - 3D60

Name of Contractor - Earth Resources Laboratory
Department of Earth, Atmospheric, and Planetary Sciences
Massachusetts Institute of Technology
Cambridge, Massachusetts 02139

Start Date of Contract - 1 December 1982

Contract Expiration Date - 30 November 1985

Amount of Contract Dollars - \$455,011

Contract Number - F49620-83-C-0038

Principal Investigators - Keiti Aki, 617/253-6397
Vernon F. Cormier, 617/253-7862
M. Nafi Toksöz, 617/253-7852

Program Manager - William J. Best

Short Title of Work - Effects of Heterogeneities on the Propagation, Scattering
and Attenuation of Seismic Waves and the Characterization
of Seismic Source

Sponsored by
Advanced Research Projects Agency (DOD)
ARPA Order No. 4397
Monitored by the Air Force Office of Scientific Research
Under Contract No. F49620-83-C-0038

The views and conclusions contained in this document are those of the authors
and should not be interpreted as necessarily representing the official policies,
either expressed or implied, of the Defense Advanced Research Projects Agency
or the U.S. Government.



Accession For	
NTIS GRA&I	<input checked="" type="checkbox"/>
DTIC TAB	<input type="checkbox"/>
Unannounced	<input type="checkbox"/>
Justification	
By _____	
Distribution/	
Availability Codes	
Dist	Special
A-1	

Approved for public release;
distribution unlimited.

84 11 27 028

SUMMARY

An important impact on the monitoring of a CTBT has recently been made by a renewed discussion of the decoupling problem. Specifically, since the decoupling of an underground explosion of low yield by detonation in a cavity is less efficient at high frequencies, the evasion of a CTBT through decoupling becomes increasingly difficult for a test site monitored by seismic stations recording frequencies greater than 10 Hz over high Q paths. Of particular importance then to CTBT monitoring will be the understanding of the relative importance of scattering versus intrinsic anelasticity to the attenuation in the crust and lithosphere, and the factors that are important to their regional variation. These problems are treated in this semi-annual report by comparing the predictions of multiple scattering theory with observations of S codas recorded from earthquakes in the Hindu Kush region by a local digital array. The complete study is contained in the Ph.D. thesis of Ru-Shan Wu, performed under the supervision of Profs. Aki and Toksöz. The work included in this report has been edited from that thesis.

The study has examined the attenuation of local/regional S codas from 0.25 Hz to 40 Hz in the Hindu Kush region. A goal of the study was to separate the relative contribution of scattering versus intrinsic anelasticity to the attenuation of coda waves. Coda attenuation has been analyzed in the frequency domain using a radiative transfer equation technique, which includes multiple scattering, and in the time domain using weak and strong scattering approximations. The frequency band less than 1 Hz appears to be dominated by strong, multiple scattering and wave interference that cannot be treated using the radiative transfer equation technique in the frequency domain.

AIR FORCE OFFICE OF SCIENTIFIC RESEARCH (AFSC)
 NOTICE OF TECHNICAL INFORMATION
 This report is available to the public
 upon request.
 Distribution is limited.
 MATTHEW J. KENNEDY
 Chief, Technical Information Division

This band may be dominated by scattering of surface and guided mode energy and multiple conversions of body wave energy to surface wave energy and vice versa by boundary topography and elastic heterogeneity. In the band 1.5 to 20 Hz intrinsic attenuation dominates scattering attenuation. The Hindu Kush data indicate that this intrinsic attenuation is frequency dependent in the 1.5 to 20 Hz band. The physical mechanism of this intrinsic attenuation is unknown. In the band above 20 Hz, regional phase onsets cannot be easily distinguished and scattering attenuation is best described by diffusion theory. Although coda Q's appear to be similar in tectonic regions, the type of analysis described in this report should be applied to many different regions before general conclusions can be made about the relative importance of scattering and intrinsic attenuation in different frequency bands.

MULTIPLE SCATTERING AND ENERGY TRANSFER OF SEISMIC WAVES
AND THE APPLICATION OF THE THEORY TO HINDU KUSH REGION

Summary	2.
Abstract	5.
1. Introduction	7.
2. Definitions and Notations	12.
3. Energy Density Distribution in the Case of Isotropic Scattering	18.
4. Strong Forward Scattering: The Case of Large Scale Inhomogeneities	28.
5. Seismic Wave Scattering and Attenuation in Hindu Kush Region	34.
6. Diffusion Approximation in Time Domain, the Constraint of Seismogram Envelope on the Scattering Strength	42.
7. Suggestions for Further Studies	50.
References	51.
Tables	57.
Figure Captions	65.
Figures	70.

Abstract

In order to separate the scattering effect from the intrinsic attenuation, we need a multiple scattering model for the seismic wave propagation in random heterogeneous media. In this paper, we apply the radiative transfer theory to seismic wave propagation and formulate in frequency domain the energy density distribution in space for a point source. We consider the cases of isotropic scattering and strong forward scattering. Some numerical examples are shown. It is seen that the energy density - distance curves have quite different shapes depending on the values of medium seismic albedo $B_0 = \eta_s / (\eta_s + \eta_a)$, where η_s is scattering coefficient and η_a is the absorption coefficient of the medium. For high albedo ($B > 0.5$) medium, the energy-distance curve is of arch shape and the position of the peak is a function of extinction coefficient of the medium $\eta_e = \eta_s + \eta_a$. Therefore we can separate the scattering and the absorption based on the measured energy density distribution curves.

We also discuss the approximate solutions in time domain: the single scattering approximation and the diffusion approximation. We apply the formulas of diffusion approximation for an arbitrary non-isotropic scattering function to the coda envelope and discuss its relation with the frequency domain solution.

The data from the digital recordings in Hindu Kush region are used as an example of application of the theory. From the derived energy density distribution curves and the discussion on the envelope shapes of the digitally filtered seismograms, we conclude that, in the frequency range 1.5 Hz to 20 Hz, scattering is not the dominant factor in the measured apparent attenuations, i.e. $B_0 < 0.5$ in the Hindu Kush region for this frequency range. Due to the insensitivity of the shape of the energy-distance curve for the case $B_0 < 0.5$ and the fluctuations of the data, we are not able to obtain the

precise B_0 values. Some interesting phenomena at low frequencies (<1.5 Hz) and high frequencies (>20 Hz) need to be studied further. The results obtained in this paper imply a frequency dependent Q .

Multiple Scattering and Energy Transfer of Seismic Waves
and Application of the Theory to Hindu Kush Region

1. INTRODUCTION

Are the measured apparent attenuations for short period seismic waves caused by anelasticity of the media or by scattering of the heterogeneities in the media? Is the single backscattering model a good approximation to the coda envelope decay or do we need a multiple scattering model which will have significant differences in describing the coda behavior from the single backscattering theory? These are long-standing problems. In order to answer these questions, we need to develop certain multiple scattering model for seismic waves and compare the predictions from it with those obtained from the single scattering theory. O'Doherty and Anstey (1971) derived a one-dimensional multiple scattering formulae for a stack of thin layers as

$$|T(\omega)| = e^{-R(\omega)t}, \quad (1.1)$$

where ω is the angular frequency of the wave, $t = N\tau$ is the travel time of passing through the stack, τ is the travel time for each layer and N is the number of the layers; $T(\omega)$ is the transmission response and $R(\omega)$ is the power spectrum of the reflection coefficient series normalized by the travel time. The exponential form of (1.1) itself exhibits the indiscriminability of the multiple scattering effect from the intrinsic absorption, if we observe only the decay of the transmitted waves. Richards and Menke (1983) did some numerical experiments on this model and discussed some possibilities of using the relation between amplitude spectra and phase spectra, the frequency contents of the coda and that of the main arrival etc. to distinguish the multiple scattering effects of thin layers from the intrinsic attenuation. We note that the formulation of the problem by O'Doherty and Anstey is essentially that of the random slab problem (see Kay and Silverman 1958, Hoffman 1964). The results are presented as the relations of transmitted or

reflected waves with the slab thickness, which do not necessarily represent the amplitude attenuation with distance or the envelope decay with time of seismic waves.

Kopnichev (1977) formulated the double and triple scattering for 2-D and 3-D media in the case of isotropic scattering. Gao et al. (1983, 1984) derived up to seventh order scattering and then obtained the approximate formulas of multiple scattering in time domain for 2-D and 3-D media using curve-fitting technique. However, the formulas derived are for the case in which the source and sensor are located in the same point. On the other hand, the most prominent evidences of multiple scattering would be manifested if the sensor could be situated at some place between the source and the point apart from the source by one mean-free-path of scattering (this will be shown later). Therefore it may be difficult to use these formulas for discriminating the scattering attenuation from the intrinsic attenuation, though the formulation may be very useful in other calculations.

In this paper, we derive the formulation of seismic energy transfer under multiple scattering by using the radiative transfer equation technique developed in the astrophysical optics and the neutron transport theory and explore the possibilities of using this approach to separate the scattering and intrinsic attenuation.

Historically, multiple scattering theory has been developed along two independent approaches: the analytic theory and the transport theory (for review see Ishimaru 1977). Both are based on the statistical treatment of wave propagation in random media. Because the complex heterogeneities are modeled with a random medium, the wavefields propagating therein are also random wavefields. We are interested only in some statistical quantities of the wavefield, such as the mean intensity, phase and amplitude fluctuations,

various correlation functions, pulse spreading, angular broadening, etc. All of these quantities can be obtained from the moments of the random field. The analytic theory starts with basic differential equations such as wave equations and, by introducing the scattering and absorption characteristics of the random heterogeneities, derives the differential or integro-differential equations for the moments of the wavefields. There are basically two branches in the analytic theory: the renormalization method and the small-angle approximation method. In the first branch the renormalization procedure was used for the formal perturbation series and the exact equation for the first moment (the mean field), known as the Dyson equation, and for the second moment (the correlation function), the Bethe-Salpeter equations were derived. These equations are exact in the sense that the multiple scattering of all orders, as well as the diffraction and interference effect are all included in the equations. However, since the operator involved in these equations are in the form of infinite series, there is no solution available at present. Approximations have to be made to the operator before some practical solutions can be obtained. The most widely used approximation is the first order smoothing approximation as called by Frisch (1968) (see also Ishimaru 1978, v. 2), in which the local Born approximation of the fluctuating field (or equivalently the Bilocal approximation to the mean field) is applied to the Dyson equation and the ladder approximation is applied to the Bethe-Salpeter equation. These approximations can be obtained by either the Feynman diagram method or the Bogoliubov smoothing method in the operator form (Frisch 1968, Tatarskii 1971, Ishimaru 1978; for the various names of the first order smoothing approximation, see also Wu 1982b, footnote 2). The justification for the use of this approximation has been clarified by Frisch (1968) by introducing the generalized Reynolds number. The basic physical condition for

the valid use of the approximation is the scattered field within a correlation length being weak compared with the incident field. In the case of large scale inhomogeneities, Fante (1982) has shown that a sufficient condition for applying the ladder approximation is the mean free path for multiple scattering being large in comparison with the correlation length of the medium. This condition is usually satisfied in the context of seismic wave scattering in the lithosphere. The first order smoothing approximation to the Dyson equation and Bethe-Salpeter equation can be shown (Frisch 1968) to be equivalent to the Foldy-Twersky system of equations, which have been developed independently for discrete random media, i.e. the media with randomly distributed scatterers. There are still no general solutions for these equations and further approximations are needed to put them into practical use. For small size inhomogeneities, there are some general solutions for the mean field, but no useful results for the second moments (Tatarski 1971, §61, Ishimaru 1978, ch. 14). It has been shown that the first order smoothing approximation of the Dyson and Bethe-Salpeter equations can lead to a radiative transfer equation for the specific intensity which is the 3D spatial Fourier transform of the spatial correlation function of the wavefield when the correlation function is a slowly varying function in space (Barabanenkov 1969, 1971, Tatarskii 1971, §63, Ishimaru 1975, 1978). Similarly, a generalized radiative transfer equation can be derived for the frequency correlation function (Ishimaru 1978). Thereby the link bridge has been established between the analytic theory and the transport theory.

The second branch of the analytic theory includes all the small-angle-scattering methods. Because of the small scattering angle approximation or forward-scattering approximation, the basic starting point of the method is the parabolic wave equation. There are two approaches: parabolic equation

approach and Feynman path integral approach. Tatarskii applies the Markov approximation to the parabolic wave equation, so the theory of Markov process can be used to the study of the problem (Tatarskii 1971). Uscinski, on the other hand, uses the plane wave decomposition and phase-screen technique to the parabolic wave equation (Uscinski 1977). At present, the parabolic equation methods can have only approximate solutions for up to the fourth moment equations. The path-integral approach starts with the Feynman path-integral representation of the parabolic wave equation and makes use of the small scattering-angle approximation and Markov approximation (Dashen 1977, Flatte et al., 1979). It can obtain solutions for any higher order moments for the Gaussian statistics. Flatte et al. have applied this approach to the ocean acoustics and obtained the expressions for phase and intensity fluctuations, various correlations and pulse wandering and spreading etc.

The transport theory (or radiative transfer theory) is a phenomenological approach. It does not start with the wave equation, but deals directly with the energy transport process. Therefore, only energy or intensity arithmetic appears in the theory and no wave interference is considered. This treatment much simplifies the mathematics. Historically it appeared earlier than the analytic theory, and has its root from Boltzmann's equations in the kinetic theory of gases and in the neutron transport theory. It was introduced into astrophysical optics by Schuster (1905), Chandrasekhar (1950) and others and is now widely used in the multiple scattering treatment in the astrophysical optics, ocean acoustics, neutron transport theory, electromagnetic wave remote sensing, marine biology, etc. (Chandrasekhar 1950, Sobolev 1963, Menzel 1966, Davison 1958, Bell and Glasstone 1970, Flatte 1979, Kong et al. 1984, Jerlov 1976). This approach also has its shortcomings. It can only deal with the second moments, it does not account for the diffraction and interference

phenomena. However, there are some new developments recently, which incorporate some wave interference effects into the radiative transfer equation. For example, in deriving the transfer equations from the Bethe-Salpeter equation, beside the ladder terms (which alone will lead to the regular intensity transfer equation), the cyclical diagrams are also included, resulting in a modified radiative transfer equation, which can account for the backscattering enhancement due to the constructive interference effect caused by the double passage of the backscattered waves (Zuniga et al. 1980). So-called "wave radiative transfer theory" based on the second order approximations to the Bethe-Salpeter equation is also under development (Tsang and Ishimaru 1983).

For the coda envelopes or coda energy problems of local earthquakes, it is apparently a wide-angle scattering problem, so that the transport theory is probably the most effective method to treat it at present. In this paper we use the frequency domain formulation mainly from the neutron transport theory and the electromagnetic wave propagation (Davison 1958, Liu and Ishimaru 1974, Fante 1973, Ishimaru 1978) to the energy density decay with distance of the seismic waves from local earthquakes, and discuss the possibility of using the decay curves to evaluate the relative strengths of the intrinsic absorption and the scattering coefficient of the medium in the region studied. Some examples are given for the Hindu-Kush region. The results and their geophysical meaning are also discussed.

2. DEFINITIONS AND NOTATIONS

It is difficult to keep all the notations and terminology in radiative transfer theory without causing ambiguities and contradictions with the traditional notation and terminology in seismology, when the theory is introduced into seismology. I will basically follow Ishimaru (1978) and make some necessary changes to keep the notations self-consistent.

$I(\underline{r}, \hat{\Omega})$: Specific intensity or directional intensity. It is the most fundamental quantity in transport theory. It gives the power flowing within a unit solid angle in the direction $\hat{\Omega}$, here $\hat{\Omega}$ is the unit vector, emanated from a unit area perpendicular to $\hat{\Omega}$, in a unit frequency band. The specific intensity is defined for a frequency ω , which is omitted in the notation.

In this paper we consider the S wave and its coda for small local earthquakes. Since the P wave energy is much smaller than the S wave energy for a double-couple point source which is the source model for small earthquakes, we consider here $I(\underline{r}, \hat{\Omega})$ as only the S wave energy by neglecting the mode converted energy from P waves. We assume here also that the wave energy described by $I(\underline{r}, \hat{\Omega})$ is depolarized, i.e. the energy is equally partitioned between the two orthogonal components of S waves. This agrees generally with the observations. Because of the free surface reflection and the scattering by heterogeneities, the S waves from a double-couple source get quickly depolarized. From the results of this paper, the energy density decay curves for the two orthogonal components are very similar to each other, which further validate the assumptions.

In order to measure the specific intensity (or directional intensity), we need strongly directional sensors, which are not available in the seismological practice. Therefore the specific intensity is not the quantity measured in practice, but is the important concept and quantity for theoretical derivations.

$\bar{I}(\underline{r})$: Average intensity, defined by

$$\bar{I}(\underline{r}) = \frac{1}{4\pi} \int_{4\pi} I(\underline{r}, \hat{\Omega}) d\Omega, \quad (2.1)$$

is the intensity at point \underline{r} averaged over all directions.

$\underline{E}(\underline{r})$: Energy density, defined by

$$\underline{E}(\underline{r}) = \frac{1}{C} \int_{4\pi} I(\underline{r}, \hat{\Omega}) d\Omega = \frac{4\pi}{C} \bar{I}(\underline{r}) . \quad (2.2)$$

where C is the wave velocity.

$\underline{J}(\underline{r})$: Flux density vector, defined by

$$\underline{J}(\underline{r}) = \int_{4\pi} I(\underline{r}, \hat{\Omega}) \hat{\Omega} d\Omega . \quad (2.3)$$

The net flux density in a particular direction $\hat{\Omega}_0$ is defined as $\hat{\Omega}_0 \cdot \underline{J}(\underline{r})$. It is the net power transferred along the $\hat{\Omega}_0$ direction across a unit area perpendicular to $\hat{\Omega}_0$. In this paper, we also use the notation for the energy flux density, i.e. the power flux density divided by the wave velocity c .

$S(\hat{\Omega}, \hat{\Omega}_0)$: Scattering intensity function of a random medium, which is related to the single scattering amplitude $f(\hat{\Omega}, \hat{\Omega}_0)$ of an elementary volume dV of the inhomogeneous medium by

$$S(\hat{\Omega}, \hat{\Omega}_0) = \frac{\langle |f(\hat{\Omega}, \hat{\Omega}_0)|^2 \rangle}{dV}, \quad (2.4)$$

where $\langle \rangle$ denotes taking ensemble average. $S(\hat{\Omega}, \hat{\Omega}_0)$ gives the scattered power in $\hat{\Omega}$ direction within a unit solid angle by a unit volume of the random medium for a unit flux density of incident wave in $\hat{\Omega}_0$ direction.

In this paper we will give a unified treatment for both the discrete and the continuous random media. For a discrete random medium composed of randomly distributed scatterers, $S(\hat{\Omega}, \hat{\Omega}_0)$ is defined by the scattering characteristics of individual scatterers; while in the case of random continua, we can choose the volume elements small enough so that we can derive the single scattering amplitude $f(\hat{\Omega}, \hat{\Omega}_0)$ by the Born approximation.

$\hat{g}(\hat{\Omega}, \hat{\Omega}_0)$: Directional scattering coefficient, defined by

$$\hat{g}(\hat{\Omega}, \hat{\Omega}_0) = 4\pi S(\hat{\Omega}, \hat{\Omega}_0) . \quad (2.5)$$

for the definition and the derivation for elastic random media, see paper II (Wu and Aki, 1984b).

$\eta_s \equiv g$: Scattering coefficient of the medium defined by

$$\eta_s = \int_{4\pi} S(\hat{\Omega}, \hat{\Omega}_0) d\hat{\Omega} = \frac{1}{4\pi} \int_{4\pi} \hat{g}(\hat{\Omega}, \hat{\Omega}_0) d\hat{\Omega} , \quad (2.6)$$

which gives the total power loss due to scattering by a unit volume random medium per unit flux density of incident wave under the single scattering assumption.

$\eta_a \equiv b$: Absorption coefficient of the medium, which gives the power loss due to absorption by a unit volume random medium per unit flux density of incident wave.

η_e : Extinction coefficient of the medium, defined by

$$\eta_e = \eta_a + \eta_s \quad (2.7)$$

$l_0 \equiv a$: Correlation length of the random medium.

$L_e = 1/\eta_e$: Extinction length of the medium.

$L_a = 1/\eta_a$: Absorption length of the medium. (2.8)

$L_s = 1/\eta_s$: Scattering length or scattering mean free path of the medium.

D_e : Numerical extinction distance, which is called "optical distance" in optics.

D_a : Numerical absorption distance,

D_s : Numerical scattering distance, defined by

$$D_e = r/L_e,$$

$$D_a = r/L_a,$$

$$D_s = r/L_s,$$

where r is the travel distance. (2.9)

B_0 : Medium seismic albedo, defined by

$$B_0 = \frac{\eta_s}{\eta_e} = \frac{\eta_s}{\eta_s + \eta_a} . \quad (2.10)$$

$D(\hat{\Omega}, \hat{\Omega}_0)$: Scattering directivity, defined by

$$D(\hat{\Omega}, \hat{\Omega}_0) = \frac{g(\hat{\Omega}, \hat{\Omega}_0)}{\eta_s} = \frac{4\pi S(\hat{\Omega}, \hat{\Omega}_0)}{\eta_s} \quad (2.11)$$

It is the normalized directional scattering coefficient, and satisfies

$$\frac{1}{4\pi} \int_{4\pi} D(\hat{\Omega}, \hat{\Omega}_0) = 1, \quad (2.12)$$

that means its average over all the directions is equal to unit. In the case of isotropic scattering

$$D(\hat{\Omega}, \hat{\Omega}_0) \equiv 1 . \quad (2.13)$$

Its relation with the "phase function" in the radiative transfer theory (Chandrasekhar 1950, Ishinara 1978) is

$$D(\hat{\Omega}, \hat{\Omega}_0) = B_{op}(\hat{\Omega}, \hat{\Omega}_0) . \quad (2.14)$$

$p(\hat{\Omega}, \hat{\Omega}_0)$: Phase function (see 2.14).

In the case of a discrete random medium having statistically uniformly distributed random scatterers with number density n , we have

$\sigma_d(\hat{\Omega}, \hat{\Omega}_0)$: Differential (or directional) scattering cross-section of the scatterers.

$$S(\hat{\Omega}, \hat{\Omega}_0) = n\sigma_d(\hat{\Omega}, \hat{\Omega}_0). \quad (2.15)$$

σ_s : Scattering cross-section of the scatterers, defined by

$$\sigma_s = \int_{4\pi} \sigma_d(\hat{\Omega}, \hat{\Omega}_0) d\hat{\Omega} \quad (2.16)$$

σ_a : Absorption cross-section of the scatterers.

$\sigma_t = \sigma_s + \sigma_a$: Total cross-section of the scatterers.

η_h : Absorption coefficient of the host medium.

$$\eta_s = n\sigma_s, \quad (2.16)$$

$$\eta_a = n\sigma_a + \eta_h, \quad (2.17)$$

$$D(\hat{\Omega}, \hat{\Omega}_0) = \frac{4\pi\sigma_d(\Omega, \Omega_0)}{\sigma_s} \quad (2.18)$$

B_1 : Scatterer albedo, defined by

$$B_1 = \frac{\sigma_s}{\sigma_s + \sigma_a} = \frac{\sigma_s}{\sigma_t}. \quad (2.19)$$

Therefore,

$$B_0 = \frac{\eta_s}{\eta_s + \eta_a} = \frac{n\sigma_s}{n\sigma_s + n\sigma_a + \eta_h} = \frac{n\sigma_s}{n\sigma_t + \eta_h}. \quad (2.20)$$

When $\eta_h \ll n\sigma_t$, we have

$$B_0 \approx \frac{\sigma_s}{\sigma_t} \left(1 - \frac{\eta_h}{n\sigma_t}\right) = B_1 \left(1 - \frac{\eta_h}{n\sigma_t}\right). \quad (2.21)$$

For a perfect scattering medium $B_0 = 1$.

3. ENERGY DENSITY DISTRIBUTION IN THE CASE OF ISOTROPIC SCATTERING

Knowing the extinction coefficient and scattering coefficient of the medium η_e , η_s and the scattering directivity $D(\hat{\Omega}, \hat{\Omega}_0)$ or the scattering intensity function of the medium $S(\hat{\Omega}, \hat{\Omega}_0)$ defined by (2.6), (2.7), (2.11) and (2.4), we can obtain the differential equation for the specific intensity $I(\underline{r}, \hat{\Omega})$, the "equation of transfer" (Chandrasekhar 1950, I, Ishimara 1978, ch. 7):

$$\begin{aligned} \frac{dI(\underline{r}, \hat{\Omega})}{dl} &= -\eta_e I(\underline{r}, \hat{\Omega}) + \int_{4\pi} S(\hat{\Omega}, \hat{\Omega}_0) I(\underline{r}, \hat{\Omega}_0) d\Omega_0 + W(\underline{r}, \hat{\Omega}) \\ &= -\eta_e I(\underline{r}, \hat{\Omega}) + \frac{\eta_s}{4\pi} \int_{4\pi} D(\hat{\Omega}, \hat{\Omega}_0) I(\underline{r}, \hat{\Omega}_0) d\Omega_0 + W(\underline{r}, \hat{\Omega}), \end{aligned} \quad (3.1)$$

where $W(\underline{r}, \hat{\Omega})$ is the source intensity function, which defines the amount of power emitted from the sources into the direction $\hat{\Omega}$ per unit solid angle. In (3.1), dl is the length of a cylindrical elementary volume of unit cross section in the medium with the axis of the cylinder in $\hat{\Omega}$ direction (Fig. 3.1). Therefore the left hand side of (3.1) represents the total change of the specific intensity for a unit travel distance. The first term in right hand side of (3.1) is the loss of power in $\hat{\Omega}$ direction due to absorption and scattering, whereas the second term gives the gain of power in that direction from the scattered waves for the incident intensity from all directions and the third term is the energy supply from the sources. No general analytic solutions are available for (3.1). Some methods such as the Gauss-quadrature can be used to obtain the numerical solutions for a general scattering function. Let us first consider the simplest case of isotropic scattering. In this case the scattering directivity $D(\hat{\Omega}, \hat{\Omega}_0) \equiv 1$. Integrating (3.1) over all directions $\hat{\Omega}$, we obtain equation for the average intensity $\bar{I}(\underline{r})$ or the

energy density $E(\underline{r})$ (2.2)

$$\begin{aligned} \frac{dE(\underline{r})}{d\underline{l}} &= -\eta_e E(\underline{r}) + \frac{1}{C} \int_{4\pi} \left[\frac{\eta_s}{4\pi} \int_{4\pi} I(\underline{r}, \hat{\Omega}_0) d\Omega_0 + W(\underline{r}, \hat{\Omega}) \right] d\Omega \\ &= -\eta_e E(\underline{r}) + Q(\underline{l}), \end{aligned} \quad (3.2)$$

where C is the wave velocity. (3.2) is in a form of first order differential equation, in which the second term in RHS is the source term

$$Q(\underline{l}) = \frac{1}{C} \int_{4\pi} \left[\frac{\eta_s}{4\pi} \int_{4\pi} I(\underline{r}, \hat{\Omega}_0) d\Omega_0 + w(\underline{r}, \hat{\Omega}) \right] d\Omega. \quad (3.3)$$

The general solution for (3.2) is

$$E(\underline{r}) = A e^{-\eta_e \underline{l}} + \int_0^{\underline{l}} Q(\underline{l}_1) e^{-\eta_e (\underline{l} - \underline{l}_1)} d\underline{l}_1, \quad (3.4)$$

where A is a constant.

The energy density (3.4) is composed of two terms. The first term is a simple exponential decay with the extinction coefficient η_e as its attenuation coefficient; this is the coherent energy density E_c or "reduced energy density" (Ishimaru 1978). The second term is therefore the diffuse energy density E_d which is produced by scattering. Applying the initial condition

$$E(\underline{r}_0) = E_{in}, \quad (3.5)$$

where E_{in} is the incident energy, we get

$$\begin{aligned} E(\underline{r}) &= E_c(\underline{r}) + E_d(\underline{r}) \\ E_c(\underline{r}) &= E_{in} e^{-\eta_e \underline{l}} \\ E_d(\underline{r}) &= \int_0^{\underline{l}} Q(\underline{l}_1) e^{-\eta_e (\underline{l} - \underline{l}_1)} d\underline{l}_1 \\ &= \frac{1}{C} \int_0^{\underline{l}} \int_{4\pi} \left[\frac{\eta_s}{4\pi} \int_{4\pi} I(\underline{r}, \hat{\Omega}_0) d\Omega_0 + W(\underline{r}, \hat{\Omega}) \right] e^{-\eta_e (\underline{l} - \underline{l}_1)} d\Omega d\underline{l}_1. \end{aligned} \quad (3.8)$$

In order to calculate the diffuse term (3.8), we need to know the intensity $I(\underline{r}, \hat{\Omega}_0)$ which is related to the total energy density. Therefore (3.8) is in the form of integral equation. To carry out the integration with respect to $\hat{\Omega}$, we note that, the intensity gain in the direction $\hat{\Omega}$ within $d\hat{\Omega}$ are contributed from the intensity of all the volume elements dV_1 at \underline{r}_1 within the elementary solid angle, and

$$dV_1 = d\hat{\Omega} |\underline{r} - \underline{r}_1|^2 d\ell_1 . \quad (3.9)$$

Therefore (3.8) becomes

$$E_d(\underline{r}) = \int_V \left[\eta_s E(\underline{r}_1) + \frac{4\pi}{c} W(\underline{r}_1, \hat{\Omega}) \right] \frac{e^{-\eta_e |\underline{r} - \underline{r}_1|}}{4\pi |\underline{r} - \underline{r}_1|^2} dV_1 . \quad (3.10)$$

The integration is over the volume of the random medium. The integral equation for the total energy density becomes (see also Ishimaru, 1978, ch. 12).

$$E(\underline{r}) = E_{in} e^{-\eta_e l} + \int_V \left[\eta_s E(\underline{r}_1) + \epsilon(\underline{r}_1, \hat{\Omega}) \right] G_o(\underline{r} - \underline{r}_1) dV_1 , \quad (3.11)$$

where

$$\epsilon(\underline{r}, \hat{\Omega}) = \frac{4\pi}{c} W(\underline{r}, \hat{\Omega}) \quad (3.12)$$

is the source energy density function, and

$$G_o(\underline{r} - \underline{r}_1) = \frac{e^{-\eta_e R}}{4\pi R^2} = \frac{e^{-\eta_e |\underline{r} - \underline{r}_1|}}{4\pi |\underline{r} - \underline{r}_1|^2} . \quad (3.13)$$

Integral equation (3.11) can also be derived from the first order smoothing approximation of the Dyson and Bethe-Salpeter equations (Lin and Ishimaru 1974).

From (3.11), the energy density $E(\underline{r})$ is totally defined by the incident field, the source-function, and the volume of the random medium. For the problems of seismic coda waves of local earthquakes, the distances between the stations and the sources are short compared to the travel time of coda waves.

As the first approximation, we consider the problem of a point source located in an infinite randomly inhomogeneous medium. The effect of the free surface is like a mirror reflecting the half random space to a whole random space with the upper half space being the mirror image of the lower half space. The limited thickness of the lithosphere, which is supposed to be more heterogeneous than the asthenosphere beneath will have influence on the coda of later part. Further discussion about the limitation of the model will be given later in this paper.

In (3.11), suppose the incident field $E_{in} = 0$ and the point source is located at $\underline{r} = 0$, radiating the total power P_0 . Then

$$\underline{\varepsilon}(\underline{r}) = \frac{P_0}{C} \delta(\underline{r}) = E_0 \delta(\underline{r}) \quad (3.14)$$

The equation (3.11) becomes

$$\begin{aligned} \underline{E}(\underline{r}) &= E_0 \frac{e^{-\eta_e r}}{4\pi r^2} + \int_V \eta_s \underline{E}(\underline{r}_1) \frac{e^{-\eta_e |\underline{r}-\underline{r}_1|}}{4\pi |\underline{r}-\underline{r}_1|^2} dV_1 \\ &= E_0 G_0(\underline{r}) + \int_V \eta_s \underline{E}(\underline{r}_1) G_0(\underline{r}-\underline{r}_1) dV_1. \end{aligned} \quad (3.15)$$

This is a Faltung type or convolution type integral equation (Tricomi 1957, Carrier et al. 1966), Fourier transform method can be used for solution. Assuming $E_0 = 1$, the solution can be written as (see Davison 1958, Lin and Ishimaru 1974, Ishimaru 1978 (12-21))

$$\begin{aligned} E(\underline{r}) &= \frac{\eta_e P_d}{4\pi r} \exp(-\eta_e d_0 r) + \frac{\eta_e}{4\pi r} \int_1^\infty f(s, B_0) \exp(-\eta_e r s) ds \\ &= E_d(\underline{r}) + E_c(\underline{r}), \end{aligned} \quad (3.16)$$

where

$$Pd = \frac{2 d_o^2 (1-d_o^2)}{B_o (d_o^2 + B_o - 1)}, \quad (3.17)$$

and d_o is the diffuse multiplier determined by

$$\frac{B_o}{2d_o} \ln \left(\frac{1+d_o}{1-d_o} \right) = 1; \quad (3.18)$$

and

$$f(s, B_o) = \left\{ \left[1 - \frac{B_o}{s} \tanh^{-1} \left(\frac{1}{s} \right) \right]^2 + \left(\frac{\pi}{2} \frac{B_o}{s} \right)^2 \right\}^{-1}. \quad (3.19)$$

The first term in (3.16) is the diffuse term E_d , which is attributed to the pole residue in the complex spatial frequency plane, and the second term, coherent term E_c is from the branch cut integration.

Fig. 3.2 shows the relation between the diffuse multiplier d_o and the medium albedo B_o . d_o is always less than 1. When distance r is large, especially for large B_o , the diffuse term becomes dominant (see also Fig. 9), and $E(r)$ will be approximately an exponential decay with an apparent attenuation coefficient $d_o \eta_e$, which is less than the extinction coefficient η_e . The degree of reduction depends on the albedo B_o . The diffuse term can also be written as

$$E_d(r) = \frac{\eta_e P_d}{4\pi r} \exp[-(\eta_a + d_s \eta_s) r],$$

$$d_s = \frac{d_o - (1 - B_o)}{B_o}. \quad (3.20)$$

d_s is a multiplier and $d_s \eta_s$ gives the effective contributions of the scattering coefficient to the apparent attenuations. d_s is also plotted in Fig. 2. Table 1 lists some values of d_o and d_s versus B_o .

The coherent term can also be written as

$$E_c(r) = \frac{\eta_e}{4\pi r} \int_0^1 f(\xi, B_0) \exp\left(-\frac{\eta_e r}{\xi}\right) \frac{d\xi}{\xi^2}, \quad (3.21)$$

by setting $\xi = 1/s$ for the convenience of computation. Fig. 3.3 shows the behavior of the two factors of the integrand for different numerical extinction distances $D_e = \eta_e r$ and different medium albedo B_0 . $\exp(-D_e/\xi)/\xi^2$ has a sharp peak for small D_e when ξ is small; whereas $f(\xi, B_0)$ is nearly singular for small B_0 when ξ is close to 1. Therefore, in doing numerical integration, we used Romberger integration method for three separate segments to take care of the abrupt changes of the integrand at both ends of the interval. The Gauss-Legendre quadrature is also used to check the results. It turned out that the Gauss-Legendre quadrature of order 10 gives fairly good results.

In the following we will show some numerical results of the energy density distribution along the travel path from the source point. In the case of homogeneous media, the decay of energy density with distance is only due to geometric spreading. For a isotropic point source, the decay is $1/4\pi r^2$. Therefore, we normalize the distribution for inhomogeneous media (3.16) by the homogeneous distribution, i.e. multiply both sides of (3.16) with $4\pi r^2$,

$$\begin{aligned} E_n(r) = 4\pi r^2 E(r) &= \eta_e P_d r \exp(-\eta_e d_0 r) + \eta_e r \int_0^1 f(\xi, B_0) \exp\left(-\frac{\eta_e r}{\xi}\right) \frac{d\xi}{\xi^2} \\ &= D_e P_d \exp(-d_0 D_e) + D_e \int_0^1 f(\xi, B_0) \exp\left(-D_e/\xi\right) \frac{d\xi}{\xi^2}, \end{aligned} \quad (3.22)$$

where $E_n(r)$ stands for the normalized energy density distribution. Fig. 3.4 gives the results for different medium albedo B_0 . The diffuse term and the coherent term are also plotted in the figure for comparison. The coherent term has little changes for different B_0 , whereas the diffuse term varies dramatically with B_0 , especially when $B_0 > 0.5$, i.e. when scattering is dominant. This gives the possibility of using the energy density decay curves to calculate the extinction coefficient η_e and the medium albedo B_0 , hence to separate the absorption coefficient η_a and the scattering coefficient η_s . In the case of $B_0 > 0.5$, the diffuse term is dominant. There will be a peak on the $E(r)$ curve, the position of the peak will depend on η_e and B_0 of the medium. When $B_0 < 0.5$, the coherent term is dominant for $D_e < 2$. Therefore the shape of the curve is not very sensitive to the change of B_0 , so that the separation of scattering from absorption becomes difficult.

By assuming a point source with $E_0 = 1$, we get $E(r)$ around the peak with values greater than 1, that need some explanation. As shown in Fig. 3.5, the normalized energy density $E_n(r) = 4\pi r^2 E(r)$ represents the energy received by the ring shell (hatched). In a homogeneous medium, if there is no absorption, the energy received will be equal to the source energy. In a scattering medium, the wave energy can go outward and inward across the shell. We denote the outward energy flux by F_r^+ and the inward energy flux by F_r^- . In the figure, we sketched one possible path of multiple scattering. No matter how complicated the path is and how long the time delay is compared to the direct path, the closed ring shell will eventually receive all the energy emitted by the source. There is no escape! Therefore, in this case the F_r^+ is equal to the total energy. However, the shell will also receive the inward scattered energy, so the total received energy $F_r^+ + F_r^-$ is greater than E_0 . Of course the net energy flux $F_r^+ - F_r^-$ is always less than E_0 . If there exists absorption,

the amount of received energy will depend on the energy balance between the absorption loss and the inward-scattering gain. Near the source, r is small, the ring shell has a small surface area for receiving the inward-scattered energy, so $E_n(r) \approx E_0$. When r increases, the surface area of the shell also increases, so that more inward-scattered energy can be received, resulting in the growth of $E_n(r)$. However, the absorption loss also grows with r due to the increase of the path length. Up to some distance r , the growth rate of gain is equal to the growth rate of loss, the curve reaches its maximum. Beyond this distance, the absorption loss prevails.

Fig. 3.6 replots the curves of Fig. 4 in a semi-logarithm coordinate system. Fig. 7 and 8 plot some $E_n(r)$ curves for cases of constant absorption and constant scattering respectively. In this paper $b \equiv \eta_R$ $g \equiv \eta_S$. Fig. 3.7 shows the influence of different scattering coefficients on the energy density distribution curve of a constant absorption medium. The distance is normalized by the absorption length of the medium $L_a = 1/\eta_a$. It is seen from the figure that, for large distances compared with the absorption length of the medium, the decay of the energy density is nearly exponential with an apparent attenuation coefficient different from both the extinctions coefficient and the absorption coefficient. In the figure, b is the true absorption coefficient, \hat{b} is the apparent attenuation coefficient measured from the slope of the curve. It can be seen that, for strong scattering ($B_0 > 0.5$), the apparent attenuation is much bigger than the absorption coefficient but much smaller than the extinction coefficient (for $B_0 = 0.9$, $\hat{b} = 4.5b = 0.45 \eta_e$). For weak scattering ($B_0 < 0.5$), the influence of scattering to the apparent attenuation is less appreciable. When $B_0 = 0.5$, $\hat{b} = 1.62b$. On the other hand, for small absorption distance ($D_a < 1$), the shape of $E(r)$ curve varies drastically depending on the values of B_0 , which provides the

basis for the separation of scattering effect and the absorption effect. Fig. 3.8 in a similar way shows the influence of absorption on the $E(r)$ curve of a constant scattering medium.

In order to compare the relative contributions of the diffuse term and the coherent term, we plot them on Fig. 3.9 and Fig. 3.10 with the distance normalized by the extinction length L_e and scattering length L_s respectively.

Now, we will derive the radial energy flux density $J_r(r)$. We know the energy conservation relation (see Ishimaru 1978, (7.28))

$$\operatorname{div} \underline{J}(\underline{r}) = -\frac{\eta_a}{C} \int_{4\pi} I(\underline{r}, \hat{\Omega}) d\Omega + \frac{1}{C} \int_{4\pi} W(\underline{r}, \hat{\Omega}) d\Omega, \quad (3.23)$$

where $\underline{J}(\underline{r})$ is the energy flux density vector, C is the wave velocity and $W(\underline{r}, \hat{\Omega})$ is the source intensity. For isotropic scattering in the source free region

$$\operatorname{div} \underline{J}(\underline{r}) = \eta_a E(r). \quad (3.24)$$

In view of the spherical symmetry, there is no transverse component of $\underline{J}(\underline{r})$, therefore (3.24) becomes

$$\operatorname{div} \underline{J}(\underline{r}) = \frac{1}{r^2} \frac{\partial}{\partial r} (r^2 J_r) = -\eta_a E(r). \quad (3.25)$$

Then

$$J_r = -\frac{\eta_a}{r^2} \int_0^r E(r) r^2 dr = \frac{\eta_a}{r^2} \int_r^\infty E(r) r^2 dr \quad (3.26)$$

Normalizing J_r by the homogeneous case, we get

$$J_{nr}(r) = 4\pi r^2 J_r(r) = \eta_a \int_r^\infty 4\pi r^2 E(r) dr = \eta_a \int_r^\infty E_n(r) dr. \quad (3.27)$$

Substituting (3.22) into (3.27) yields

$$\begin{aligned}
 J_{nr}(r) &= 4\pi r^2 J_r(r) \\
 &= (1-B_0) \left\{ \frac{P_d}{d_0} \left(D_e + \frac{1}{d_0} \right) \exp(d_0 D_e) + \int_0^1 f(\xi, B_0) \left(1 - \frac{D_e}{\xi} \right) \exp(-D_e/\xi) d\xi \right\} \quad (3.28)
 \end{aligned}$$

Fig. 3.11 and 3.12 give some numerical results with the distance normalized by the extinction length and by the absorption length respectively, together with the results for the forward scattering approximation (see next section). It can be seen that the radial net flux is always smaller than the source energy E_0 . However, the radial energy flux is difficult to measure in the practice of seismology. The reason is the difficulty of separating the inward and outward energy flow. Nevertheless, the comparison between $E(r)$ and $J_r(r)$ helps us understand the multiple scattering process.

4. STRONG FORWARD SCATTERING: THE CASE OF LARGE SCALE INHOMOGENEITIES

From the analysis of coda generations for local earthquakes, we conclude that the lithosphere in tectonically active regions may be rich in small scale heterogeneities (less than 1 km) (paper II). On the other hand, by measuring the phase and amplitude fluctuations in large seismic arrays as LASA and NORSAR, large scale velocity inhomogeneities (10-20 km) underneath the arrays were revealed (Aki 1973, Capon 1974, Berteusson et al. 1975). Therefore, the lithosphere may have multi-scale inhomogeneities. For short period seismic waves (around 1 Hz), the scattering by the small scale heterogeneities may be in the Rayleigh and Mie scattering region. From the elastic scattering pattern (paper I, II), we may approximately use the isotropic scattering approximation. However, for the large scale velocity inhomogeneities, the forward scattering is dominant. The energy density distribution with distance will be quite different from the case of isotropic scattering. Since most of the scattered energy is concentrated in the forward direction within a small cone, the focussing and defocussing, diffraction interference phenomena become important. Most of the scattered energy arrives at the receiver point with much shorter travel paths, so that the energy delay due to scattering is much less severe than the case of isotropic scattering. From a reasoning similar to that in Fig. 3.5, we can see that, the normalized energy density decay curve will not have a peak of value greater than 1. Because the inward scattered energy is much less than the outward scattered energy, the energy density which is $J_r^+ + J_r^-$, where J_r^+ and J_r^- is the outward and inward radial energy flux respectively, will have no too much difference from the net energy flux $J_r = J_r^+ - J_r^-$. In the following, let us examine what can be obtained from the theory available in transport theory.

Fante (1973) has solved the transport equation under the forward scattering approximation, and Ishimaru (1978, ch. 13) has a lucid derivation and discussion on it. Here we only draw some main threads for understanding. Since

$$\frac{dI(\underline{r}, \hat{\underline{\Omega}})}{d\ell} = \hat{\underline{\Omega}} \cdot \text{grad } I(\underline{r}, \hat{\underline{\Omega}}), \quad (4.1)$$

where $d\ell$ is the length of an elementary segment in $\hat{\underline{\Omega}}$ direction (Fig. 3.1), the transport equation (3.1) can be written as

$$\hat{\underline{\Omega}} \cdot \text{grad } I(\underline{r}, \hat{\underline{\Omega}}) = -\eta_a I(\underline{r}, \hat{\underline{\Omega}}) + \eta_s \int_{4\pi} D(\hat{\underline{\Omega}}, \hat{\underline{\Omega}}_0) I(\underline{r}, \hat{\underline{\Omega}}_0) d\hat{\underline{\Omega}}_0 + w(\underline{r}, \hat{\underline{\Omega}}). \quad (4.2)$$

Because the scattered energy is mostly confined within a small angle in the forward direction, we choose the z-axis of the cartesian coordinates as this direction, and approximate (4.2) through the following steps.

$$\hat{\underline{\Omega}} = l\hat{x} + m\hat{y} + n\hat{z}, \quad (4.3)$$

where \hat{x} , \hat{y} and \hat{z} are the unit vectors in x, y and z-axis respectively, and l, m, n , the corresponding direction cosines. In the spherical coordinate system with z-axis as its polar axis (Fig. 4.1)

$$l = \sin\theta\cos\phi, \quad m = \sin\theta\sin\phi, \quad n = \cos\theta. \quad (4.4)$$

Because the angle with z-axis θ is always small, we have approximations

$$\begin{aligned} n &= \cos\theta \approx 1 \\ d\hat{\underline{\Omega}} &= nd\hat{\underline{\Omega}} = dl dm = d\underline{s}, \\ \int_{4\pi} d\hat{\underline{\Omega}} &\approx \int_{-\infty}^{\infty} dl \int_{-\infty}^{\infty} dm = \int d\underline{s}, \\ \hat{\underline{\Omega}} \cdot \text{grad } I(\underline{r}, \hat{\underline{\Omega}}) &\approx \frac{\partial}{\partial z} I(\underline{r}, \hat{\underline{\Omega}}) + \underline{s} \cdot \nabla_{\underline{t}} I(\underline{r}, \hat{\underline{\Omega}}), \end{aligned} \quad (4.5)$$

where

$$\begin{aligned}\underline{r} &= \hat{x}x + \hat{y}y + \hat{z}z = \underline{\rho} + \hat{z}z, \\ \underline{r} &= \hat{1}x + \hat{m}y, \quad \nabla t = \frac{\partial}{\partial x} \hat{x} + \frac{\partial}{\partial y} \hat{y}.\end{aligned}\quad (4.6)$$

Note that \underline{s} is not a unit vector. Because θ is a small angle, the magnitude of \underline{s} is much smaller than 1.

By these approximations (4.2) becomes

$$\begin{aligned}\frac{\partial}{\partial z} I(z, \underline{\rho}, \underline{s}) + \hat{s} \cdot \nabla_t I(z, \underline{\rho}, \underline{s}) \\ = -\eta_e I(z, \underline{\rho}, \underline{s}) + \frac{\eta_s}{4\pi} \iint_{-\infty}^{\infty} D(\underline{s} - \underline{s}') I(z, \underline{\rho}, \underline{s}') d\underline{s}' + W(z, \underline{\rho}, \underline{s}).\end{aligned}\quad (4.7)$$

here $D(\hat{\Omega}, \hat{\Omega}_0)$ is assumed only as a function of $\hat{\Omega} - \hat{\Omega}_0$. Since most of the energy is confined within a small angle with z-axis, the integration limits for l and m are extended to $\pm\infty$ without introducing any significant change.

Again (4.7) can be solved by the Fourier transform method (Fante 1973, Ishimaru 1978, ch. 13), the general solution for $W(z, \underline{\rho}, \underline{s}) = 0$ is

$$I(z, \underline{\rho}, \underline{s}) = \frac{1}{(2\pi)^4} \int d\underline{k} \int d\underline{q} \exp(-i\underline{k} \cdot \underline{\rho} - i\underline{s} \cdot \underline{q}) I_0(\underline{k}, \underline{q} + \underline{k}z) K(z, \underline{k}, \underline{q}), \quad (4.8)$$

where

$$I_0(\underline{k}, \underline{q}) = \iint I_0(\underline{\rho}, \underline{s}) \exp(i\underline{k} \cdot \underline{\rho} + i\underline{s} \cdot \underline{q}) d\underline{\rho} d\underline{s} \quad (4.9)$$

is the double Fourier transform of the incident intensity $I_0(\underline{\rho}, \underline{s})$ at $z=0$, and

$$K(z, \underline{k}, \underline{q}) = \exp\left\{ \int_0^z \eta_e \left[1 - \frac{B_0}{4\pi} D(\underline{q} + \underline{k}(z-z')) \right] dz' \right\} \quad (4.10)$$

where

$$D(\underline{q}) = \iint_{-\infty}^{\infty} D(\underline{s}) \exp(i\underline{s} \cdot \underline{q}) d\underline{s} . \quad (4.11)$$

There is no general explicit expression for (4.8) for a general scattering directivity $D(\underline{s})$. If we approximate the strong forward scattering pattern by a Gaussian function,

$$D(\underline{s}) \approx 4\xi \exp(-\xi s^2) \quad (4.12)$$

where ξ is a parameter proportional to $(l_0/\lambda)^2$, and l_0 is correlation length of the random medium, λ is the wavelength, substituting into (4.11) and (4.10) yields

$$D(\underline{q}) = 4\pi \exp\left(-\frac{q^2}{4\xi}\right) , \quad (4.13)$$

$$K(z, \underline{k}, \underline{q}) = \exp\left\{ \int_0^z \eta_e [1 - B_0 \exp\left(\frac{-q^2}{4\xi}\right)] dz' \right\} . \quad (4.14)$$

Since most of the energy is confined within a small cone along z -axis, we consider the case of a plane incident wave

$$I_0(\underline{\rho}, \underline{s}) = I_0 \delta(\underline{s}) , \quad (4.15)$$

$$I_0(\underline{k}, \underline{q}) = (2\pi)^2 I_0 \delta(\underline{k}) . \quad (4.16)$$

From (4.8) we have

$$I(z, \underline{\rho}, \underline{s}) = \frac{I_0}{(2\pi)^2} \int d\underline{k} \int d\underline{q} \exp(-i\underline{k} \cdot \underline{\rho} - i\underline{s} \cdot \underline{q}) \delta(\underline{k}) \exp[-\eta_e z + \eta_s z \exp\left(\frac{-q^2}{4\xi}\right)] . \quad (4.17)$$

When the scattering distance is large, i.e. $\eta_s z \gg 1$, the main contributions to the integral in (4.17) come from the integrands with small q 's. We can set

$$\exp\left(\frac{-q^2}{4\xi}\right) \approx 1 - \frac{q^2}{4\xi} . \quad (4.18)$$

Therefore

$$I(z, \underline{\rho}, \underline{s}) \approx \frac{I_0 \xi}{\pi \eta_s z} \exp\left[-\eta_s z - \frac{\xi s^2}{\eta_s z}\right] . \quad (4.19)$$

$$E(z, \rho) = J(z, \rho) = \int I(z, \rho, s) ds = I_0 e^{-\eta_a z} . \quad (4.20)$$

We see that, under forward scattering approximation, the energy density decay with distance is only due to the absorption. That is because, in the approximation, we neglect the backscattering and the path length differences between the direct path and the multiple scattering paths by letting $\cos\theta=1$. In Fig. 3.11 and Fig. 3.12 we plot the energy flux $J(r)$ of strong forward scattering vs. that of the isotropic scattering. If we consider the lengthening of travel paths by multiple forward scattering, the decay curve could be somewhere between these two extremes.

(4.19) gives the angle distribution of intensities. The incident wave has only intensity in z-direction, after scattering by the medium, the intensities with different directions have a Gaussian distribution and the width of the angle distribution broadens with distance. The loss due to the scattering of energy to other directions is compensated by the gain of scattered energy from other directions. Therefore there is no energy loss except absorption. However, in order to calculate the real energy attenuation, we have to take the backscattered energy into account. Wu (1982a, see appendix C) uses a simple renormalization procedure and sums up all the energy scattered into the back halfspace as the energy loss. This procedure is similar to DeWolf's "Cumulative Forward-Scatter Single-Backscatter Approximation" in calculating the backscattering strength (DeWolf 1971). Since the backscattered energy is much smaller than the forward scattered energy, the second backscattered energy (from the backward direction into the forward direction) is one order smaller than the single backscattered energy. Therefore the single backscattering loss with the renormalization of the total forward energy could be a reasonable approximation of the scattering attenuation for the harmonic wave field.

From the above analysis, in the case of strong forward scattering due to large scale inhomogeneities, the shape of the energy density decay curve is insensitive to the medium albedo B_0 and the separation of scattering attenuation from absorption becomes more difficult. However, because the scattering loss is much smaller than the isotropic case, we can have some constraint on the possible scattering attenuation from the strength of inhomogeneities. The shape of the seismogram envelope in time domain can also give constraints on the possible values of albedo B_0 . We will discuss this later in this paper.

5. SEISMIC WAVE SCATTERING AND ATTENUATION IN HINDU KUSH REGION

In this section we will calculate the energy density distribution with travel distances for the small earthquakes in the Hindu Kush region. The data used are from the digital recordings from two stations in that area. Between 11 June and 13 July, 1977, 11 smoked paper recorders and 4 digital event detector recorders were operated around the Hindu Kush Mountains of Northeastern Afghanistan. The organization and operation of the field work as well as the seismicity and tectonics of that region are described by Roecker (1981), Chatelain et al. (1980) and Roecker et al. (1982). Fig. 5.1 is the map view of the earthquake distribution and the station locations. In Fig. 5.2, the events are divided into groups with 50 km depth intervals. The digital numbered events were recorded digitally ^{on} magnetic tapes, which have been used by Roecker et al. (1982) to calculate the coda Q and S wave Q in that region using Aki's single station methods. Table 5.1 lists these events. We will use some of those events to calculate the energy distribution along the travel path.

The digital event recorders were of the event detector type (for details see Prothero 1976). When the received signal exceeded the pre-set level the recorders were triggered to record the event on magnetic tapes. The buffer of the instruments also allowed us to record one second data preceding the triggering signal. Each digital station had four seismometers, three components with high gain and a low-gain vertical component. The natural period of the seismometers was 4 seconds. The preamplifier had a gain 20 db or 40 db (low gain or high gain). The amplifier had a gain 52 db or 58 db, with a 3 pole, low-pass, antialiasing filter having a corner frequency of 32 Hz. The response of the whole system is shown in Fig. 5.3. After amplification the signal was digitized at 128 samples per second, multiplexed

and then recorded if the recorder was triggered. The events recorded usually were greater than magnitude 3, with the exception of a few close earthquakes, due the pre-set trigger level.

Because there are only a few stations, it is difficult to get the energy density-distance relation from a single event. We will use a single station method. The seismograms of different events with different distances from the station will be Fourier-transformed to get the spectral density of the energy density $E(r)$ for the corresponding source-sensor distances. In order to have a common source factor for all the events, we use the coda spectral density of these events as the reference levels. From observations, it is generally acknowledged that the coda level, at the travel time greater than twice the S wave travel time, has a very stable relation with the source energy and does not change with the locations of the events. This can be explained by the theory of coda generation in which the coda waves are assumed to be formed by the backscattered S waves from the heterogeneities in the local region of the lithosphere (Aki 1969, Aki and Chouet 1975). A received signal can be considered as a product of three factors:

$$\text{received signal} = \text{source factor} \times \text{path factor} \times \text{station factor.} \quad (5.1)$$

Because the coda energy at a specified time interval is assumed to be the sum of backscattered wave energy from the heterogeneities in all the directions, therefore the path factor has been averaged over all the directions, which is much more stable than the path factor of the direct path.

In the calculations, we took the reference coda travel time as $t_0 = 70$ sec. However, for the very close events, some seismograms are shorter than 70 sec, while for the distant events, 70 sec is smaller than twice the S wave travel times. We need to do extrapolations. The guideline for choosing coda time t_c is to have it greater than twice the S travel time and as close as

possible to 70 sec. In order to convert the coda level of each t_c to the reference level of $t_0 = 70$ sec, we use the empirical averaged coda envelope decay for each frequency obtained by Roecker (1982) for this region. When $t > 2t_s$, where t_s is the S travel time, the coda envelope decay can be fitted by

$$P(\omega|t) = P_0(\omega) \frac{1}{t^2} \exp(-b_t t), \quad (5.2)$$

where $P(\omega|t)$ is the coda power spectral density at frequency ω , at time t , $P_0(\omega)$ is a constant, b_t is the attenuation rate and

$$b_t = \beta b, \quad (5.3)$$

where b is the attenuation coefficient and β is S wave velocity. For the single backscattering model, $P_0(\omega)$ is found to be (Aki and Chouet 1975)

$$P_0(\omega) = \frac{2g(\pi)S(\omega)}{\beta}, \quad (5.4)$$

where $g(\pi)$ is the backscattering coefficient and $S(\omega)$ is the source power. For our purpose, it is not necessary to specify $P_0(\omega)$, we need only use the empirical relation (5.2). If we set $t = t_0$ as the reference coda travel time, then

$$P(\omega|t_0) = P_0(\omega) \frac{1}{t_0^2} \exp(-b_t t_0). \quad (5.5)$$

Suppose we measure the coda power $P(\omega|t_c)$ at time t_c , the correction for reducing $P(\omega|t_c)$ to $P(\omega|t_0)$ is then

$$P(\omega|t_0) = P(\omega|t_c) \left(\frac{t_c}{t_0}\right)^2 \exp[-b_t(t_0 - t_c)]. \quad (5.6)$$

We can also use $P_0(\omega)$ as the reference level:

$$P_0(\omega) = P(\omega|t_0) \cdot t_0^2 \exp(b_t t_0). \quad (5.7)$$

In Fig. 5.4, the solid line is the averaged attenuation-frequency relation obtained by Roecker, the dotted line is the smoothed version being used for calculations.

We choose two stations PEN and CHS (Fig. 5.1), because there were many close events for both stations to confine the energy-distance curves. In Table 5.2 and 5.3 the events used for calculations are listed in the order of distances. The events were located using the arrival times on smoked paper records.

To calculate the spectral density, we use the fast Fourier transform algorithm, and average the spectral densities over the specified bandwidths. In order to compare with the previous results obtained using the filtering method by other authors, we take the frequencies as octave and with bandwidths $2/3$ of the central frequencies. Table 5.4 lists the 14 central frequencies and their corresponding attenuation values. We use a 32 second window for the S wave Fourier transforms. Fig. 5.5 shows some examples of the seismograms at station PEN for different hypocenter distances, from which we can see that the 32 second window will include most of the S wave energy. In the figure, for each event first gram is the low gain vertical (Z) component, the rest are high gain in Z, E-W, and N-S components respectively. In order to avoid the Gibbs phenomena of the rectangular window, we use a 1 second cosine taper for both edges of the window. For the reference coda spectrum, we use an 8 second Hamming window for Fourier transforms.

Fig. 5.6 shows the obtained $4\pi r^2 E(r)$ curves from the station PEN. Totally 31 events are used and the events are grouped according to their distances. From left to right, the curves are of Z, EW and NS components. In the upper part, they are for $f = 0.25, 0.5$ and 1 kHz; in the middle, $f = 1.5-8$ Hz; in the bottom, $f = 12-45$ Hz. Except for the low frequencies $f < 1$ Hz, the curves can almost be fitted with straight lines. We calculated the apparent attenuations for different frequencies for the EW components and listed in the Table 5.5.

Because of the fluctuations of the measured curves and the insensitivity to albedo B_0 when $B_0 < 0.5$, we can not determine exactly the values of B_0 for each frequency. However, we can get some constraints on the B_0 values from the comparison between the measured and the theoretical curves.

Since Aki introduced the single station method using S-coda ratios to measure the apparent attenuations of short period body waves (Aki, 1980a), various attenuation mechanisms have been examined to interpret the observations, especially the frequency dependence of the apparent attenuations. After discussing different attenuation mechanisms, Aki proposed two most promising candidates: thermoelasticity and scattering (Aki 1980a). However, it seems only the scattering mechanism survived in the literature. Dainty (1981) proposed a scattering model with a constant Q medium and attributed the observed attenuation as the sum of the intrinsic attenuations and the single scattering coefficient. Assuming an intrinsic $Q_i = 2000$, he matched the observed data in Kanto, Japan by Aki (1980a) well with the theoretical calculations. Let us test this model using our theoretical calculations and the data in Hindu-Kush. Fig. 5.7 gives the possible energy density distribution curves for different frequencies if we assume the constant Q model ($Q_i = 2000$) and use the values of apparent Q in Kanto region obtained by Aki. Due to the low intrinsic attenuation at low frequencies, the medium albedo B_0 will be very high, if we attribute the observed apparent attenuations mainly to scattering. However, from Fig. 5.7 and Fig. 3.6, we see that the $E_n(r)$ curves for $B_0 = 1$ are of arch shape, only approach approximately exponential curves when distances are much greater than the extinction length L_e . Compare the prediction of Fig. 5.7 with Fig. 5.6, they do not agree in general. More detailed comparison is shown in Fig. 5.8 for the Hindu-Kush data. The apparent attenuations b obtained from the curves in Fig. 5.6 are listed in Table 5.5. For the highest frequency $f = 45$ hz,

$\hat{b} = 0.03/\text{km}$. If we assume this is totally due to the intrinsic absorption, the equivalent Q_f will be around 2500. From this Q_f , we can obtain the approximate B_0 , d_0 , and L_e for each frequency (also listed in Table 5.5) based on the measured \hat{b} values. In Fig. 5.8 the prediction of the constant Q model with $B_0 = 0.9$ is compared with the measured data of $f = 1.5$ Hz and 2 Hz. There is no match between them. Comparing with other theoretical curves of different B_0 's, we found that the observations may be fitted with curves of $B_0 < 0.5$. Since the fluctuation in the data and the insensitivity of the curve to B_0 for $B_0 < 0.5$, we can not determine the B_0 value precisely. For the frequencies above 1.5 Hz, we can have the similar conclusions (see Fig. 5.6). Therefore, the constant Q_f model may not represent the real medium in Hindu-Kush region. Because the apparent attenuations and their frequency dependence for some tectonically active regions (e.g. California, Kanto region of Japan, etc.) are alike, we might expect that these analyses would be applicable to that region. However, we need to apply the method to other regions before we can draw any conclusions.

More careful studies are needed for the energy distribution curves of low frequencies ($f < 1$ Hz). The curves at these frequencies (Fig. 3.6) have the interesting arch shapes, which might indicate the existence of strong scattering at these frequencies. However, these curves are more fluctuating, which may be caused by the interference, and therefore are less reliable. Another consideration is the influence of surface waves and guided waves (higher mode Rayleigh and Love waves), which is stronger at low frequencies. Fig. 5.9 shows two examples of seismograms of events having distances about 100 km from the station (A34: $r = 104$ km, depth = 4.57 km; A08: $r = 124$ km, depth 16.27 km). The strong low frequency components following immediately the S arrivals are apparent. This may evidence the strong multiple scattering

t these low frequencies. Another positive ^{view}indicate of multiple scattering is emerged when we compare with the decay curves of direct S amplitudes. In Fig. 5.10 these decay curves are shown for $f = 0.25, 0.5, \text{ and } 1 \text{ hz}$, the S wave power spectra are calculated by Fourier transform using a 4 second Hamming window. These curves are more regular and are not of arch shape. That is because when the window for S wave is very narrow, the multiple-scattered waves, which have longer travel times, are not included. In 5.11 we also plot the calculated apparent attenuations from both the direct S and the total S decay curves for comparisons (the smoothed coda attenuation curve is also plotted). Above 1.5 hz, the attenuation of the total S wave is smaller than that of the direct S wave. This may be due to the inclusion of part of the scattered energy in the former case. However, the differences between these two cases are small in general, which further suggest that, the scattering is not the dominant factor in the apparent attenuation for these frequencies. Again a noticeable different behavior at low frequencies ($f < 1.5 \text{ hz}$) is presented. For these frequencies, the attenuations of direct S waves are smaller than that of the total S waves. Note that the attenuations of the total S waves are estimated from only the later part of the energy distribution curves.

If we take the energy curves for $f < 1 \text{ hz}$ as controlled by multiple scattering. A rough estimation by comparing with the theoretical curves (Fig. 3.6) can be made about the medium scattering parameters. For the vertical component, we have

f	$L_e(\text{km})$	B_0	$L_s(\text{km})$	$L_a(\text{km})$	$Q_1(\text{equivalent})$
0.25	33.3	0.99	33.7	3330	1494
0.5	28.3	0.99	28.6	2830	2540
1	50	0.9	56	500	898

In the case of the EW component,

f	L_e (km)	B_0	L_s (km)	L_a (km)	Q_i (equivalent)
0.25	25	0.99	25.3	2500	1122
0.5	26.7	0.99	26.9	2670	2396
1	40	0.90	44	400	718

It is interesting to note that, at 0.25 and 0.5 hz, the estimated Q_i are close to the proposed intrinsic Q for the constant Q model. Although this may be only a numerical coincidence, we would like to report it here for further study.

Fig. 5.12 shows the 4 r E(r) curves obtained from station CHS. The events used are listed in Table 5.3. The general conclusions drawn from the analysis of the results of station PEN hold true also for CHS.

6. DIFFUSION APPROXIMATION IN TIME DOMAIN, THE CONSTRAINT OF SEISMOGRAM ENVELOPE ON THE SCATTERING STRENGTH

Another approach for studying the scattering and attenuation of seismic waves is to formulate the problem of energy transfer in the time domain and compare the envelopes of seismograms with the theoretical predictions. However, from the author's knowledge, the complete solution of energy transfer in time domain is not available at present. Nevertheless, there are approximate solutions for the weak scattering and the strong scattering. In the weak scattering case, when the propagation distance is smaller than the scattering mean free path, the single scattering approximation can be used. Aki and Chouet (1975) developed a single backscattering model, Sato (1977) derived the formulation for isotropic scattering and discussed subsequently the influence of non-isotropic scattering (Sato 1982). In the case of strong scattering, when the scattering coefficient is much greater than the absorption coefficient ($B_0 \gg 0.5$), and the propagation distance is much greater than the scattering mean free path, the diffusion approximation can be used to approximate the envelope variation in time domain. In the following, we discuss the diffusion approximation and seek the constraint of the observed envelopes on the medium scattering properties.

When the scattering mean free path is much shorter than the absorption length in the medium, the energy transfer can be approximated by a diffusion equation (see Morse and Feshbach, 1953, §2.4)

$$\frac{\partial}{\partial t} P(r,t) = d\nabla^2 P(r,t) - b_t P(r,t) + q(t), \quad (6.1)$$

where $P(r,t)$ is the power at distance r and time t ; b_t is the absorption rate

$$b_t = bc,$$

where b is the absorption coefficient and c is the wave velocity; $q(t)$ is the source; and d is the diffusivity

$$d = \frac{c}{3\eta_d}, \quad (6.3)$$

where η_d is the effective extinction coefficient for the diffusion process. In the case of isotropic scattering $\eta_d = \eta_e$. For non-isotropic scattering, in the case of discrete random media

$$\eta_d = n\sigma_a + n\sigma_m, \quad (6.4)$$

where n is the number density of the scatterers, σ_a is the absorption cross-section of the scatterers, σ_m is defined by

$$\sigma_m = \int_{4\pi} \hat{\sigma}_d(\hat{\Omega})(1 - \cos\theta)d\Omega, \quad (6.5)$$

where $\hat{\sigma}_d(\hat{\Omega})$ is the differential scattering cross-section (2.15), θ is the scattering angle. σ_m is called the "momentum transfer cross section" by Morse and Feshbach (1953, p. 188). The solution of (6.1) for a point impulsive source is (Morse and Feshbach, 1953)

$$P(r, t) = \begin{cases} 0, & t < 0 \\ \frac{1}{(4\pi dt)^{3/2}} \exp[-(r^2/4dt) - b_t t], & t > 0 \end{cases} \quad (6.6)$$

Ishimaru (1978) formulated the problem using the equations for the two-frequency mutual coherency function and derived the two-frequency equation of transfer. Under the diffusion approximation, a solution similar to (6.6) for a point impulsive source was obtained

$$P(r, t) = \frac{r}{\sqrt{4\pi d} t^{3/2}} \exp[-(r^2/4dt) - b_t t], \quad (6.7)$$

where d is the same as (6.3), but with η_d defined by

$$\eta_d = n\sigma_m, \quad (6.8)$$

instead of (6.4). However, since σ_a is assumed very small, there will be no big difference between (6.8) and (6.4) except for very strong forward scattering. In the following we will discuss the case of $\sigma_m \gg \sigma_a$, therefore

(6.8) will be used, which can be written as

$$\eta_d = \eta_s (1 - \bar{\gamma}), \quad (6.9)$$

where η_s is the scattering coefficient, and $\bar{\gamma}$ is the mean scattering angle cosine

$$\begin{aligned} \bar{\gamma} &= \frac{1}{\sigma_s} \int \hat{\sigma}_d(\Omega) \cos\theta \, d\Omega \\ &= \frac{1}{4\pi} \int \hat{D}(\Omega) \cos\theta \, d\Omega, \end{aligned} \quad (6.10)$$

where $\hat{D}(\Omega)$ is the scattering directivity (2.11).

Note that, the quantity

$$\eta_s \bar{\gamma} = \frac{\eta_s}{4\pi} \int_0^\pi \int_0^{2\pi} D(\theta, \phi) \cos\theta \sin\theta \, d\phi \, d\theta, \quad (6.11)$$

where θ, ϕ constitute the spherical coordinates with the polar axis in the incident direction, is the net scattering power flux in the incident direction. This part of the scattered power will join the incident power flow, and does not contribute to the diffusion process. In the case of isotropic scattering, $\bar{\gamma} = 0$, the net scattering power flow in the incident direction is zero, so that $\eta_d = \eta_s$. In the case of strong backscattering, $-1 < \bar{\gamma} < 0$, so $\eta_d > \eta_s$. Vice versa, for the case of strong forward scattering, $0 < \bar{\gamma} < 1$, $\eta_d < \eta_s$.

From (6.6), we know there is a peak in the power flow curve, which is approximately at the maximum of the exponent of the exponential term, i.e. at

$$\begin{aligned} t_m &= r \frac{1}{\sqrt{4dbt}} = t_0 \frac{\sqrt{3}}{2} \frac{\tau_a}{\sqrt{1-\bar{\gamma}}} \frac{\tau_a}{\tau_s} = t_0 \frac{\sqrt{3}}{2} \frac{\eta_d}{\eta_s} \\ &= t_0 \frac{\sqrt{3}}{2} \frac{\sqrt{B_0}}{1-\bar{\gamma}} \frac{B_0}{1-B_0} \end{aligned} \quad (6.12)$$

where

$$t_0 = r/c, \quad (6.13)$$

and

$$\tau_a = 1/b_t, \quad \tau_s = 1/\eta_s c, \quad (6.14)$$

are the absorption time and the scattering mean free time respectively.

Therefore, the arrival time of the peak of the power flow is proportional to the square root of the ratio between the absorption time and the scattering

mean free time. For strong forward scattering, $\sqrt{1-\bar{\gamma}} < 1$, the power peak will arrive earlier than the case of isotropic scattering; in the case of strong backscattering, $\sqrt{1-\bar{\gamma}} > 1$, the peak will arrive later.

Note that, under diffusion approximation, the apparent attenuation, when $t \tau_s \gg t_0^2$, is approaching to the absorption coefficient η_a ; while in the exact solution in frequency domain (3.16) it approaches $\omega \eta_e$ or $\eta_a + d_s \eta_s$. The multiplier d_0 or d_s varies depending on B_0 . Only in the case of $B_0 \rightarrow 1$, the apparent attenuation approaches η_a .

From the peak time we can derive the ratio η_d/η_a after doing correction of $t^{3/2}$, while measuring apparent attenuation will determine approximately η_a . Therefore the shape of the envelope provides all the parameters of diffusion scattering.

If we assume a constant Q model, from table 5.5, we have $B_0 > 0.79$ for $f < 6$ Hz. Therefore, the diffusion approximation could be applied to the wave energy transfer for frequencies below 6 Hz. Based on the estimated scattering parameters in Table 5.5, we list in Table 6.1 the predicted arrival times of peak power for different frequencies. Except for the strong forward scattering case, the peak arrival times have a large delay up to several times of the direct travel time. This contradicts the observations on earthquake seismograms or explosion-source seismograms on the earth. The travel time fluctuations for local earthquakes are usually less than 10-20% and the direct S waves can be easily recognized for these frequencies in general. The

observed seismograms are not of diffusion type in the frequency range 1-10 hz. Fig. 6.1 shows the diffusion type envelope curves according to (6.6) at $f = 2$ hz for different scattering patterns (the envelopes should be symmetric about the time axis). Since we neglected the $t^{-3/2}$ term in deriving (6.12), the peak times in Fig. 6.1 are different from the predictions in Table 6.1.

However, the envelopes exhibit the typical diffusion characteristics. These diffusion type envelopes have been observed on the moonquake seismograms and on the seismograms of model experiments in laboratories. In Fig. 6.2, the 3-component seismograms for two events on the moon are shown (the figures are from Latham et al. 1971). The first event (upper seismograms) is believed to be a meteoroid impact, corresponding to the case of shallow source; the second event is considered to be a deep moonquake (below the strong scattering layer). These diffusion type seismograms are due to the existence of the high Q, strong scattering layer below the moon surface (Dainty et al., 1974, Dainty and Toksoz, 1981). Fig. 6.3 shows the seismograms from the model experiment in the laboratory (Dainty et al., 1974). (a) is the seismogram with a homogeneous plate as the propagation medium; while (b) shows the diffusion type seismogram for the case when the plate has many grooves as scatterers.

In order to compare with Fig. 6.1, we select two events A06 (Depth 103 km) and A15 (depth 118 km), which have distances around 200 km from station PEN and CHS. From Fig. 3.9 we know that, the diffuse term will dominate after the travel distance exceeds twice the extinction distance for $B_0 = 0.9$. Therefore the seismograms for these two events should be of diffusion type, if the parameters in Table 6.1 are true, i.e. the constant Q model is true. Fig. 6.4 and 6.5 show the filtered seismograms for these two events at different stations. The digital filter is a six pole, zero-phase, Butterworth filter, the central frequencies are 0.375, 0.75, 1.5, 3, 6, 12, 24, and 46 hz, the

bandwidth is 2/3 of the central frequency for each band (see Roecker, 1982). From these figures, we do not see the diffusion type seismograms at low frequencies. In Fig. 6.6 we plot the envelope decay curves for event A15 as an example. The power decay curves are calculated by the moving window spectral analysis with an 8 second Hamming window and at a 5 second interval. On the left are the vertical components, right, the EW components. These envelope curves are typical for the events in this region (see Roecker 1982). They are not of diffusion type except for some very high frequency components ($f > 20$ hz, we will discuss this later). In fact these curves fit the single isotropic model fairly well. The energy density $E(r,t)$ of the isotropically scattered body waves at time t and at distance r from a point source can be expressed as (Sato 1977)

$$E(r,t) = \frac{n\sigma_s W_0}{4\pi r^2} K\left(\frac{t}{t_s}\right), \quad (6.15)$$

where t_s is the direct wave (here S wave) travel time, n , the number density and σ_s the scattering cross-section of the scatterers. W_0 is the source factor, and

$$K(\xi) = \frac{1}{\xi} \ln \left[\frac{\xi+1}{\xi-1} \right]. \quad (6.16)$$

The time function $K(t/t_s)$ is a pure geometric spreading factor for the single isotropic scattering model, which is plotted in Fig. 6.7 for the distance of event A15 to CHS ($r=221.85$ km). Fig. 6.8 shows the power decay curves after making the corresponding geometric spreading correction, i.e. dividing the curves in Fig. 6.6 by $K(t/t_s)$. We can see that, after this geometric correction, the power decay curves are fairly linear, which is of exponential decay due to attenuation.

To compare with Fig. 6.1, we need to examine the case of strong forward scattering more carefully. The curve of $\bar{\gamma}=0.5$ is calculated by assuming the same scattering coefficient η_s as the isotropic scattering case. Because more energy is concentrated in the forward direction, the effective scattering coefficient for diffusion η_d becomes smaller than η_s (see (6.9)). In our case we estimated η_s from the apparent attenuation measurement in frequency domain (section 5). Since we calculated the power spectral densities for the total S waves, the net scattering power flux (6.11) is included, so that the forward scattering power flux does not contribute to the apparent attenuation. Therefore, the estimated scattering coefficient is closer to η_d than to η_s , if we consider the apparent attenuation is mainly due to the scattering loss. By this consideration, the curve for strong forward scattering in Fig. 6.1 should have a shape close to the isotropic case with a η_d closer to, but a η_s greater than the isotropic case. Secondly, if the peak of the power flow is near the direct arrival time, the more elaborated diffusion formulae should be appealed (Ishimaru 1978), which will incorporate the direct travel time into the formulation. At any rate, if the apparent attenuation obtained in section 5 is taken as mainly from scattering loss, the envelope curve should be similar to a diffusion type curve of isotropic scattering.

From above comparison and analysis, combining with the results obtained in section 5, we can conclude that, in the frequency range 1.5-20 hz, the scattering is not the dominant factor of the measured apparent attenuation. In other words, the scattering coefficients is smaller than the absorption coefficients at these frequencies in the lithosphere of this region.

More careful study is also needed for the case of frequencies higher than 20 hz. From Fig. 6.4, 6.5 we notice that, at these high frequencies the seismograms become spindle-shaped as pointed out by Tsujura and Aki (see Aki

1980b). These are of diffusion type. For some stations, the P and S phase can no longer be clearly separated, which means also strong scattering and conversion. Since the attenuation coefficients are high at these frequencies, the scattering coefficients must be also high. This strong scattering for high frequencies may be caused by the near surface very small scale heterogeneities. Regarding Fig. 6.6, 6.8, we can find that the decay curves of m and n band ($f=32$ and 45 hz) have flat tops, different from the other bands.

The time domain analysis has the advantage of easy comparison with the data, because each seismogram is one experiment, unlike the energy density distribution curve in frequency domain, which need many events covering a distance range. However, in order to perform more complete analysis, we need to develop more accurate theory and model. Besides, the shape of the envelope is also sensitive to the slip direction of the earthquake source, that makes the analysis more complicated. At any rate, the combinations of time domain and frequency domain analysis will make the analysis more informative and reliable.

7. SUGGESTION FOR FURTHER STUDIES

It is interesting and beneficial to apply the method to other regions to see the relative importance of absorption and scattering for different regions. Especially the comparison between the results for the tectonically stable regions, such as New England area or the central U.S., and that for the active regions such as the results obtained here for Hindu Kush or that for California, will give us deeper understanding about scattering and attenuation as well as more information about the tectonic activities.

Further improvements on the scattering theory and modeling are also needed, such as the influences of the radiation pattern of the source, the finite thickness of the lithosphere, the nonisotropy of the inhomogeneities, etc. Of course, full treatment of elastic wave scattering in both the frequency domain and the time domain are highly desired.

References

- Aki, K., 1969, Analysis of the seismic coda of local earthquakes as scattered waves, *J. Geophys. Res.*, 74, 615-631.
- Aki, K., 1973, Scattering of P waves under the Montana Lasa, *J. Geophys. Res.*, 78, 1334-1346.
- Aki, K., 1980a, Attenuation of shear waves in the lithosphere for frequencies from 0.05 to 25 Hz, *Phys. Earth Planet. Int.*, 21, 50-60.
- Aki, K., 1980b, Scattering and attenuation of shear waves in the lithosphere, *J. Geophys. Res.*, 85, 6496-6504.
- Aki, B. and B. Chouet, 1975, Origin of coda waves: source, attenuation and scattering effects, *J. Geophys. Res.*, 80, 3322-3342.
- Barabanenkov, Y.N., 1969, On the spectral theory of radiation transport equations, *Sov. Phys., JETP*, 29, 679-684.
- Bell, G.I. and S. Glasstone, 1970, *Nuclear Reactor Theory*, New York, Van Nostrand Reinhold.
- Berteussen, K.A., A. Christoffersson, E.S. Husebye, and A. Dahle, 1975, Wave scattering theory in analysis of P wave anomalies at NORSAR and LASA, *Geophys. J. Roy. astr. Soc.*, 42, 403-417.
- Capon, J., 1974, Characterization of crust and upper mantle structure under Lasa as a random medium, *Bull. Seis. Soc. Am.*, 64, 235-266.
- Carrier, G.F., M. Krook and C.E. Pearson, 1966, *Functions of a complex variable*, ch. 7, McGraw-Hill, New York.
- Chandrasekhar, S., *Radiative Transfer*, Dover, 1960 (revised version of 1950).
- Chatelain, J.L., S.W. Roecker, D. Hatzfeld, and P. Molnar, 1980, Microearthquake seismicity and fault plane solutions in the Hindu Kush region and their tectonic implications, *J. Geophys. Res.*, 85, 1365-1387.

- Chernov, L.A., 1960, *Wave Propagation in a Random Medium*, McGraw-Hill, New York.
- Chouet, B., 1979, Temporal variations in the attenuation of earthquake coda near Stone Canyon, California, *Geophys. Res. Lett.*, 6, 3.
- Dainty, A.M., A scattering model to explain seismic Q observations in the lithosphere between 1 and 30 Hz, *Geophys. Res. Lett.*, 8, 1126-1128, 1981.
- Dainty, A.M., M.N. Toksoz, K.R. Anderson, P.J. Pines, Y. Nakamura, and G. Latham, Seismic scattering and shallow structure of the moon in oceanus procellarum, *Moon*, 9, 11-29, 1974.
- Dainty, A.M. and M.N. Toksoz, 1981, Seismic codas on the earth and the moon: a comparison, *Phys. Earth Planet. Int.*, 26, 250-260.
- Dashen, R., 1979, Path integrals for waves in random media, Stanford Research Inst. Tech. Report JSR 76-1, also *J. Math. Phys.*, 20, 894-920 (1979).
- Davison, B., 1957, *Neutron Transport Theory*, Oxford Univ. Press, London.
- Del Pezzo, E., F. Ferulano, A. Giarusso, and M. Martini, 1983, Seismic coda Q and scaling law of the source spectra at the Aeolian Islands, Southern Italy, *Bull. Seis. Soc. Am.*, 73, 97-108.
- DeWolf, D.A., 1971, Electromagnetic reflection from an extended turbulent medium: cumulative forward-scatter single-backscatter approximation, *IEEE Trans. Ant. Prop.*, AP-19, 254-282.
- Fante, R.L., 1973, Propagation of electromagnetic waves through turbulent plasma using transport theory, *IEEE Trans. Ant. and Prop.*, AP-21, 750-755.
- Flatte, S.M., R. Dashen, W.H. Munk, K.M. Watson, and F. Zachariasen, *Sound transmission through a fluctuating ocean*, Cambridge Univ. Press, 1979.

- Frisch, V., 1968, Wave Propagation in Random Media, Probabilistic Methods in Applied Mathematics, Vol. 1, Academic Press, New York, 76-198.
- Gao, L.S., L.C. Lee, N.N. Biswas and K. Aki, 1983, Comparison of the effects between single and multiple-scattering on coda waves for local earthquakes, Bull. Seis. Soc. Amer., 73, 377-389.
- Gao, L.S., N.N. Biswas, L.C. Lee and K. Aki, 1984, Effects of multiple scattering on coda waves in three-dimensional medium, to be published.
- Hoffman, W.C., 1964, Wave propagation in a general random continuous medium, Proc. Symp. Appl. Math., 16, 117-144.
- Ishimaru, A., 1975, Correlation functions of a wave in a random distribution of stationary and moving scatterers, Radio Sci., 10, 45-52.
- Ishimaru, A., 1977, Theory and application of wave propagation and scattering in random media, Proc. of IEEE, 65, 1030-1061.
- Ishimaru, A., 1978, Wave propagation and scattering in random media, V. 1 and 2, Academic Press, New York.
- Ishimaru, A., 1978, Diffusion of a pulse in densely distributed scatterers, J. Opt. Soc. Am., 68, 1045-1050.
- Jerlov, M.G., 1976, Marine Optics, Elsevier, New York.
- Jin, A.S., Coda, I. Durations and backscattering coefficients, Acta Geophysica Sinica (in Chinese), in press, 1983.
- Kay, I. and R.A. Silverman, 1958, Multiple scattering by a random stack of dielectric slabs, Nuovo Cimento (10) 9, suppl., 625-645.
- Kong, J.A., Tsang, L. and R. Shin, 1984, Theory of Microwave Remote Sensing, Wiley-Interscience, New York.
- Kopnichev, Y.F. 1977, The role of multiple scattering in the formation of a seismogram's tail, Izvestiya Academy of Science, USSR, Physics of the Solid Earth, 13, 394-398.

- Latham, G.V., M. Ewing, J. Dorman, D. Lammlein, F. Press, N. Toksoz, G. Sutton, F. Duennebier, and Y. Nakamura, 1971, Moonquakes and lunar tectonism, *Science*, 174, 687-692.
- Lin, J.C. and A. Ishimaru, 1974, Multiple scattering of waves by a uniform random distribution of discrete isotropic scatterers, *J. Acoust. Soc. Am.*, 56, 1995-1700.
- Mason, W.P., 1969, Internal friction mechanism that produces an attenuation in the earth's crust proportional to frequency, *J. Geophys. Res.*, 74, 4963-4966.
- Mason, W.P., 1971, Internal friction at low frequencies due to dislocation: applications to metals and rock mechanics, in *Physical Acoustics*, v. 8, W.P. Mason and R.N. Thurston, eds., Academic Press, New York.
- Menzel, D.H., ed., 1966, *Selected Papers on the Transfer of Radiations*, New York, Dover.
- Morse, P.M. and H. Feshbach, 1953, *Methods of Theoretical Physics*, New York, McGraw-Hill.
- O'Doherty, R.F. and N.A. Anstey, 1971, Reflections on amplitudes, *Geophys. Prospecting*, 19, 430-458.
- Rautian, T.G. and V.I. Khalturin, 1978, The use of coda for determination of the earthquake source spectrum, *Bull. Seis. Soc. Am.*, 68, 923-948.
- Rhea, S., 1983, Analysis of digital data from local Charleston, S.C., earthquakes, *Earthquake Notes*, 54, 32.
- Richard, P.G. and W. Menke, 1983, The apparent attenuation of a scattering medium, *Bull. Seis. Soc. Am.*, 73, 1005-1021.
- Roecker, S.W., 1981, Seismicity and tectonics of the Pamir-Hindu Kush region of central Asia, Ph.D. Thesis, Massachusetts Institute of Technology, Cambridge, MA.

- Roecker, S.W., B. Tucker, J. King, and D. Hatzfeld, 1982, Estimates of Q in central Asia as a function of frequency and depth using the coda of locally recorded earthquakes, *Bull. Seis. Soc. Am.*, 72, 129-149.
- Sato, H., 1977, Energy propagation including scattering effect; single isotropic scattering approximation, *J. Phys. Earth*, 25, 27-41.
- Sato, H., 1982a, Coda wave excitation due to nonisotropic scattering and nonspherical source radiation, *J. Geophys. Res.*, 87, 8665-8674.
- Sato, H., 1982b, Attenuation of S waves in the lithosphere due to scattering by its random velocity structure, *J. Geophys. Res.*, 87, 7779-7785.
- Schuster, A., 1905, Radiation through a foggy atmosphere, *Astrophys. J.*, 2, 1-22.
- Sobolev, V.V., 1963, *A Treatise on Radiative Transfer*, Princeton, NJ, Van Nostrand.
- Suyehiro, S., 1968, Change in earthquake spectrum before and after the Matsushiro Swarm, *Papers in Meteorology and Geophysics*, 19, 3, 427-435.
- Tatarskii, V.I., 1971, The effects of the turbulent atmosphere on wave propagation.
- Tricomi, F.G., 1957, *Integral Equations*, New York, 22-26.
- Tsang, L. and A. Ishirau, 1983, Backscattering enhancement for random discrete scatterers, to be published.
- Turpening, R., 1984, Differential vertical seismic profiling: fracture volume analysis in "Vertical seismic profiling", ed. by Balch, A. and M. Lee, I.H.R.D.C., Boston.
- Usciuski, B.J., 1977, *The elements of wave propagation in random media*, McGraw-Hill.
- Walsh, J.B., 1966, Seismic wave attenuation in rocks due to friction, *J. Geophys. Res.*, 71, 2591-2599.

- Winkler, K., A. Nur, and M. Gladwin, 1979, Friction and seismic attenuation in rocks, *Nature*, 227, 528-531.
- Wu, R.S., 1980, The attenuation of seismic waves due to scattering in a random medium (abstract), *EOS*, 61, 46, 1049.
- Wu, R.S., 1982a, Attenuation of short period seismic waves due to scattering, *Geophys. Res. Lett.*, 9, 9-12.
- Wu, R.S., 1982b, Mean field attenuation and amplitude attenuation due to wave scattering, *Wave Motion*, 4, 305-316.
- Wu, R.S., and K. Aki, 1984, Scattering characteristics of elastic waves by an elastic heterogeneity, *Geophysics*, in press.
- Wu, R.S. and K. Aki, 1984, Elastic wave scattering by a random medium and the small scale inhomogeneities in the lithosphere, *J. Geophys. Res.*, in press.
- Yildiz, A., 1984, Macroscale attenuation of seismic waves, preprint.
- Zuniga, M., J.A. Kong and L. Tsang, 1980, Depolarization effects in the active remote sensing of random media, *J. Appl. Phys.*, 51, 2315-2325.

Table 3.1. The Diffuse Multipliers d_o and d_s

B_o	0.1	0.2	0.3	0.4	0.5	0.6	0.7	0.8	0.9	0.95	0.99
d_o	0.997	0.987	0.969	0.944	0.910	0.866	0.807	0.728	0.611	0.519	0.374
d_s	0.97	0.94	0.90	0.86	0.82	0.78	0.72	0.66	0.57	0.49	0.37

Table 5.1

DATE	ORIGIN TIME	LAT N MIN	LON E MIN	DEPTH (KM)	EVENT NO.	MAG
77 616	1616	55.26 36	31.75 70	16.13	102.26	16 3.9
77 617	8 6	32.45 35	23.30 69	28.05	1.49	18 2.4
77 617	1714	20.46 36	32.89 70	57.20	197.00	19 3.8
77 617	1930	38.16 35	43.12 69	40.23	77.98	20 3.7
77 617	22 1	47.14 36	30.00 71	14.24	112.19	21 3.6
77 618	528	43.58 34	54.80 69	55.45	1.87	23 2.5
77 618	753	35.31 34	39.56 70	34.71	1.42	24 2.4
77 618	9 3	40.71 34	34.30 72	48.84	340.70	25 5.3
77 618	1150	22.64 36	6.23 69	23.71	131.94	26 3.3
77 618	2320	3.27 35	59.24 70	38.49	112.21	27 3.5
77 620	148	49.52 36	5.63 70	26.43	98.55	28 4.3
77 620	4 5	56.23 36	7.01 70	26.17	105.32	29 4.0
77 620	1156	30.60 36	30.35 70	18.96	215.02	30 3.8
77 620	2335	16.51 35	30.68 69	3.71	2.50	31 3.1
77 621	316	2.84 36	38.92 71	18.30	98.13	32 3.7
77 621	2133	46.80 36	33.34 71	22.42	159.81	33 4.3
77 622	832	21.95 36	35.21 70	53.23	232.49	02 4.1
77 622	1430	58.92 36	10.33 69	19.52	4.57	34 3.9
77 623	934	59.59 36	27.15 71	14.84	135.57	03 3.5
77 623	2054	13.26 36	2.75 70	32.94	106.25	04 3.5
77 624	2358	0.19 36	31.68 70	22.24	218.37	05 4.6
77 624	2243	57.24 36	11.90 69	17.27	9.65	35 3.3
77 626	824	11.00 36	18.48 70	55.67	119.35	36 3.4
77 626	1833	58.79 36	47.06 71	23.74	155.28	37 3.5
77 627	759	14.12 36	27.83 70	50.11	127.75	38 3.3
77 628	1034	26.75 36	7.25 70	32.94	100.00	39 3.6
77 628	1520	4.70 36	10.48 71	8.95	86.02	40 2.9
77 628	1623	51.79 37	11.54 71	25.61	108.66	41 3.4
77 628	17 3	36.25 35	17.53 69	16.85	8.68	42 2.1
77 629	636	27.30 36	21.49 71	10.14	105.56	43 3.5
77 629	1031	4.37 36	28.76 71	18.43	138.44	44 3.4
77 629	1521	33.18 37	27.39 72	21.65	221.95	45 4.3
77 629	1540	1.48 34	46.64 70	56.55	2.04	46 2.5
77 629	16 6	30.59 36	24.00 71	9.33	103.31	06 4.7
77 630	220	47.74 36	29.06 70	26.98	219.25	07 4.1
77 630	338	34.03 36	37.07 71	17.14	86.83	47 3.5
77 630	1353	29.92 36	17.64 71	11.71	98.23	48 3.4
77 7 1	348	32.15 34	38.56 70	28.55	16.27	08 4.5
77 7 1	1444	10.80 36	28.05 71	6.59	264.91	09 4.9
77 7 1	1627	3.09 36	14.56 70	19.05	108.83	49 3.0
77 7 2	330	48.81 36	34.45 70	39.80	174.84	50 4.1
77 7 2	2028	19.63 35	13.97 69	25.26	8.32	51 2.2
77 7 2	2111	49.19 35	59.39 70	43.29	93.93	52 3.2
77 7 3	17 0	4.91 36	56.43 71	2.82	76.67	53 3.0
77 7 4	614	15.39 36	32.71 71	21.16	122.09	54 3.5
77 7 4	824	3.03 36	19.90 69	33.71	134.72	55 3.6
77 7 4	1128	47.08 36	26.39 70	12.86	221.59	10 4.6

77	7	4	2041	5.58	36	11.73	69	26.72	128.00	56	3.3
77	7	4	21 1	56.74	37	31.97	72	0.62	157.19	11	4.7
77	7	5	14 7	12.46	36	29.72	69	47.10	271.19	57	2.9
77	7	6	055	22.50	36	39.45	71	5.04	229.10	58	3.9
77	7	6	1328	56.27	37	4.49	71	34.93	96.33	59	3.4
77	7	6	1659	8.76	36	17.72	69	50.94	9.46	60	3.0
77	7	7	620	43.34	36	25.26	70	37.26	228.86	61	4.1
77	7	8	130	36.15	36	38.20	71	8.46	214.61	12	4.0
77	7	8	525	26.60	36	41.86	71	12.24	230.79	13	4.7
77	7	8	7 2	10.28	36	31.90	71	20.23	94.37	62	3.3
77	7	8	950	6.99	36	41.21	71	12.71	233.80	63	3.8
77	7	9	1141	13.94	35	30.46	68	52.81	38.00	64	2.7
77	7	9	1211	40.56	37	36.71	71	45.78	129.68	65	3.7
77	7	9	1616	39.67	36	28.06	71	12.71	143.71	66	3.3
77	7	10	028	19.08	35	41.93	68	38.41	3.74	67	3.6
77	7	10	1347	18.52	35	6.83	69	21.09	17.57	69	2.3
77	7	10	1612	22.07	35	31.28	69	13.05	17.04	70	3.6
77	7	11	11 2	56.61	36	26.37	71	20.63	104.40	14	3.9
77	7	11	1224	5.07	36	45.50	71	28.64	188.43	72	3.6
77	7	11	1651	7.33	36	28.89	71	9.82	118.48	15	4.2
77	7	12	11 7	59.16	36	32.53	70	58.27	192.49	73	4.3
77	7	12	1518	28.82	36	12.21	69	15.96	5.57	74	3.8
77	7	12	1718	2.32	36	16.59	70	40.23	103.88	75	3.7

Table 5.2

Events Used in the Calculations for PEN in the Order of Distances (31 events)

Point No. in curve	Event No.	Distance (km)	Depth (km)	Magnitude	P travel time (sec.)	S travel time (sec.)	Reference coda time t_c (sec.)	Record length (sec.)
1	A42	11.12	8.68	2.1	7.29	11.83		44
	A51	12.10	8.32	2.2	7.54	12.26	31.5	34
2	A69	21.52	17.57	2.3	7.54	12.52	31.5	40
	A18	22.03	1.49	2.4	9.55	15.62	20.5	18
3	A70	37.76	17.04	3.6	10.10	17.03	34.1	38
	A31	39.15	2.5	3.1	11.67	19.42	41.7	40
4	A64	63.09	38.0	2.7	11.42	19.79	40.4	38
	A23	65.15	1.87	2.5	15.04	25.38	42.0	36
5	A67	80.75	3.74	3.6	16.86	28.66	60.7	60
6	A20	100.16	77.98	3.7	15.94	27.87		54
	A34	104.68	4.57	3.9	19.81	33.91	73.8	82
	A35	107.97	9.65	3.3	19.67	33.76		68
	A74	108.33	5.57	3.8	20.16	34.56		80
7	A08	124.88	16.27	4.5	21.06	36.39		158
	A68	175.74			24.21	42.61		60
8	A04	178.52	106.25	3.5	24.78	43.42	78.7	70
	A39	179.28	100.0	3.6	24.9	43.56		64
9	A16	196.42	102.36	3.9	27.16	47.47	84.0	70
	A75	197.95	103.88	3.7	27.36	47.83		64
10	A06	234.53	103.31	4.7	31.95	55.72	105.9	134
	A15	247.35	118.48	4.2	33.41	58.51	107.5	158
11	A03	259.49	136.57	3.5	34.71	61.11		62
	A50	295.83	174.84	4.1	34.46	61.07		90
12	A10	271.40	221.59	4.6	35.57	63.1	109.4	258
	A05*	278.65	218.87	4.6	36.52	64.75		234
	A07	279.0	219.25	4.1	36.56	64.82	100.5	76
	A73	283.65	192.49	4.3	37.22	65.96		90
13	A02	310.97	232.49	4.1	40.23	71.32	102.1	78
14	A13*	329.59	230.79	4.7	42.47	75.29		246
	A09*	339.32	264.91	4.9	43.36	77.06		302
15	A25	472.39	340.70	5.3	58.59	104.48	132.2	96

*high gain records were clipped, only low gain vertical component has been used.

Table 5.3

Events Used in the Calculations for CHS in the Order of Distances (22 events)

Point No. in curve	Event No.	Distance (km)	Depth (km)	Magnitude	P travel time (sec.)	S travel time (sec.)	Record Length (sec.)
1	A46	8.47	2.04	2.5	1.55	2.63	
2	A24	47.77	1.42	2.4	12.85	21.48	
	A08	59.54	16.27	4.5	12.98	22.09	
3	A04	181.43	106.25	3.5	27.08	42.69	
	A28	184.08	98.55	4.3	25.55	44.64	
	A39	184.42	100.00	3.6	28.59	44.74	
	A29	189.83	105.32	4.0	26.9	46.03	
4	A06	206.22	103.31	4.7	28.42	49.64	
	A14	211.85	104.40	3.9	29.54	50.88	
	A34	220.58	4.57	3.9	34.71	60.37	
	A15	221.85	118.48	4.2	30.33	53.19	
	A74	226.84	5.57	3.8	35.41	61.63	
	A16	230.02	102.26	3.9	31.4	54.74	
	A66	235.26	143.71	3.3	31.33	56.0	
5	A50	266.53	174.84	4.1	34.67	60.89	
	A73	273.54	192.49	4.3	35.65	61.65	
6	A12	296.55	214.61	4.0	38.17	65.84	
	A10	297.63	221.59	4.6	37.62	65.62	
	A05	298.40	218.87	4.6	39.10	65.58	
7	A02	306.54	232.49	4.1	39.11	66.00	
	A09	323.59	264.91	4.9	41.13	70.13	
8	A11	352.37	157.19	4.7	46.24	78.24	

Table 5.4 The Central frequencies used and the corresponding attenuation values of coda waves

Band no.	Central frequency	Coda Q_c (observed)	Coda Q_c (smoothed)	Coda b_t (observed)	Coda b_t (smoothed)	Coda b (smoothed)
a	0.25	24.0	24.0	6.5×10^{-2}	6.5×10^{-2}	1.86×10^{-2}
b	0.5	47.9	44.2	6.6	7.10	2.03
c	1	83.2	81.0	7.6	7.76	2.22
d	1.5	89.1	115.4	10.6	8.17	2.33
e	2	107.2	148.3	11.7	8.47	2.42
f	3	125.9	211.3	15.0	8.92	2.55
g	4	190.5	271.6	13.2	9.26	2.64
h	6	281.8	386.8	13.4	9.75	2.78
i	8	446.7	497.2	11.3	10.11	2.89
j	12	707.9	708.2	10.7	10.65	3.04
k	16	933.3	910.2	10.8	11.04	3.16
l	24	1174.9	1296.6	12.8	11.63	3.32
m	32	1698.2	1666.6	11.8	12.06	3.45
n	45	2238.7	2244.0	12.6	12.60	3.60

Table 5.5 Apparent attenuations for the EW components of station PEN and the estimated values of seismic albedo B_0 's, if we assume a constant Q (=2500) medium

f	$\eta_a = \omega/\beta Q^{-1}$ ($Q = 2500$)	L_a (km) (for $Q=2500$)	\hat{b} (measured)	η_a/\hat{b}	B_0	d_0	L_e (km)
0.5	0.036×10^{-2}	2778	1.00×10^{-2}	0.036	~0.96	0.5	50
1	0.072	1389	1.38	0.052	0.95	0.5	36
2	0.144	694	1.50	0.096	0.90	0.6	40
3	0.215	465	1.60	0.134	0.87	0.6	38
6	0.431	232	2.03	0.212	0.79	0.7	34
12	0.862	116	2.50	0.345	0.66	0.8	31
24	1.72	58	2.73	0.63	0.37	0.95	35
45	3.23	31	3.00	1.08	0	1	33

Table 6.1 The Predicted arrival time of the peak power by the diffusion approximation based on the assumed constant $Q(=2500)$ model and the estimated parameters in Table 5.5.

f (hz)	absorption time τ_a (sec.)	mean free time τ_g (sec.)	$d(1-\bar{\gamma})$ (km ² /sec)	Albedo B_0	L_e	Arrival time of peak power t_m/t_0		
						$\bar{\gamma} = -0.5$	0	0.5
0.5	793.7	14.9	60.8	0.96	50	5.20	4.24	3.0
1	396.8	10.8	44.1	0.95	35	4.62	3.77	2.67
2	198.4	12.7	51.9	0.90	40	3.18	2.60	1.84
3	132.9	12.5	51.0	0.87	38	2.74	2.24	1.58
6	66.3	12.3	50.2	0.79	34	2.06	1.68	1.19

Figure Captions

- 3.1 The derivation of the transfer equation for the specific intensity $I(\underline{r}, \hat{\Omega})$.
- 3.2 The diffuse multipliers d_0 and d_s as functions of B_0 (the medium seismic albedo).
- 3.3 The behavior of the integrand of the integral for the coherent term.
- 3.4 The normalized energy density distribution curves $4\pi r^2 E(r)$, where r is the propagation distance from the point source. At the top are the curves of the diffuse term, at the bottom are that of the coherent term; in the middle are the curves of the sum of the two term. Here D_e is the numerical extinction distance, $L_e = 1/\eta_e$ is the extinction length of the medium, $\eta_e = \eta_s + \eta_a$ is the extinction coefficient, where η_s and η_a are the scattering coefficient and the absorption coefficient respectively. $B_0 = \eta_s/(\eta_s + \eta_a)$ is the medium seismic albedo.
- 3.5 The schematic diagram of a possible multiple scattering path compared with the direct path. The hatched shell of unit thickness will receive the energy $4\pi r^2 E(r)$.
- 3.6 The normalized energy distribution curves $4\pi r^2 E(r)$ in the semi-logarithmic scale.
- 3.7 The energy distribution curves with the numerical absorption distance $D_a = r/L_a$, where $L_a = 1/\eta_a$ is the absorption length of the medium. b is the apparent attenuation coefficient obtained from the slope of the curve. B_0 is the medium albedo.
- 3.8 The energy distribution curves with the numerical scattering distance $D_s = 4/L_s$, where $L_s = 1/\eta_s$ is the scattering length of the medium. B_0 is the medium albedo.

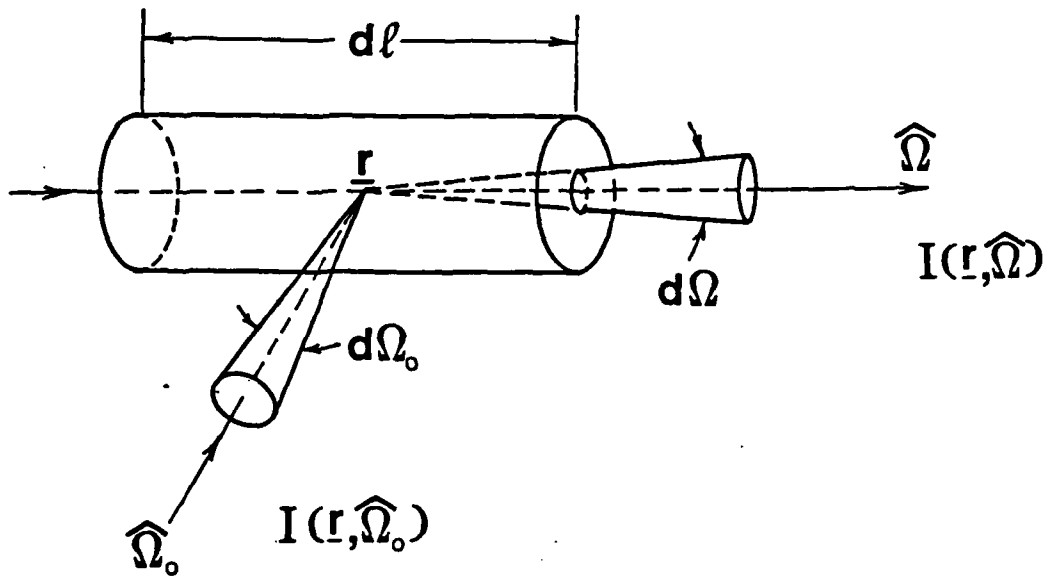
- 3.9 The relative strengths of the diffuse term E_d and the coherent term E_c at different extinction distances $D_e = r/L_e$ for different medium albedo B_0 , where $L_e = 1/\eta_e$ is the extinction length of the medium.
- 3.10 Same as 3.9, at different scattering distances $D_s = r/L_s$, where $L_s = 1/\eta_s$ is the medium scattering length.
- 3.11 The normalized radial energy flux density $4\pi r^2 J_r(r)$ for the isotropic scattering case and the strong forward scattering case.
- 3.12 Same as 3.11. The distance is the numerical absorption distance $D_a = r/L_a$, where $L_a = 1/\eta_a$ is the absorption length of the medium.
- 4.1 The derivation for the case of strong forward scattering approximation. z is along the forward direction. \underline{r} is the position vector, $\underline{\rho}$ is the position vector in the transverse plan; $\hat{\underline{Q}}$ is the unit vector in the scattering direction, and \underline{s} is projection of $\hat{\underline{Q}}$ in the transverse plan.
- 5.1 Map view of seismicity in the Hindu Kush as determined by Chatelain et al. (1980). The digital stations are indicated by open stars, and the smoked paper stations by solid diamonds.
- 5.2 Map view of all the Hindu Kush seismicity on smoked paper stations, divided into 50 km depth intervals. Locations of events recorded on the digital recorders are denoted by numbers used in Table 5.1 (from Roecker 1982).
- 5.3 The overall response of the digital recorder (from Roecker 1981).
- 5.4 The averaged coda attenuation rate $b_c = \beta b$, where β is the shear wave velocity, b is the attenuation coefficient. The solid line is obtained by Roecker (1982) for the shallow events, and the dotted line is the smoothed curve used in this paper.

- 5.5 Some seismograms for different hypocenter distances at station PEN. A42, $r = 11.12$ km, A67, $r = 8.75$ km; A16, $r = 196.42$ km; A02, $r = 310.97$ km.
- 5.6 Energy distribution curves $4\pi r^2 E(r)$ obtained from the data at station PEN. From left to right: Z, EW and NS components. From top to bottom: $f = 0.25-1$ Hz, $f = 1.5-8$ Hz, and $f = 12-45$ Hz.
- 5.7 The predicted $4\pi r^2 E(r)$ curves by the constant Q ($=2000$) model for different frequencies, if the measured apparent attenuation in Kanto, Japan by Aki (1980a) is assumed as the sum of the absorption coefficient and the scattering coefficient (Dainty 1981).
- 5.8 The comparison between the observed $4\pi r^2 E(r)$ for $f = 1.5$ and 2 Hz at station PEN in Hindu Kush and the theoretical predictions for different B_0 's. The curve of $B_0 = 0.9$ is the prediction from the constant Q ($=2500$) model, which does not match with the observation.
- 5.9 Examples of seismograms at station PEN (A34: $r = 104$ km, depth = 4.57 km; A08: $r = 125$ km, depth = 16.27 km), which show strong low frequency components immediately after the direct S).
- 5.10 The energy density curves $4\pi r^2 E(r)$ for direct S waves at $f = 0.25$, 0.5 and 1 Hz for station PEN. The curves are calculated using a 4 sec Hamming window for the direct S arrivals. Compare to fig. 5.6. No arch shape appears here.
- 5.11 Apparent attenuations derived from the slopes of the energy density curves (Fig. 5.6) for station PEN, together with the average coda attenuations and the direct S attenuations.
- O: for EW component, total S
- X: for Z component, total S
- Δ: Z component, direct S (4 sec. window).

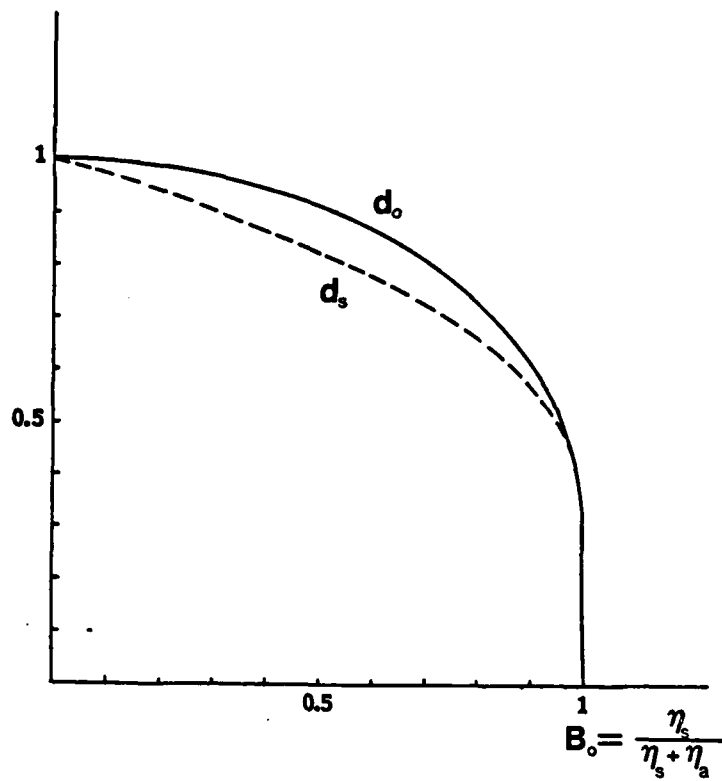
Note: For $f < 1$ Hz, the apparent attenuations are calculated by using only the last part of the curves (Fig. 5.6).

- 5.12 The energy density curves $4\pi r^2 E(r)$ for station CHS. From left to right: Z component and EW component. From top to bottom: $f = 0.25-1$ Hz, $f = 1.5-8$ Hz, and $f = 12-45$ Hz.
- 6.1 The seismogram envelopes of S waves predicted by the diffusion approximation for the case of $f = 2$ Hz, $B_0 = 0.9$ ($Q_1 = 2500$). $\bar{\gamma}$ is the mean scattering angle cosine defined by (6.10).
- 6.2 The seismograms of moonquakes. The event on the top is supposed to be a meteoroid impact; the bottom event is believed to be a deep moonquake (from Latham et al., 1971).
- 6.3 The seismograms from the model experiment in laboratory (Dainty et al., 1974).
- a) The seismogram with the homogeneous plate.
- b) The seismogram when the plate has many grooves as scatterers.
- 6.4 The band-pass filtered seismograms of A06 ($r = 235$ km, depth = 103 km) for the stations CHS, FRA, JOR and PEN. From top to bottom: $f = 0.375$, 0.75, 1.5, 3, 6, 12, 24, 46 Hz.
- 6.5 The band-pass filtered seismograms of A15 ($r = 247$ km, depth = 118 km) for the stations CHS, PEN and JOR. From top to bottom: $f = 0.375$, 0.75, 1.5, 3, 6, 12, 24, 46 Hz.
- 6.6 The envelope decay curves of A15 ($r = 247$ km, depth = 118 km) for station PEN. From left to right: Z component and EW component. From top to bottom: $f = 0.25$, 0.5 Hz; $f = 1-8$ Hz; $f = 12-45$ Hz.

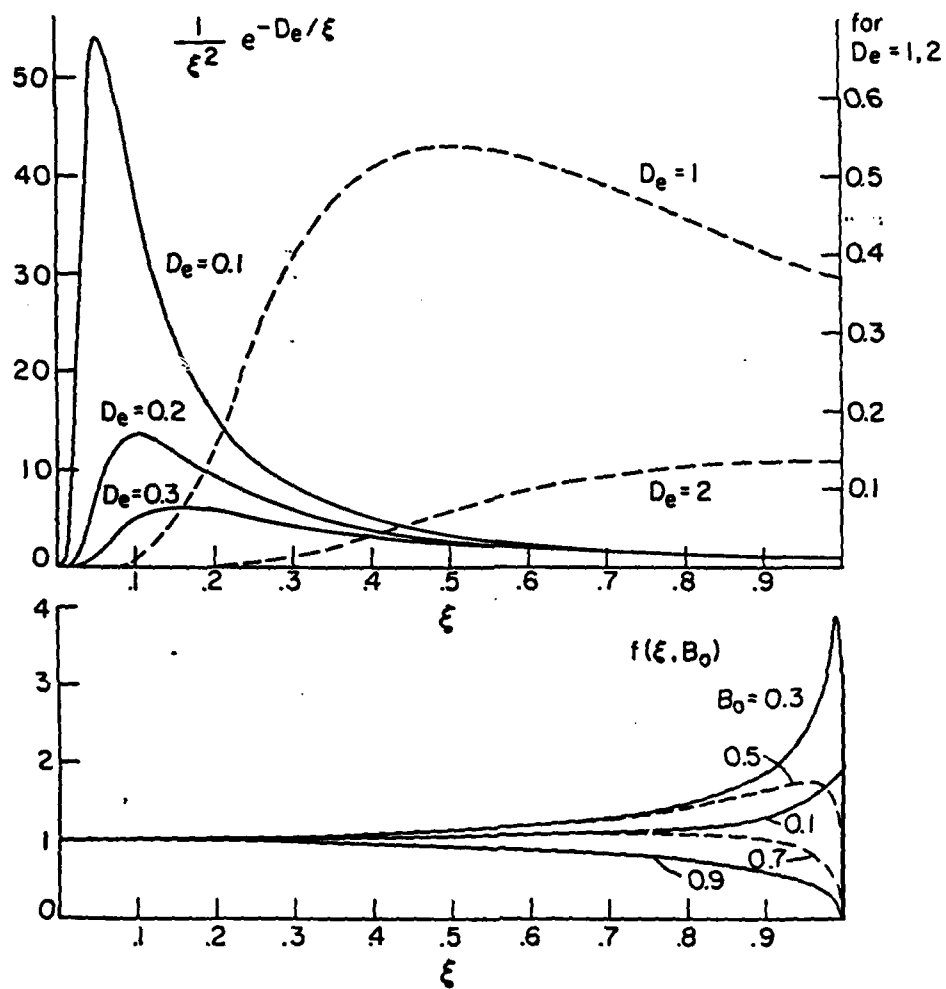
- 6.7 The theoretical envelope decay curve for the single isotropic scattering in a lossless medium according to Sato (1977). The envelope decay is a pure geometric spreading effect. The distance between the source and sensor is taken as 247 km (as the case of A15 to PEN).
- 6.8 The coda decay curves at station PEN for A15 after the geometric correction. The corrections were done by taking the ratios of the curves in Fig. 6.6 and that in Fig. 6.7. Note that, the curves for $f = 1-20$ Hz can be approximately fitted with straight lines, which means that, the scattering at this frequency range can be approximated by the single scattering theory.



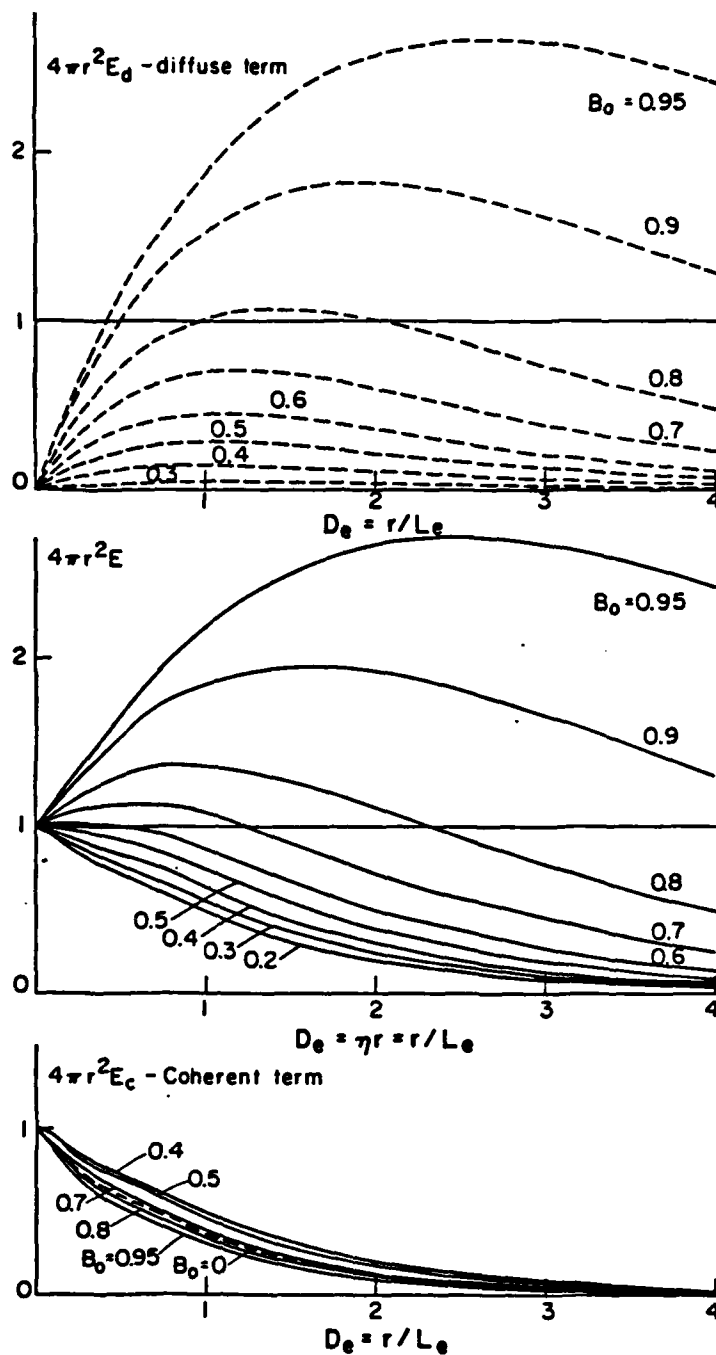
3.1 The derivation of the transfer equation for the specific intensity $I(\underline{r}, \hat{\Omega})$.



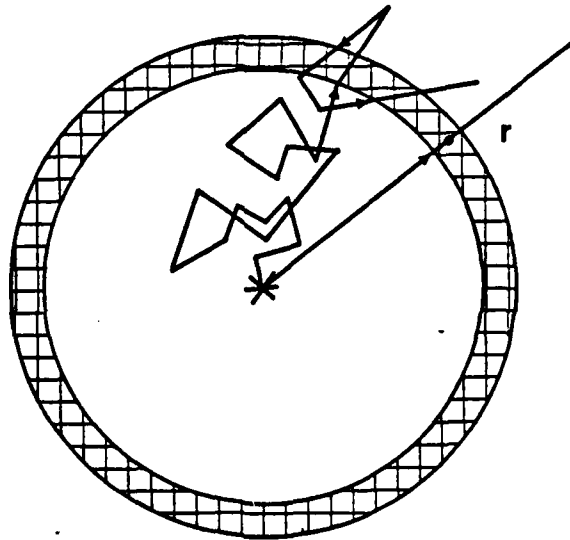
3.2 The diffuse multipliers d_0 and d_s as functions of B_0 (the medium seismic albedo).



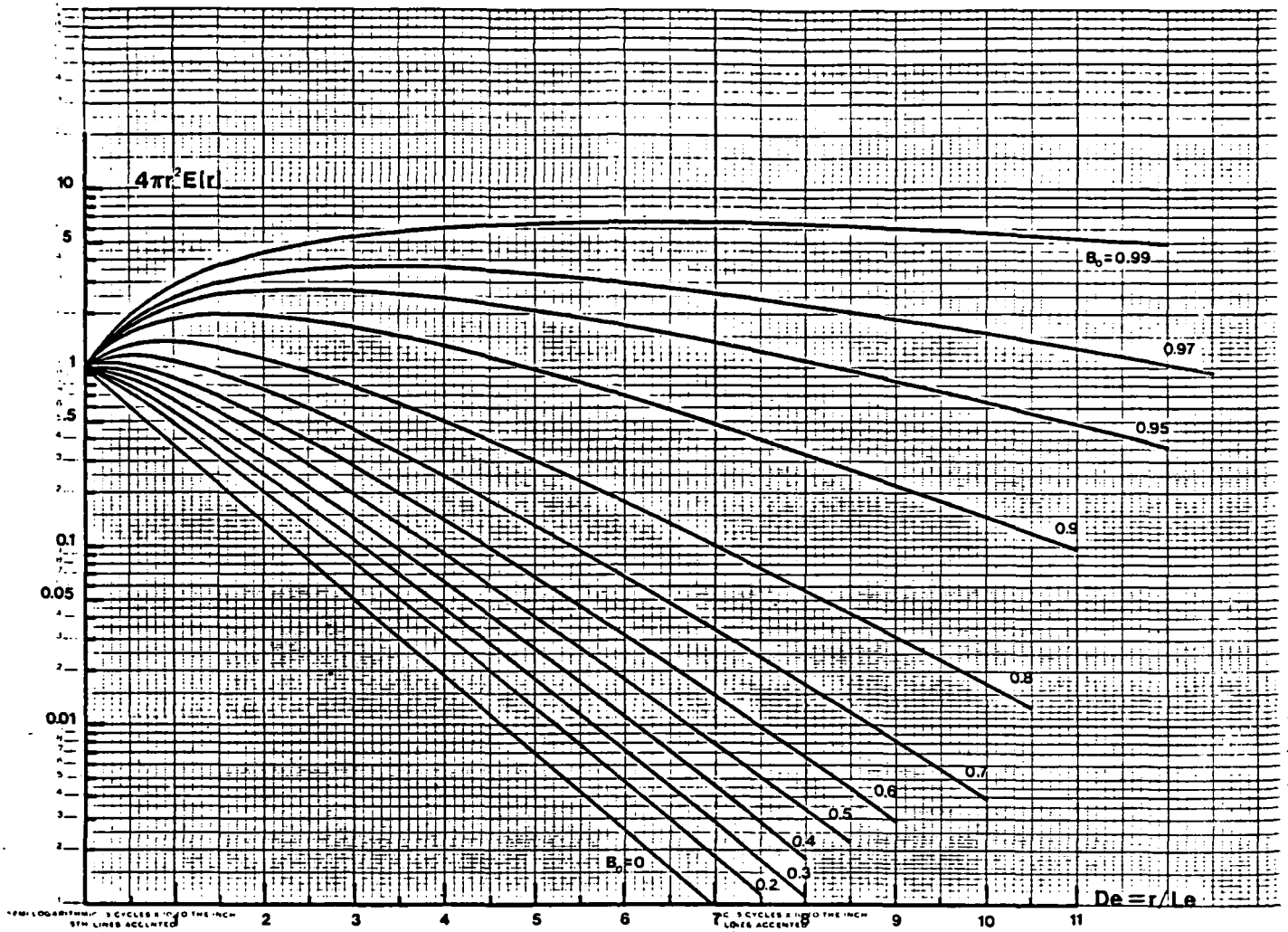
3.3 The behavior of the integrand of the integral for the coherent term.



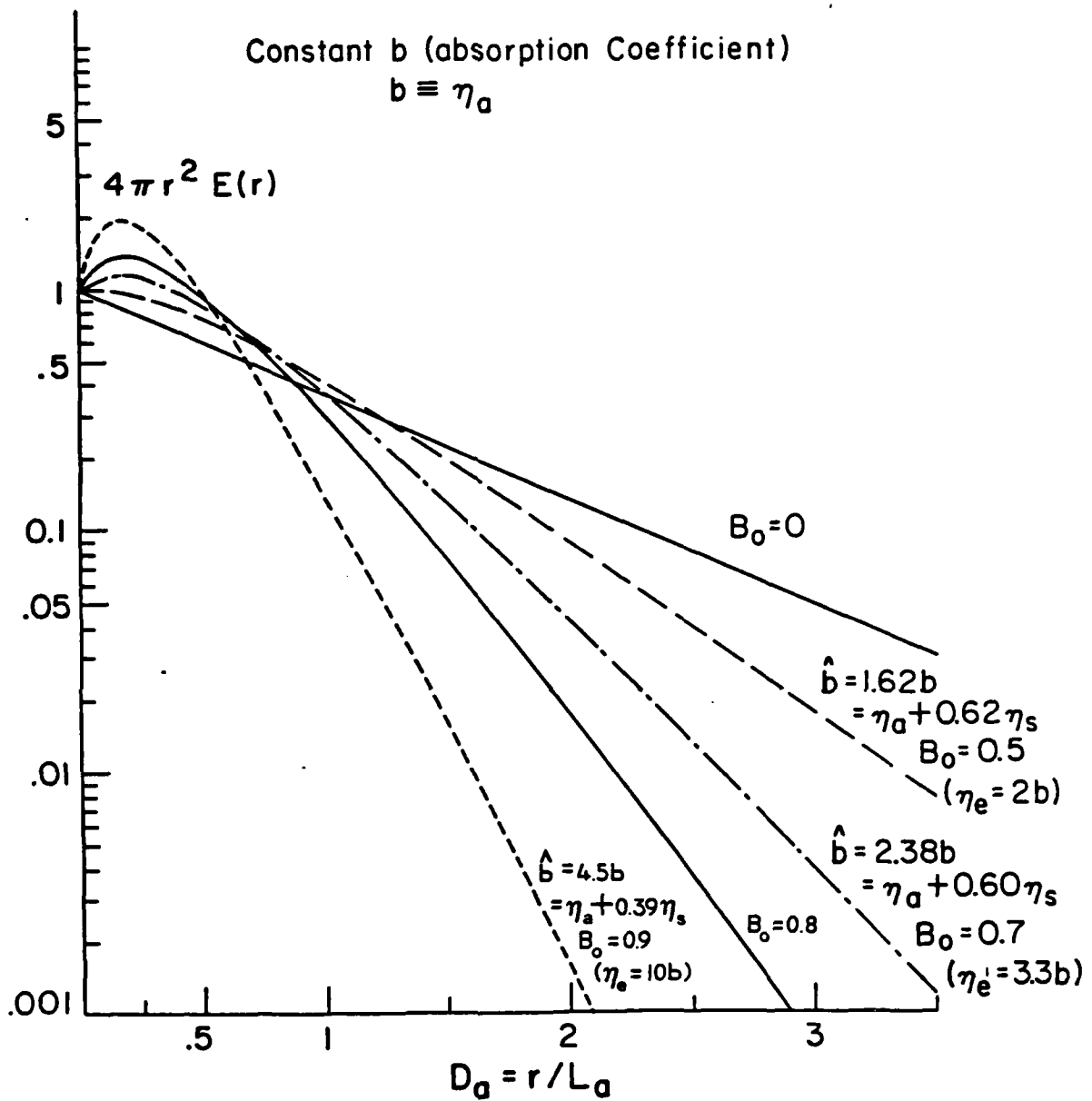
3.4 The normalized energy density distribution curves $4\pi r^2 E(r)$, where r is the propagation distance from the point source. At the top are the curves of the diffuse term, at the bottom are that of the coherent term; in the middle are the curves of the sum of the two term. Here D_e is the numerical extinction distance, $L_e = 1/\eta_e$ is the extinction length of the medium, $\eta_e = \eta_s + \eta_a$ is the extinction coefficient,



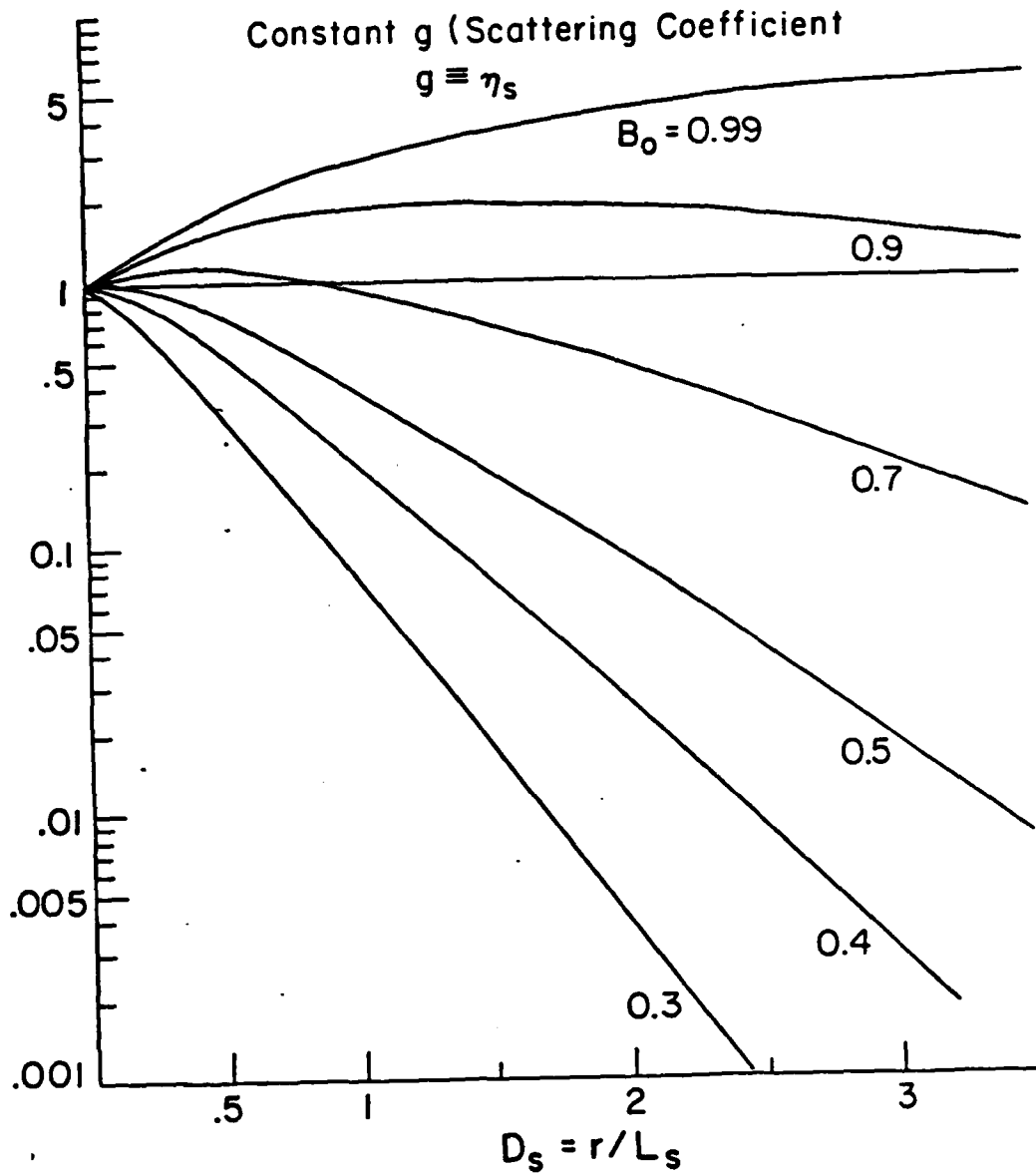
3.5 The schematic diagram of a possible multiple scattering path compared with the direct path. The hatched shell of unit thickness will receive the energy $4\pi r^2 E(r)$.



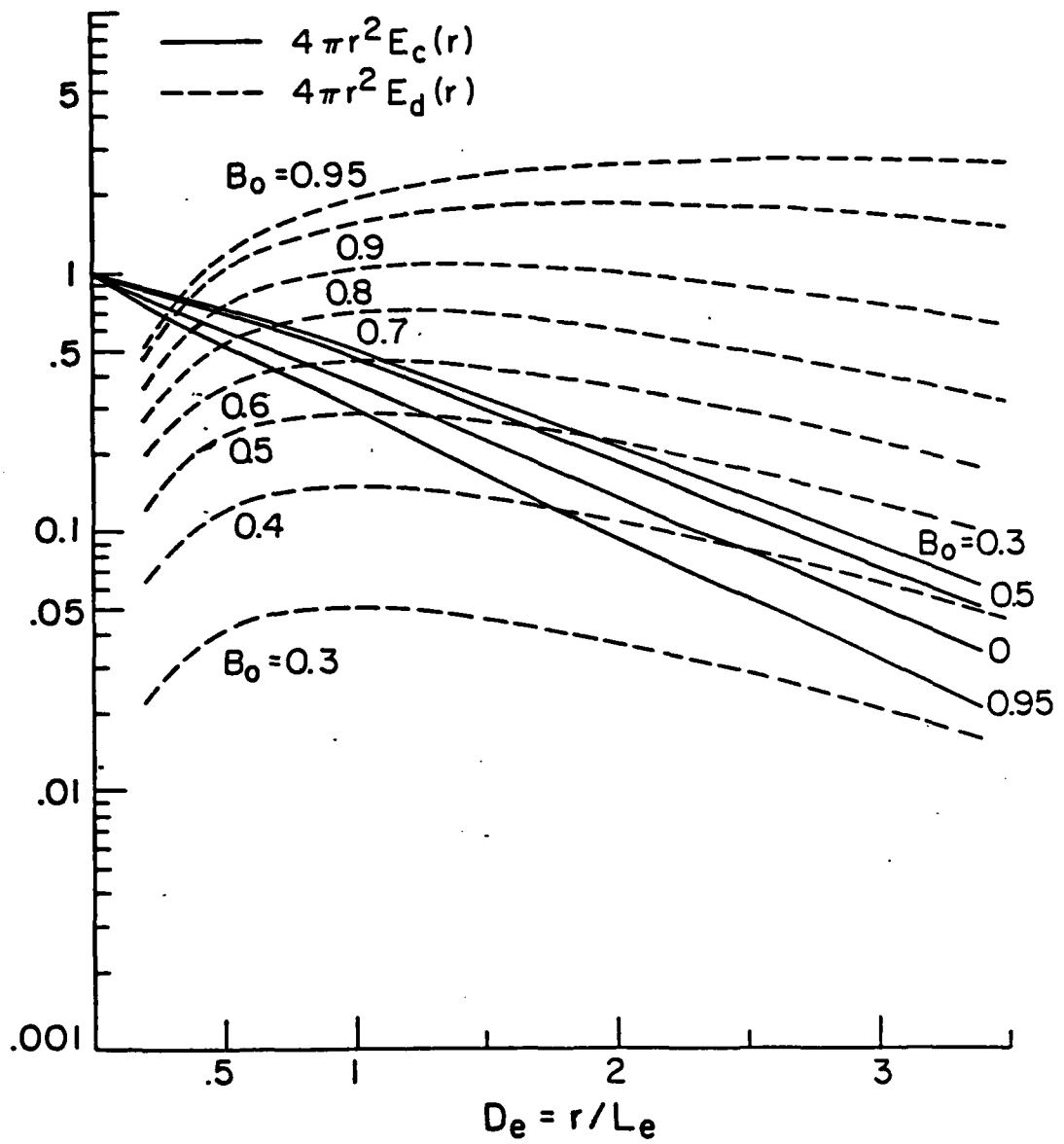
3.6 The normalized energy distribution curves $4\pi r^2 E(4)$ in the semi-logarithmic scale.



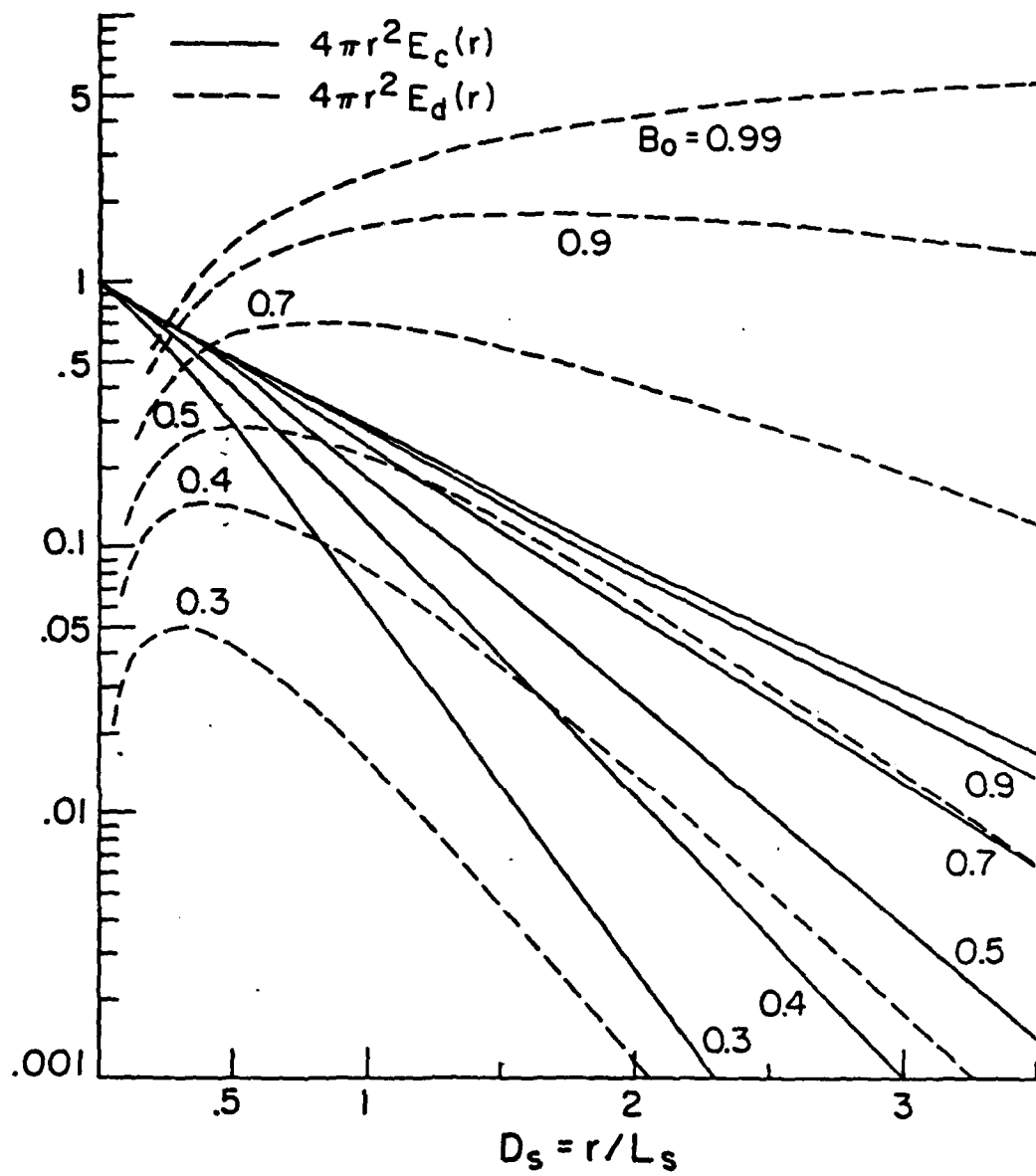
3.7 The energy distribution curves with the numerical absorption distance $D_a = r/L_a$, where $L_a = \eta_a$ is the absorption length of the medium. \hat{b} is the apparent attenuation coefficient obtained from the slope of the curve. B_0 is the medium albedo.



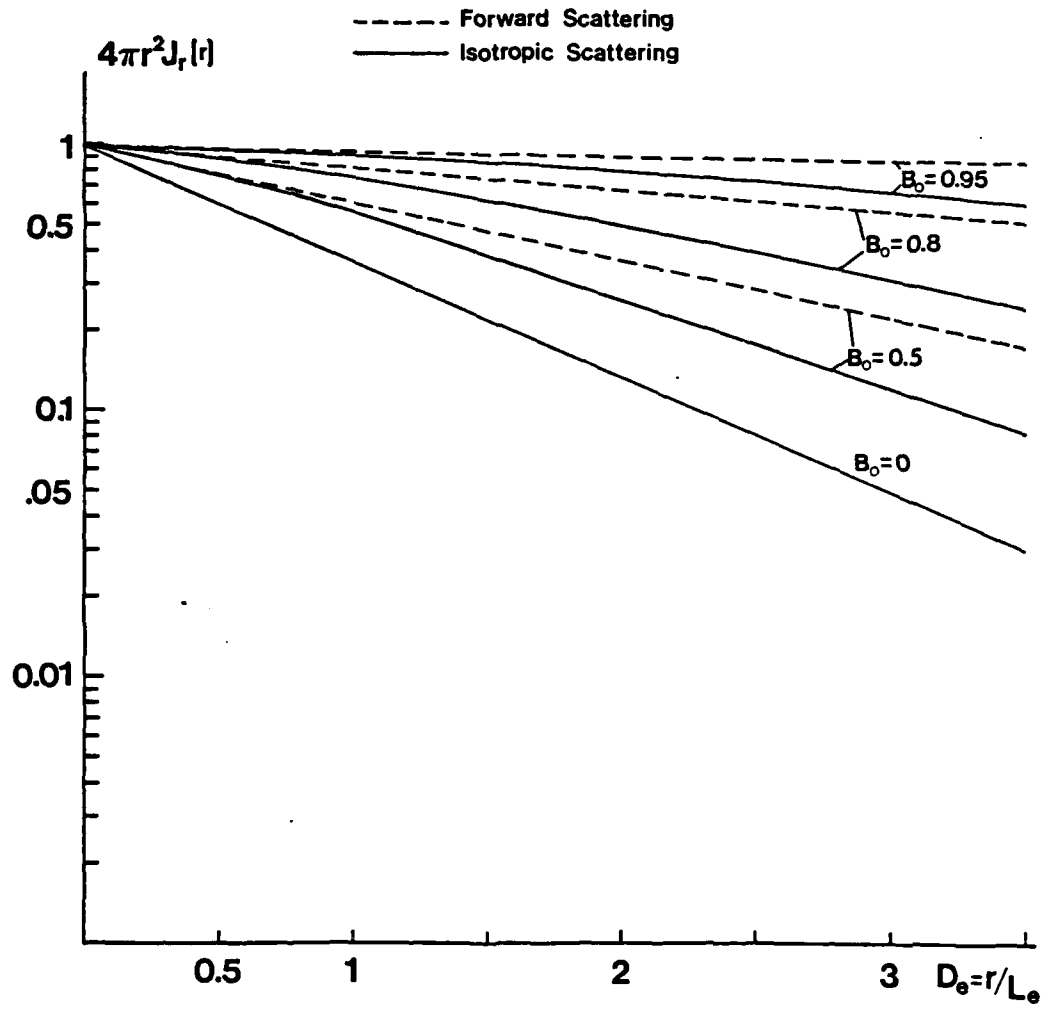
3.8 The energy distribution curves with the numerical scattering distance $D_s = 4/L_s$, where $L_s = 1/\eta_s$ is the scattering length of the medium. B_0 is the medium albedo.



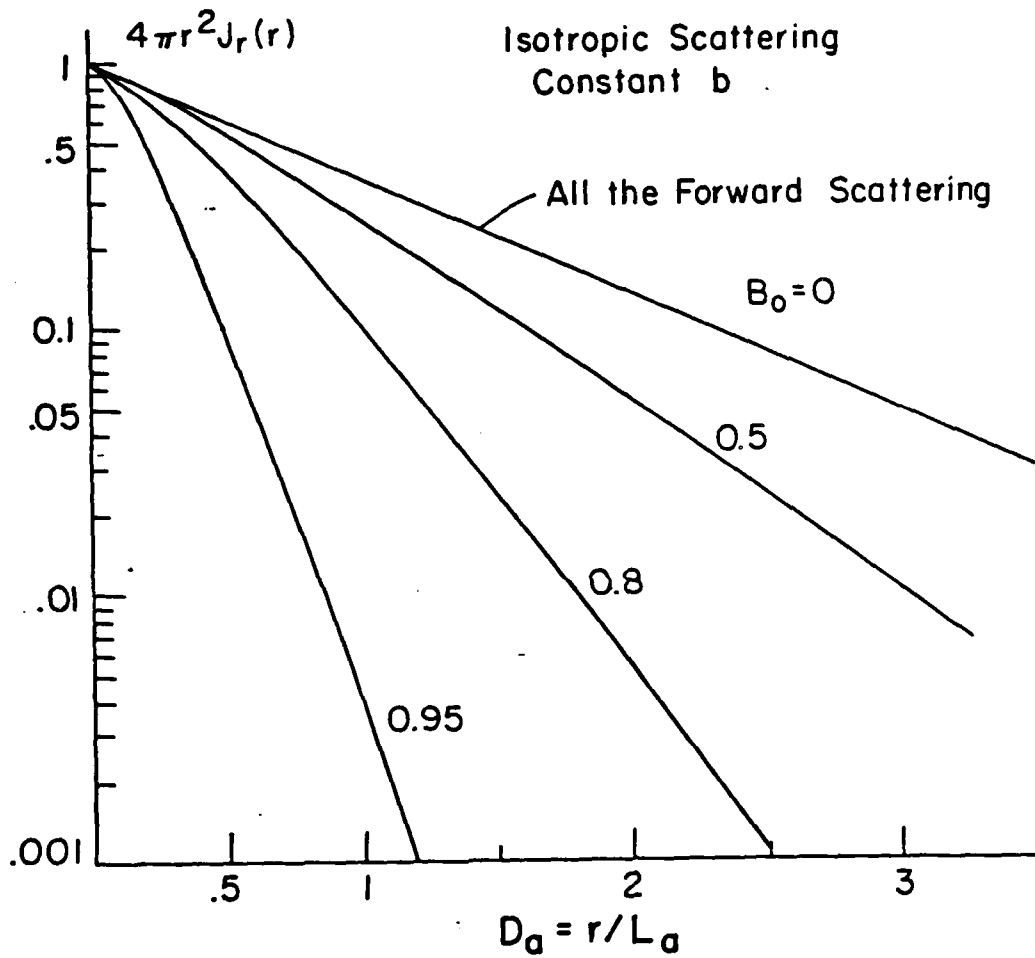
3.9 The relative strengths of the diffuse term E_d and the coherent term E_c at different extinction distances $D_e = r/L_e$ for different medium albedo B_0 , where $L_e = 1/\eta_e$ is the extinction length of the medium.



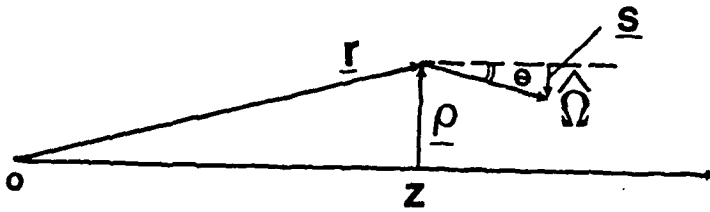
3.10 Same as 3.9, at different scattering distances $D_s = r/L_s$, where $L_s = 1/\eta_s$ is the medium scattering length.



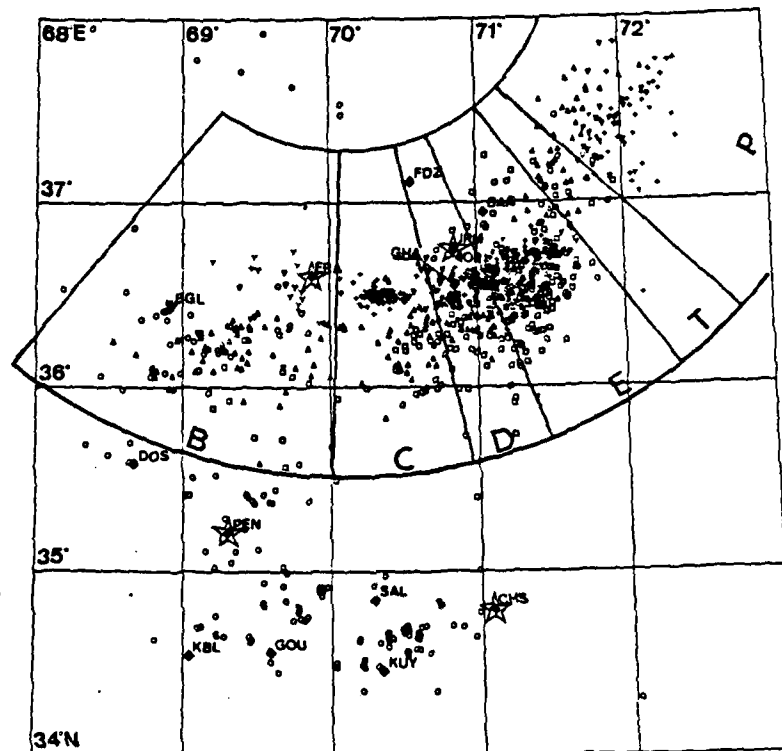
3.11 The normalized radial energy flux density $4\pi r^2 J_r(r)$ for the isotropic scattering case and the strong forward scattering case.



3.12 Same as 3.11. The distance is the numerical absorption distance $D_s = r/L_a$, where $L_a = 1/\eta_a$ is the absorption length of the medium.



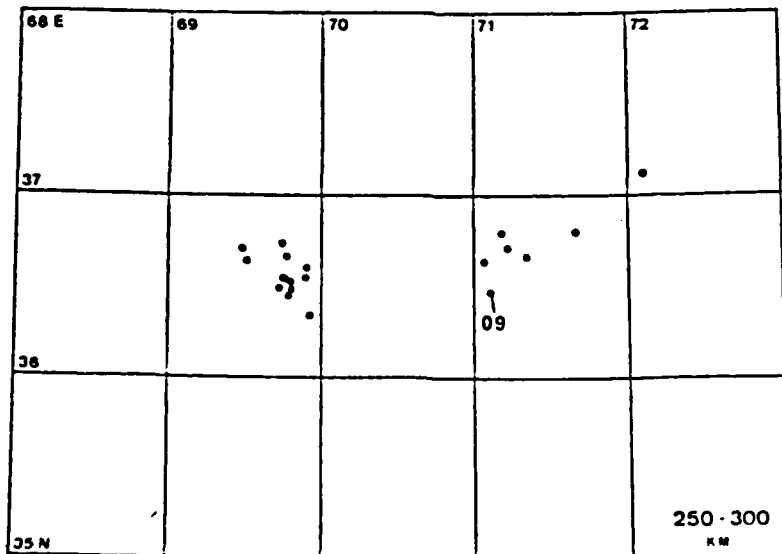
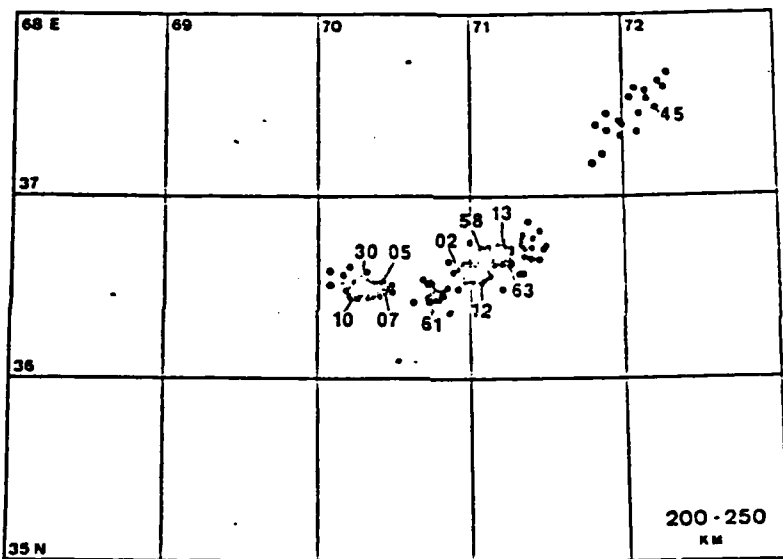
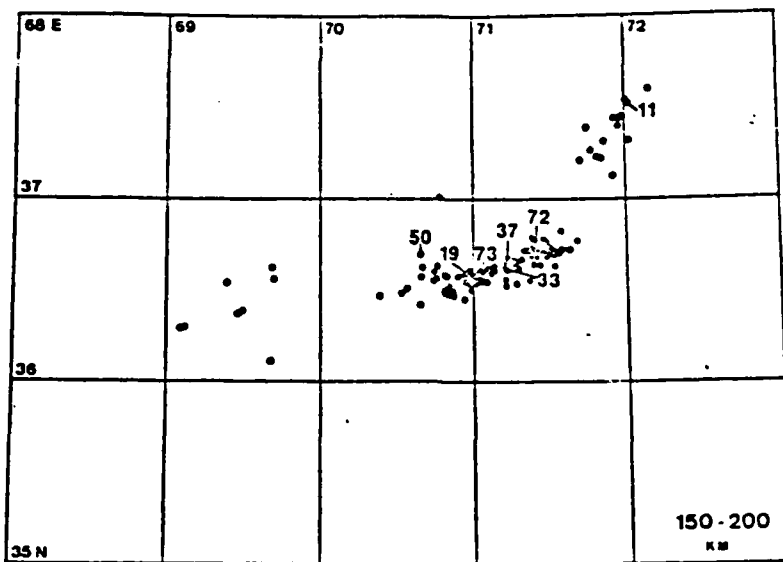
- 4.1 The derivation for the case of strong forward scattering approximation. z is along the forward direction. \underline{r} is the position vector, $\underline{\rho}$ is the position vector in the transverse plan; $\hat{\Omega}$ is the unit vector in the scattering direction, and \underline{s} is projection of $\hat{\Omega}$ in the transverse plan.

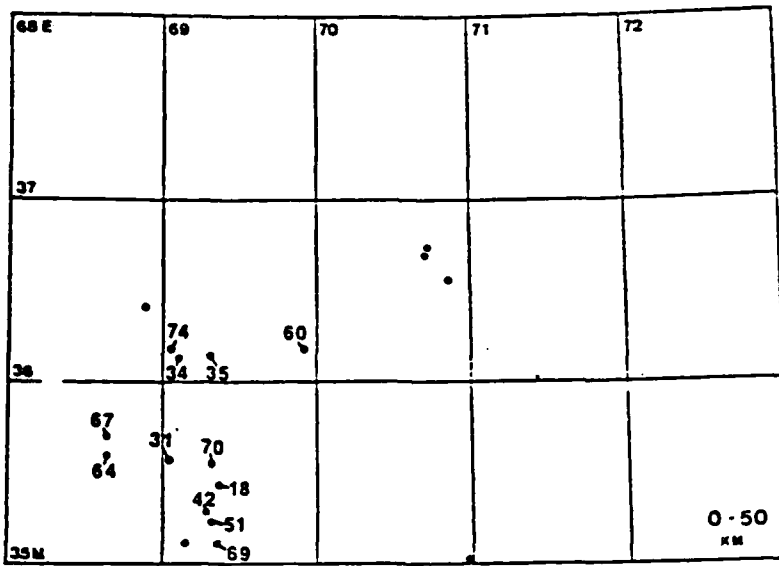


5.1 Map view of seismicity in the Hindu Kush as determined by Chatelain et al. (1980). The digital stations are indicated by open stars, and the smoked paper stations by solid diamonds.

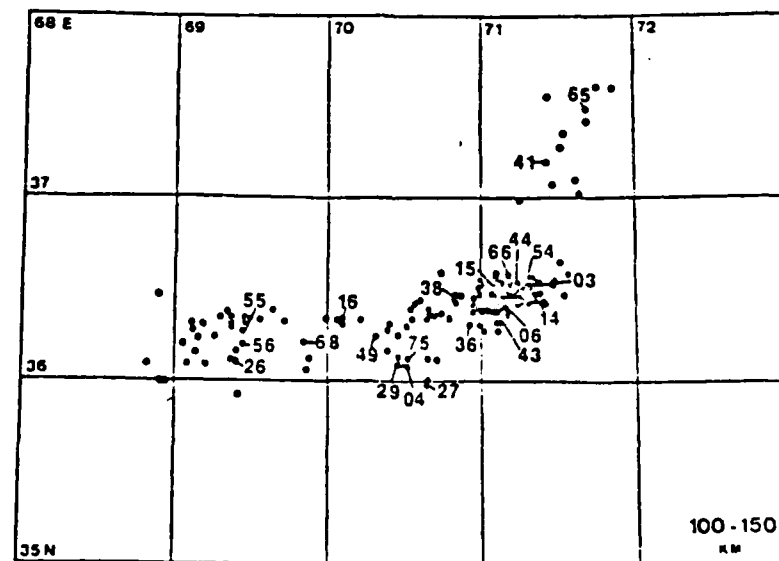
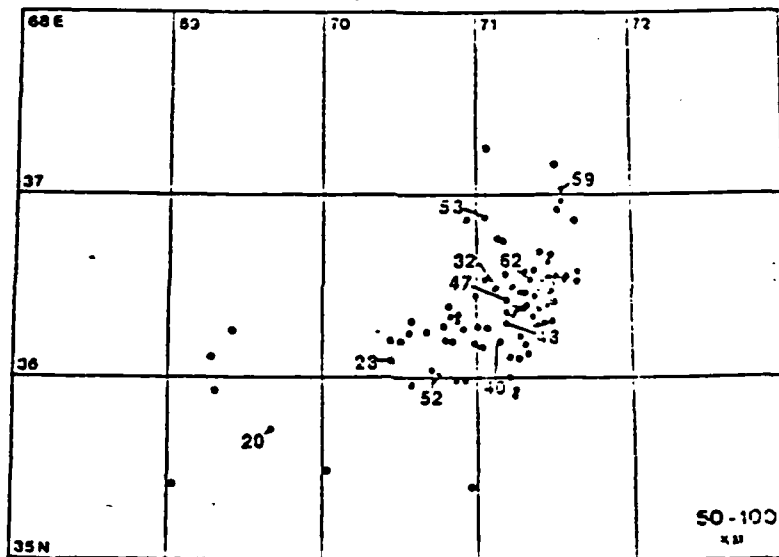
5.2 Map view of all the Hindu Kush seismicity on smoked paper stations, divided into 50 km depth intervals. Locations of events recorded on the digital recorders are denoted by numbers used in Table 5.1 (from Roecker 1982). →

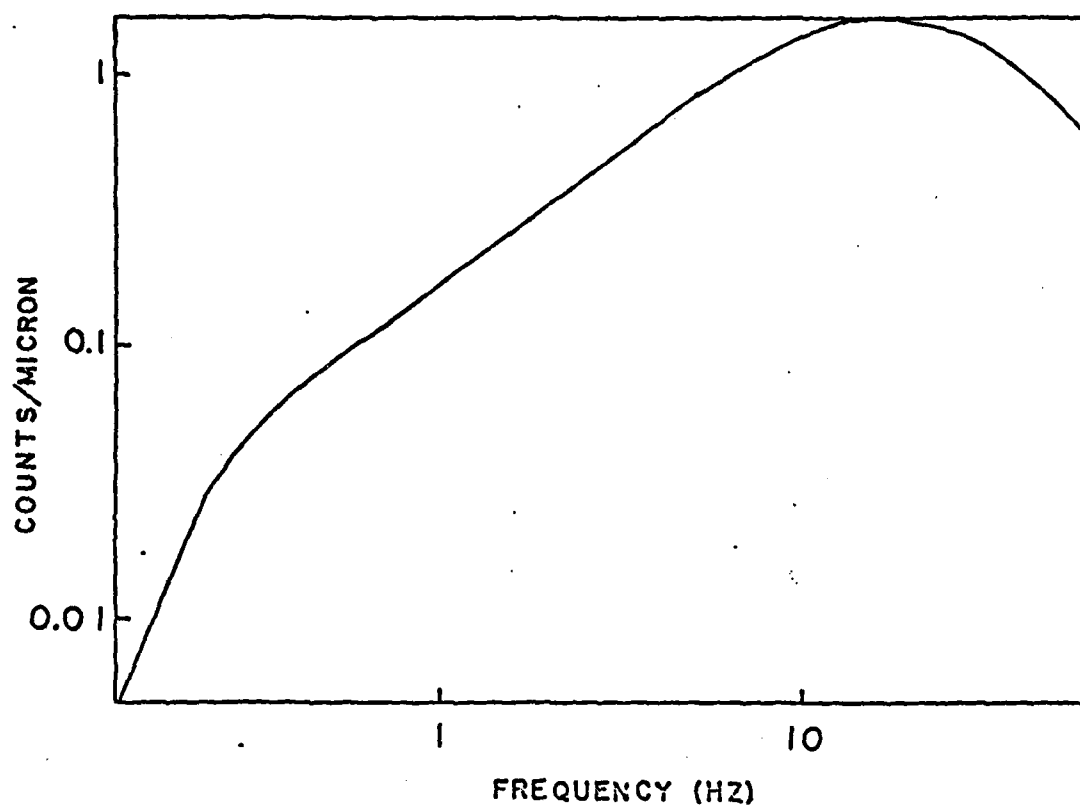
Figure (cont.)



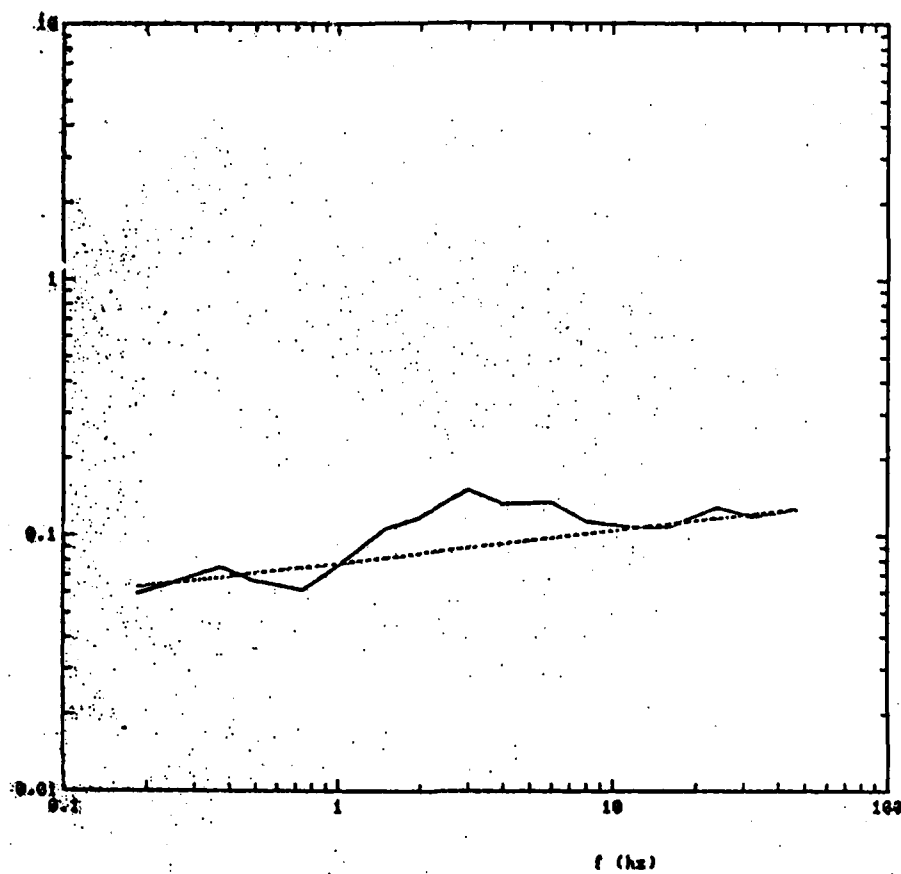


23° 24' 08" 46

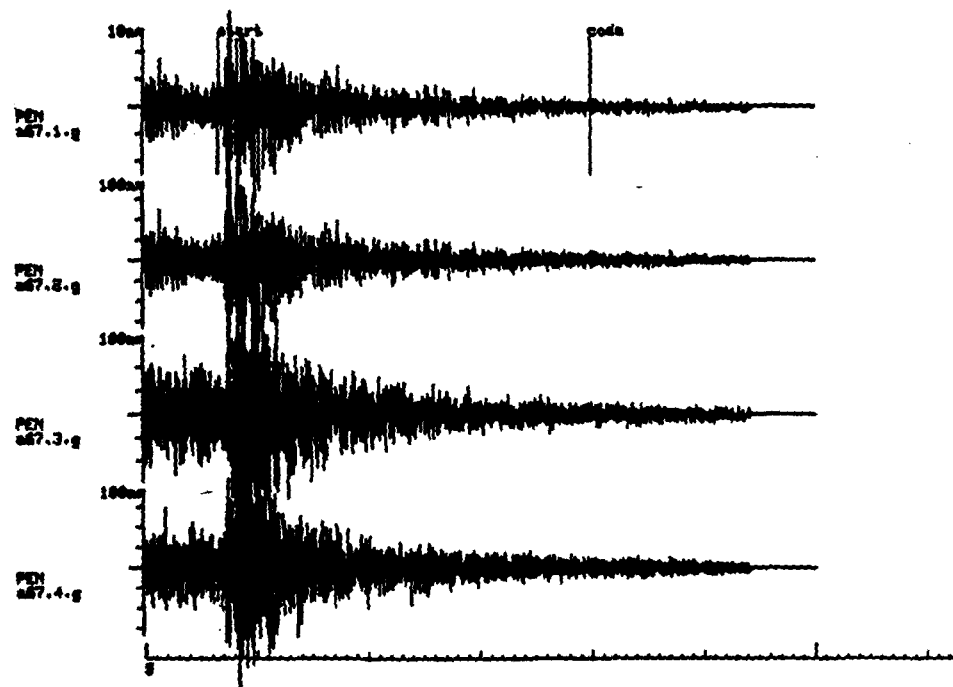
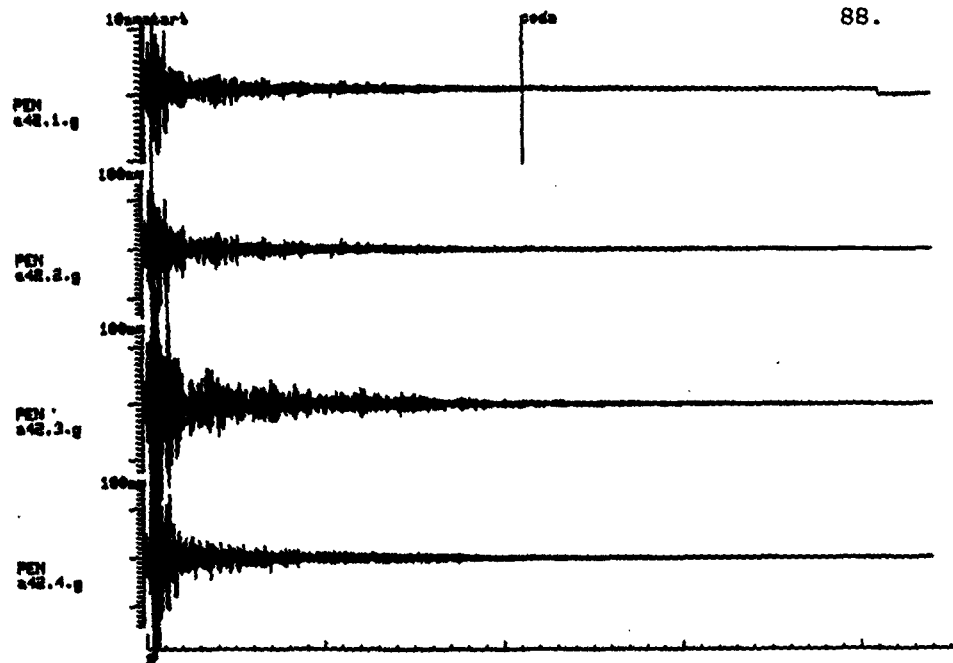




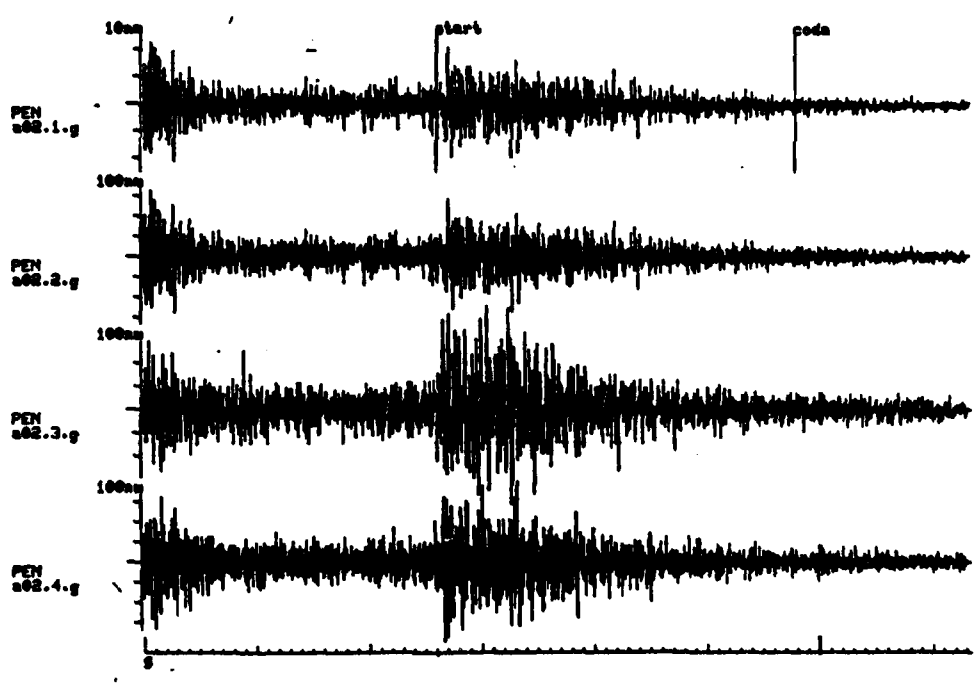
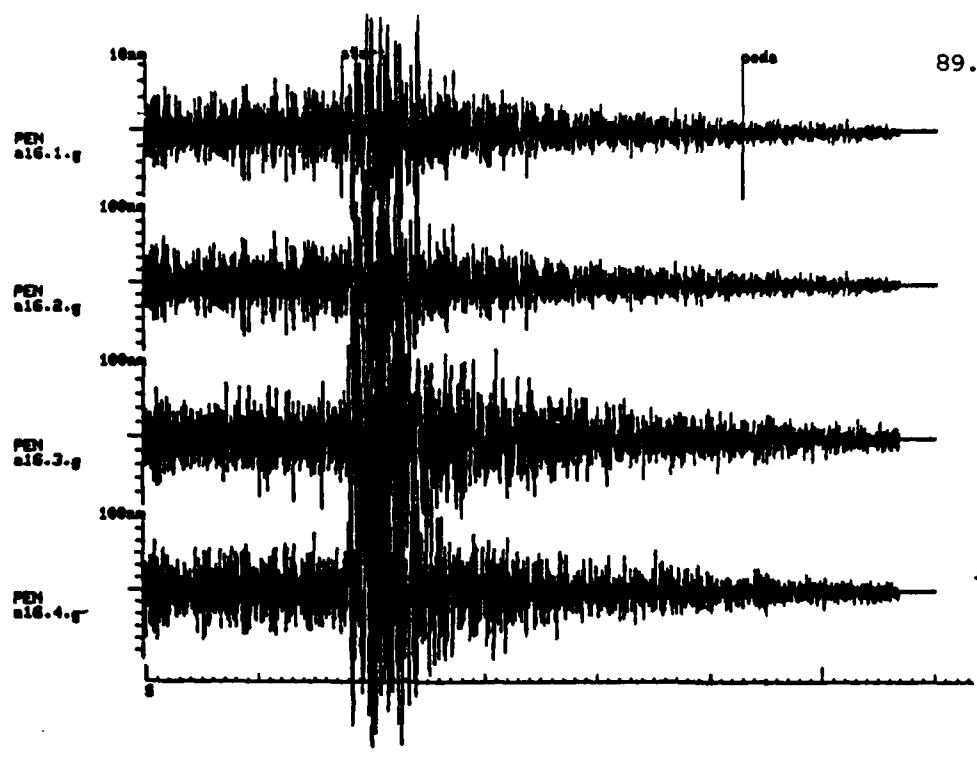
5.3 The overall response of the digital recorder (from Roecker 1981).

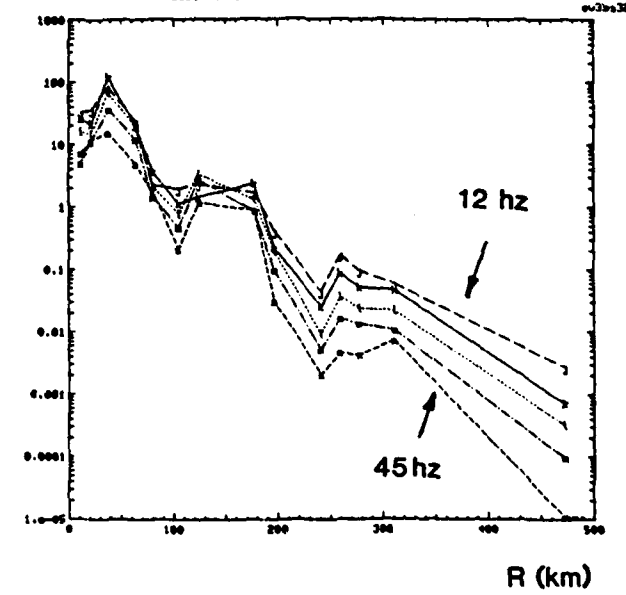
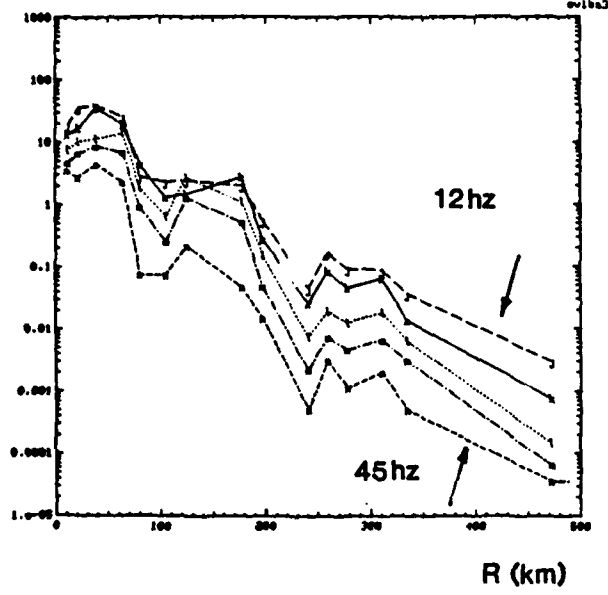
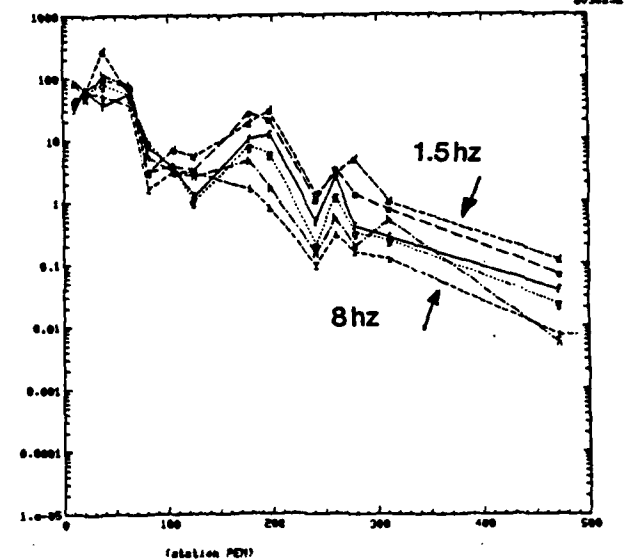
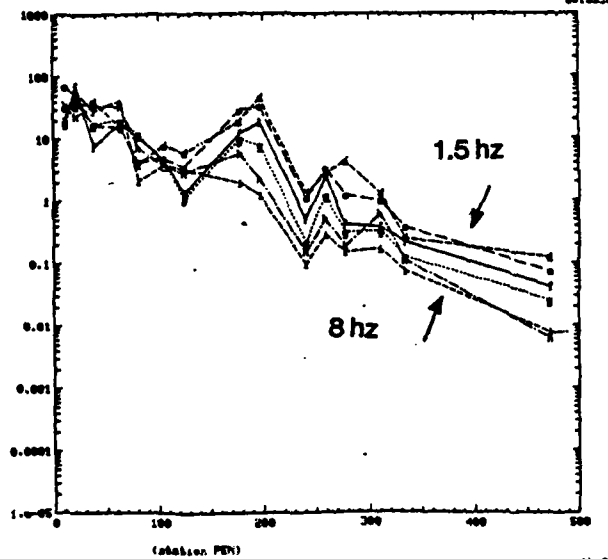
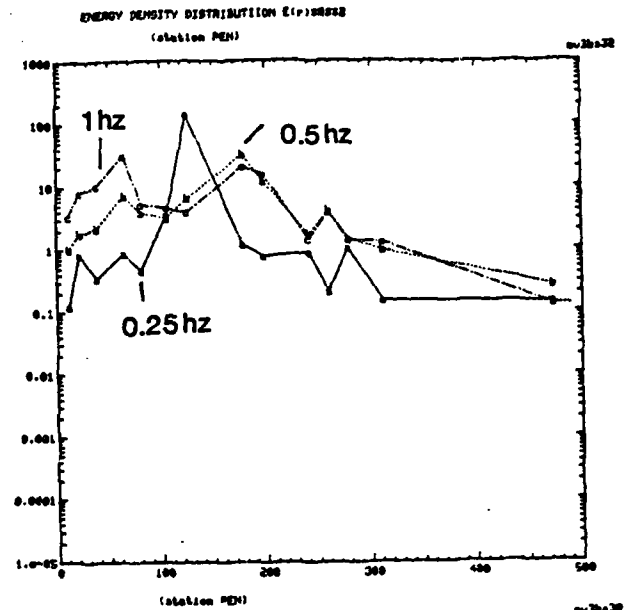
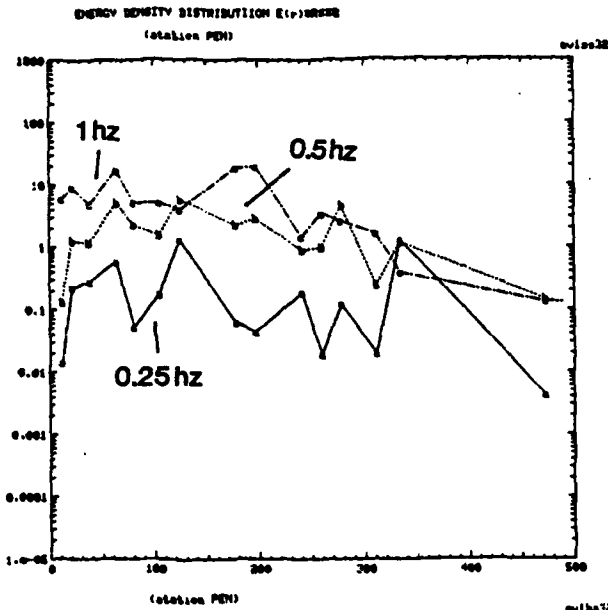
Frequency dependence of the attenuation b_t 

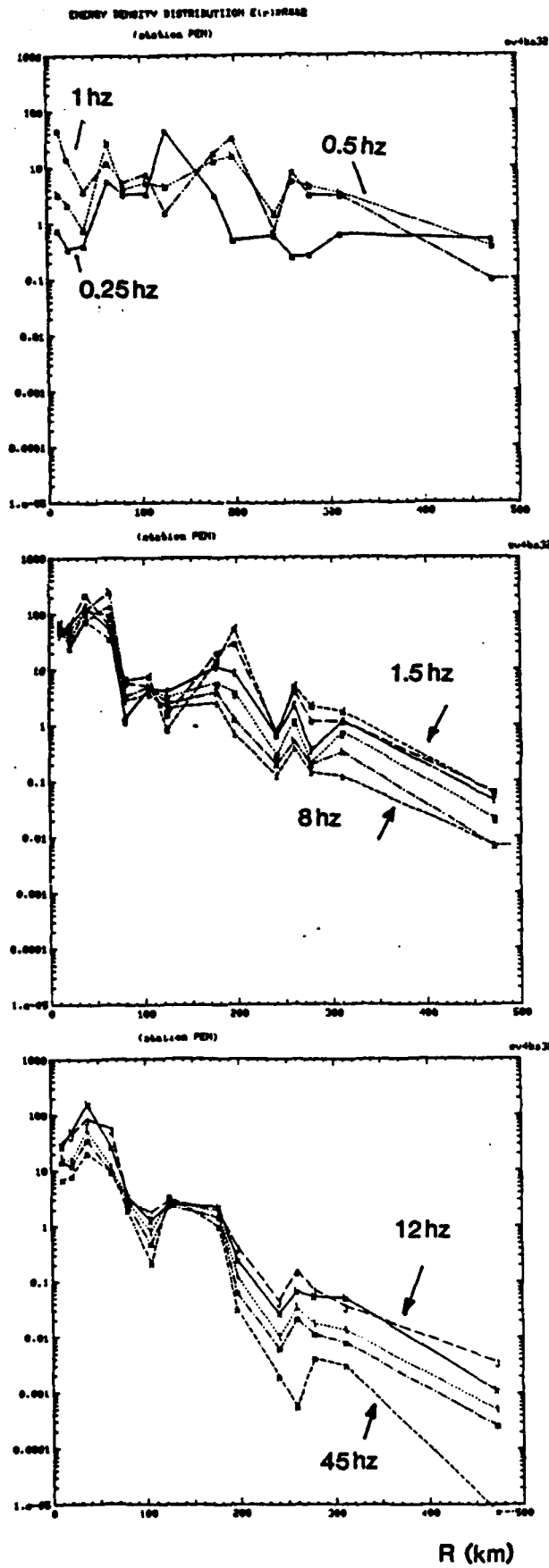
5.4 The averaged coda attenuation rate $b_t = \beta b$, where β is the shear wave velocity, b is the attenuation coefficient. The solid line is obtained by Roecker (1982) for the shallow events, and the dotted line is the smoothed curve used in this paper.



3.5 Some seismograms for different hypocenter distances at station PEN. A42, $r = 11.12$ km, A67, $r = 8.75$ km; A16, $r = 196.42$ km; A02, $r = 310.97$ km.







5.6 Energy distribution curves

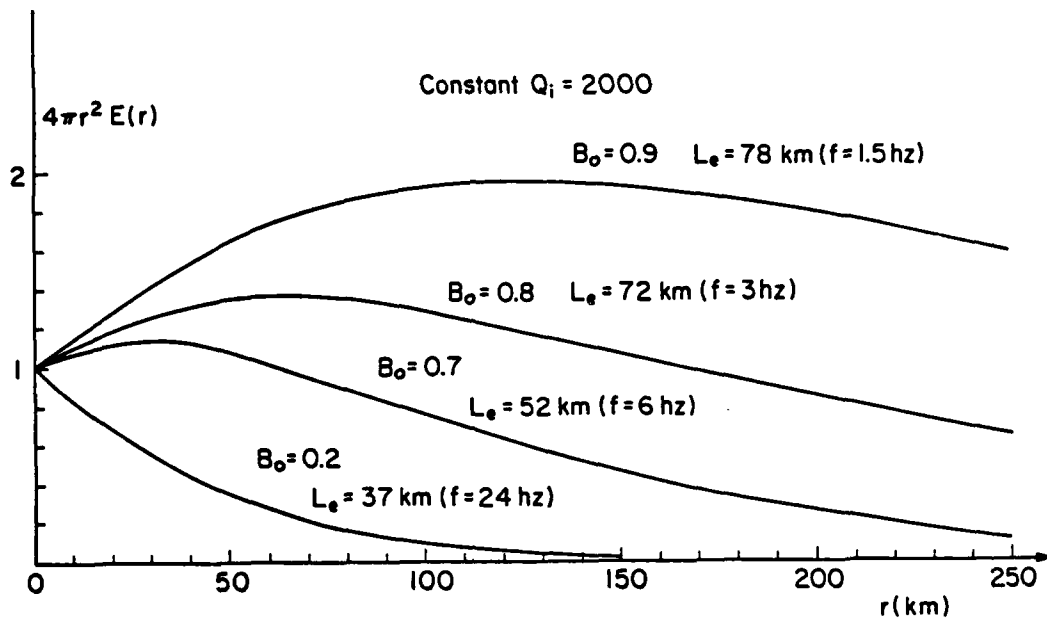
$4\pi r^2 E(r)$ obtained from
the data at station PEN.

From left to right:

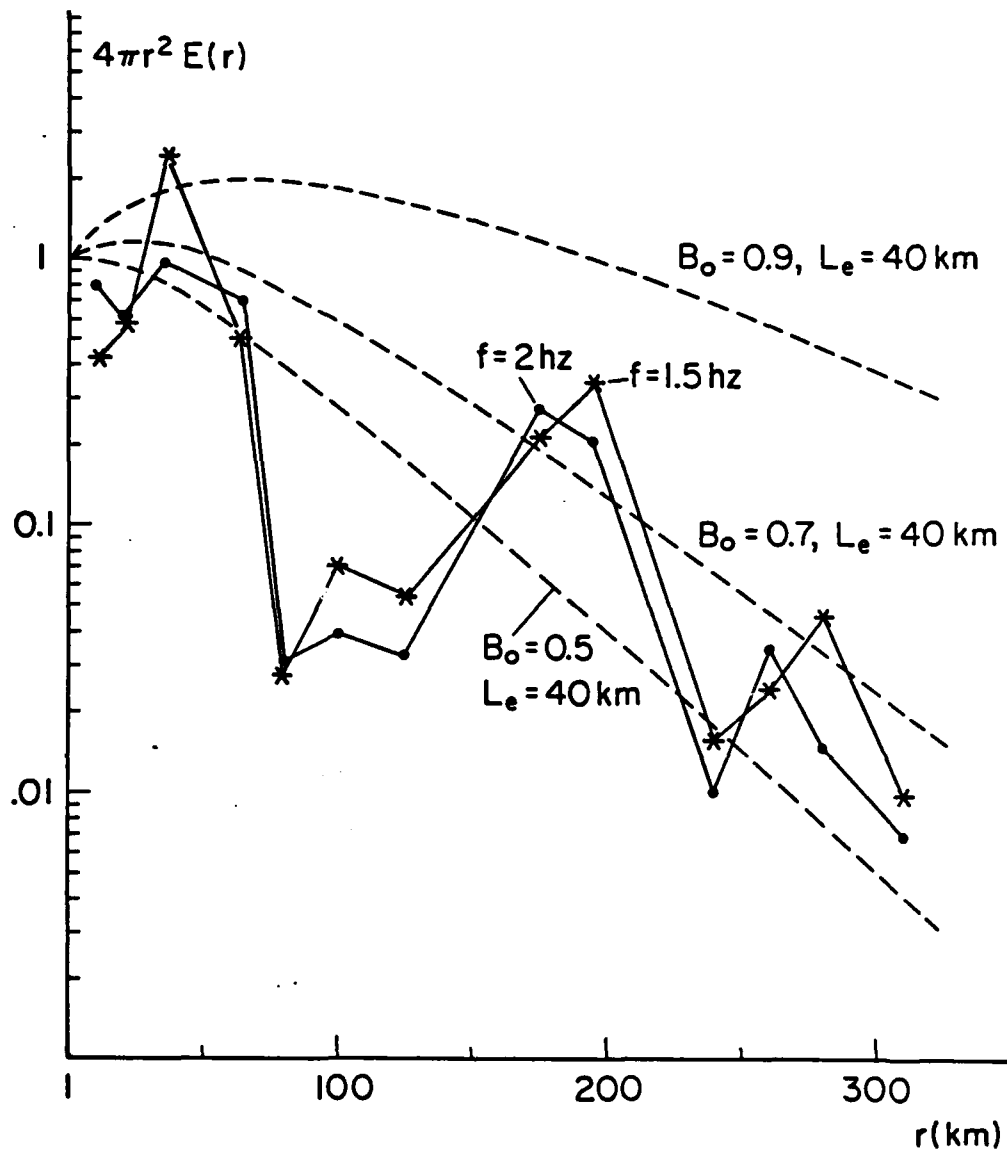
Z, EW and NS components.

From top to bottom:

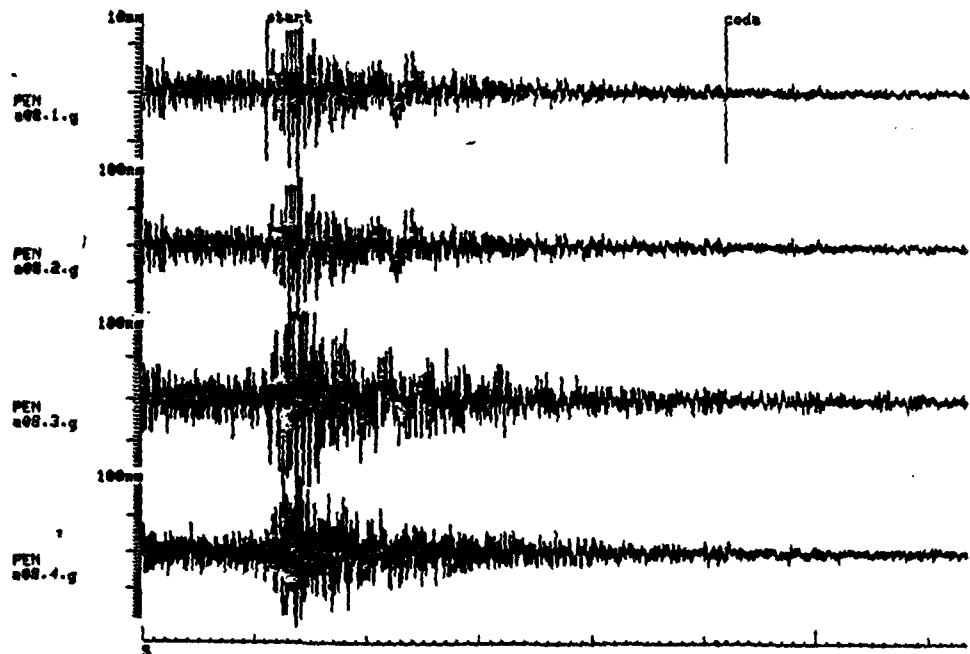
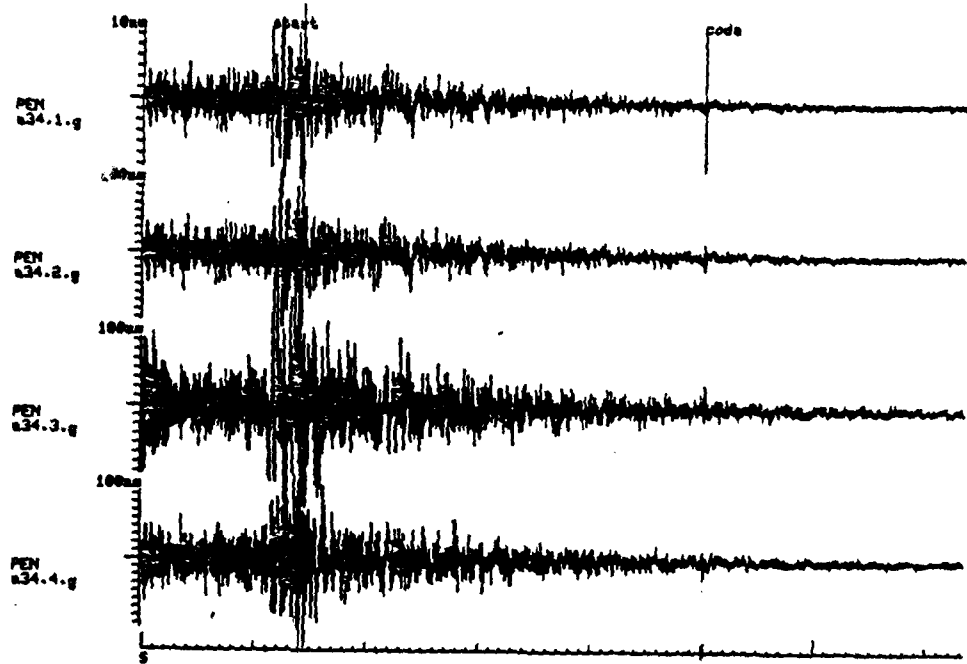
$f = 0.25-1$ Hz, $f = 1.5-8$ Hz,
and $f = 12-45$ Hz.



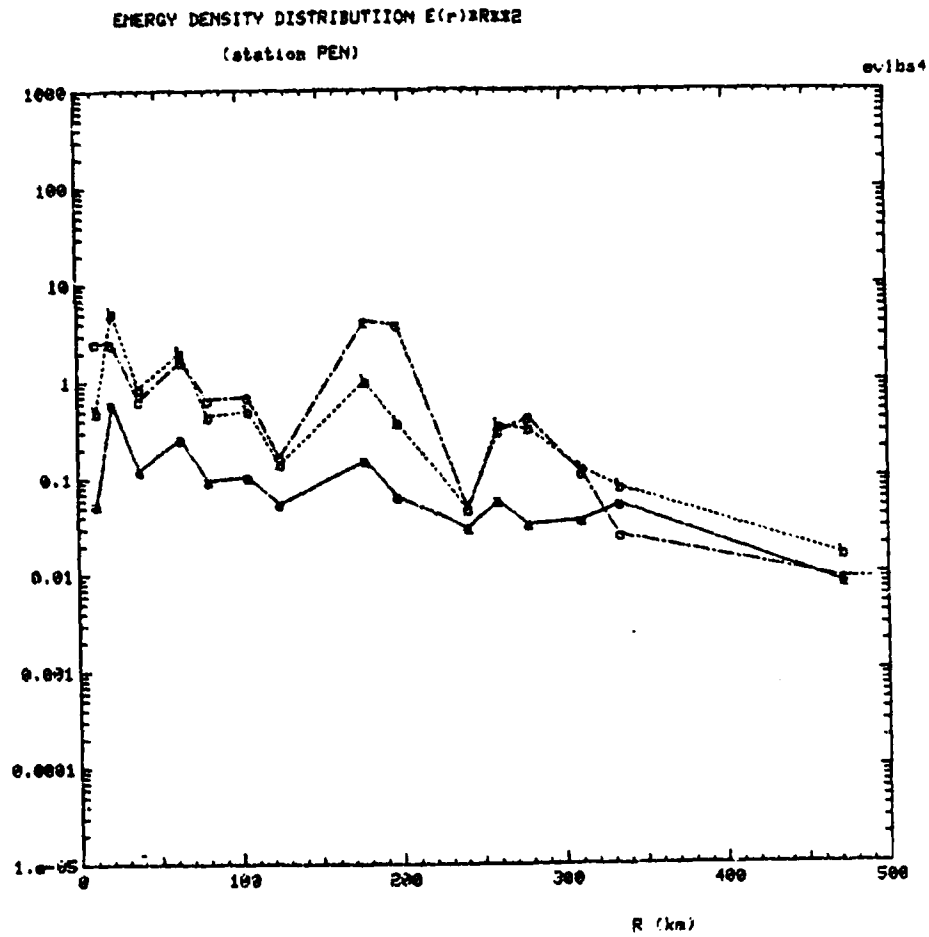
- 5.7 The predicted $4\pi r^2 E(r)$ curves by the constant Q ($=2000$) model for different frequencies, if the measured apparent attenuation in Kanto, Japan by Aki (1980a) is assumed as the sum of the absorption coefficient and the scattering coefficient (Dainty 1981).



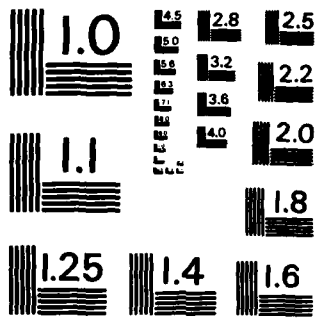
5.8 The comparison between the observed $4\pi r^2 E(r)$ for $f = 1.5$ and 2 Hz at station PEN in Hindu Kush and the theoretical predictions for different B_0 's. The curve of $B_0 = 0.9$ is the prediction from the constant Q ($=2500$) model, which does not match with the observation.



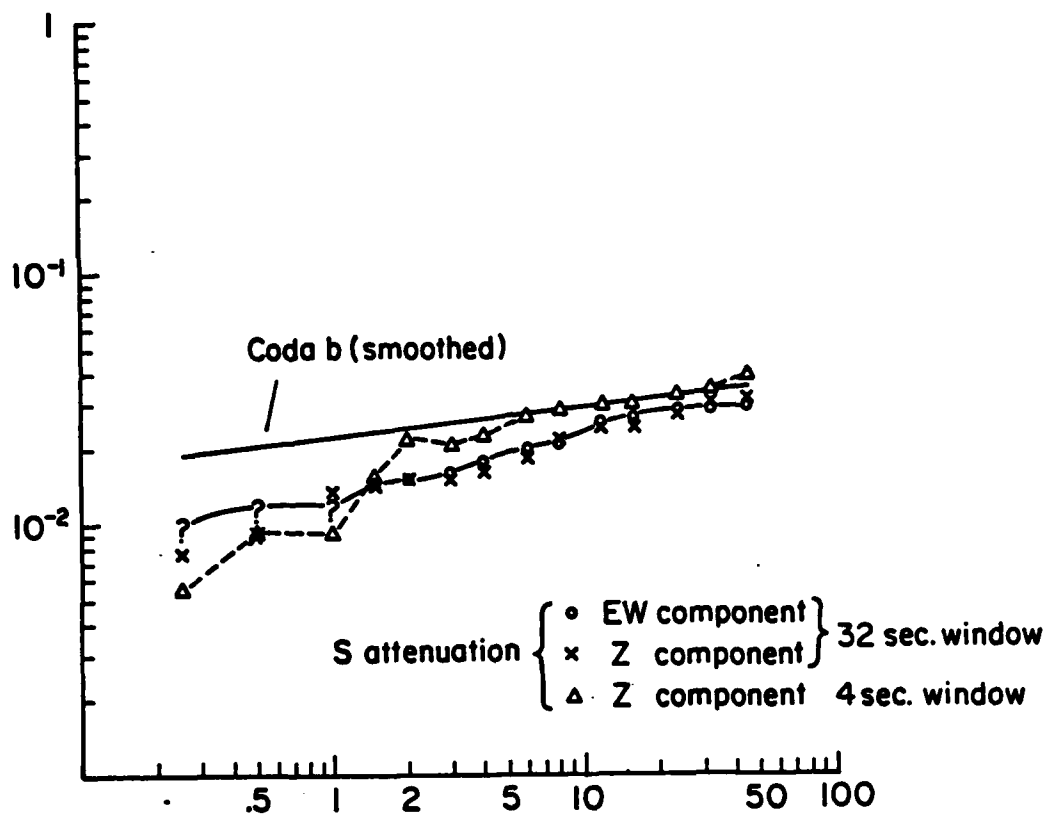
5.9 Examples of seismograms at station PEN (A34: $r = 104$ km, depth = 4.57 km; A08: $r = 125$ km, depth = 16.27 km), which show strong low frequency components immediately after the direct S).



5.10 The energy density curves $4\pi r^2 E(r)$ for direct S waves at $f = 0.25, 0.5$ and 1 Hz for station PEN. The curves are calculated using a 4 sec Hamming window for the direct S arrivals. Compare to fig. 5.6. No arch shape appears here.



MICROCOPY RESOLUTION TEST CHART
NATIONAL BUREAU OF STANDARDS-1963-A



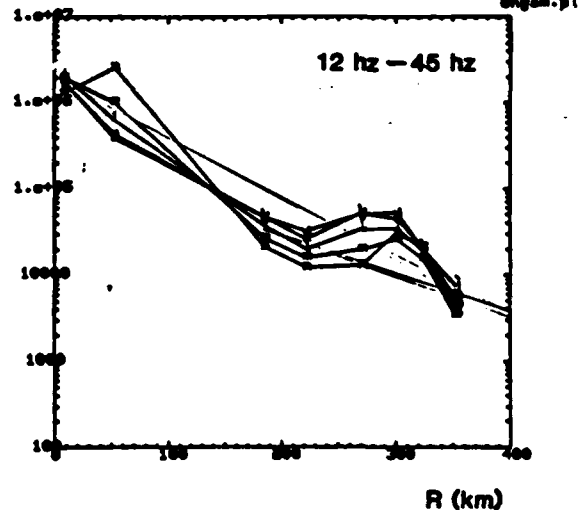
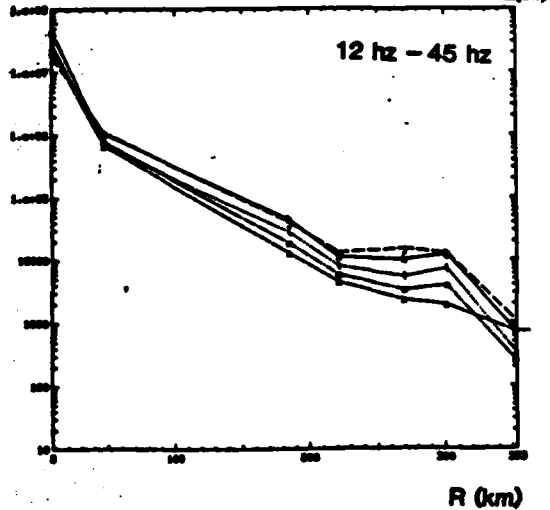
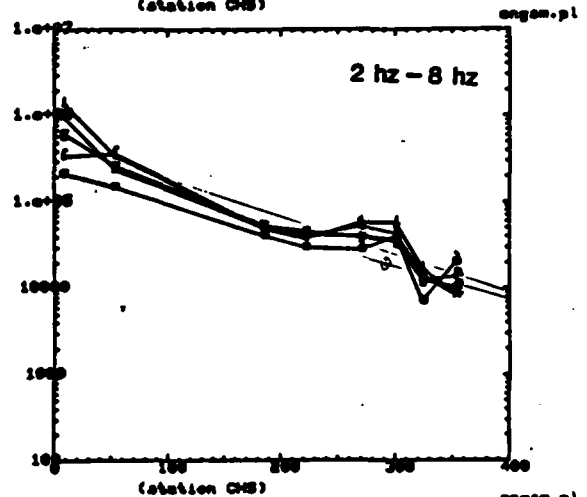
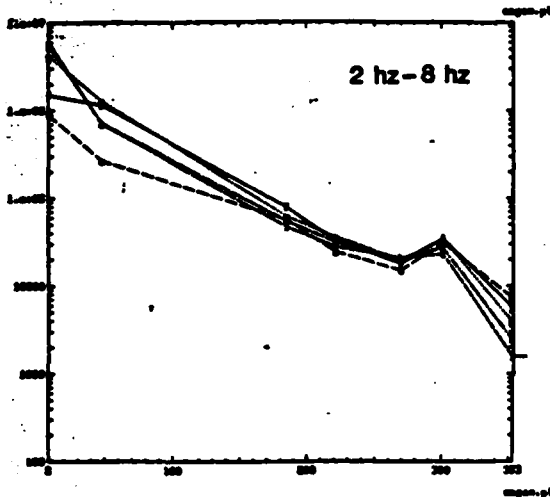
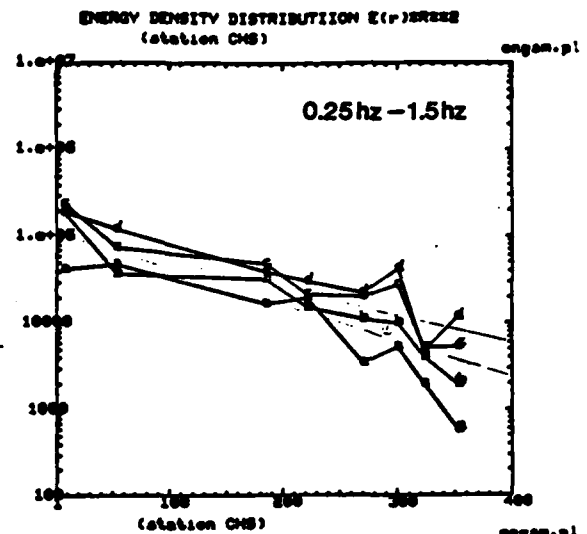
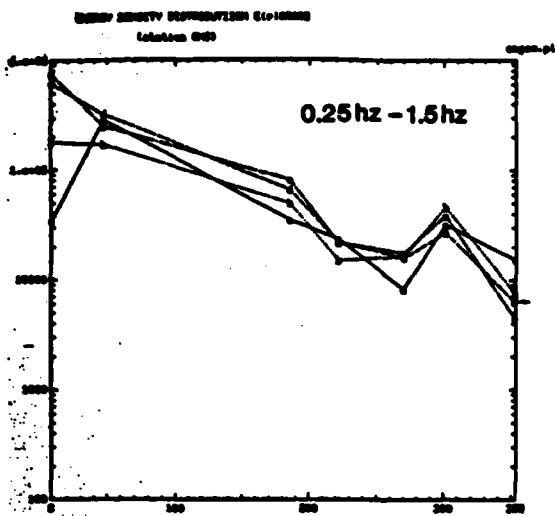
5.11 Apparent attenuations derived from the slopes of the energy density curves (Fig. 5.6) for station PEN, together with the average coda attenuations and the direct S attenuations.

O: for EW component, total S

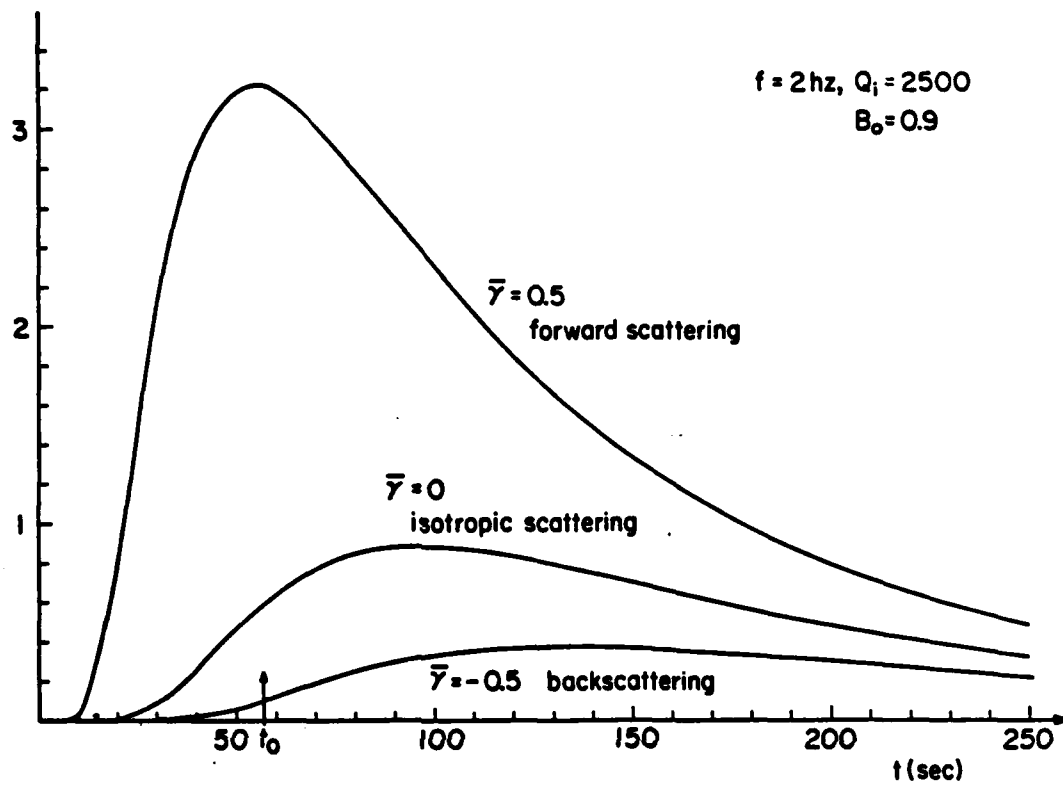
X: for Z component, total S

Δ : Z component, direct S (4 sec. window).

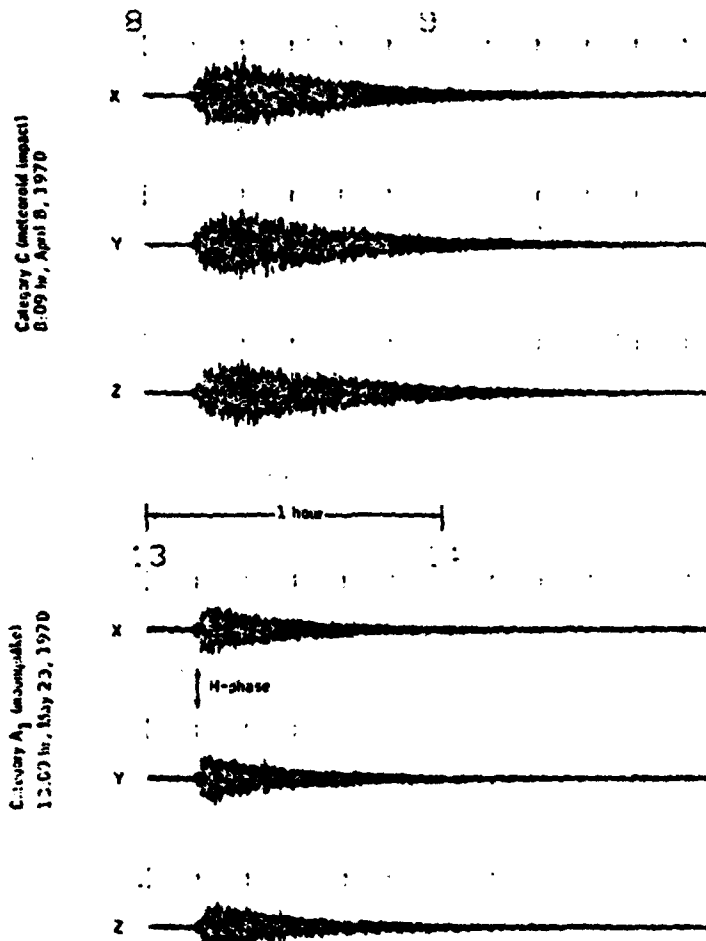
Note: For $f < 1$ Hz, the apparent attenuations are calculated by using only the last part of the curves (Fig. 5.6).



5.12 The energy density curves $4\pi r^2 E(r)$ for station CHS. From left to right: Z component and EW component. From top to bottom: $f = 0.25-1$ Hz, $f = 1.5-8$ Hz, and $f = 12-45$ Hz.

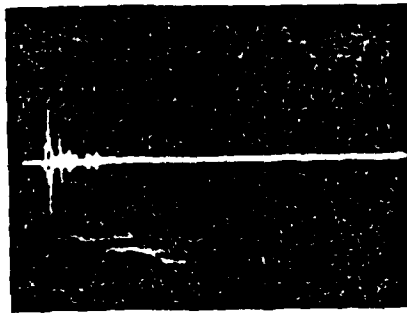


- 6.1 The seismogram envelopes of S waves predicted by the diffusion approximation for the case of $f = 2 \text{ Hz}$, $B_0 = 0.9$ ($Q_1 = 2500$). $\bar{\gamma}$ is the mean scattering angle cosine defined by (6.10).

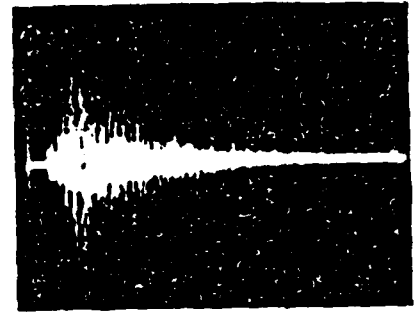


Compressed time-scale records of two of the lunar seismic events believed to be of natural origin recorded at station 12. Z is the vertical component seismometer; X and Y are the horizontal component seismometers. The moonquake, event of 13:09 hr., May 23, 1970, originated within the zone of greatest activity (A_1 zone). The H-phase is prominent on the seismograms from the horizontal component seismometers for category A_1 events. This phase is tentatively identified as the direct shear wave arrival. The event of 8:09 hr., April 8, 1970, is believed to be a meteoroid impact (category C event).

- 6.2 The seismograms of moonquakes. The event on the top is supposed to be a meteoroid impact; the bottom event is believed to be a deep moonquake (from Latham et al., 1971).



(a)



(b)

6.3 The seismograms from the model experiment in laboratory (Dainty et al., 1974).

a) The seismogram with the homogeneous plate.

b) The seismogram when the plate has many grooves as scatterers.

6.4 The band-pass filtered seismograms of A06 ($r = 235$ km, depth = 103 km) for the stations CHS, FRA, JOR and PEN. From top to bottom: $f = 0.375, 0.75, 1.5, 3, 6, 12, 24, 46$ Hz. —————>

6.5 The band-pass filtered seismograms of A15 ($r = 247$ km, depth = 118 km) for the stations CHS, PEN and JOR. From top to bottom: $f = 0.375, 0.75, 1.5, 3, 6, 12, 24, 46$ Hz. —————>

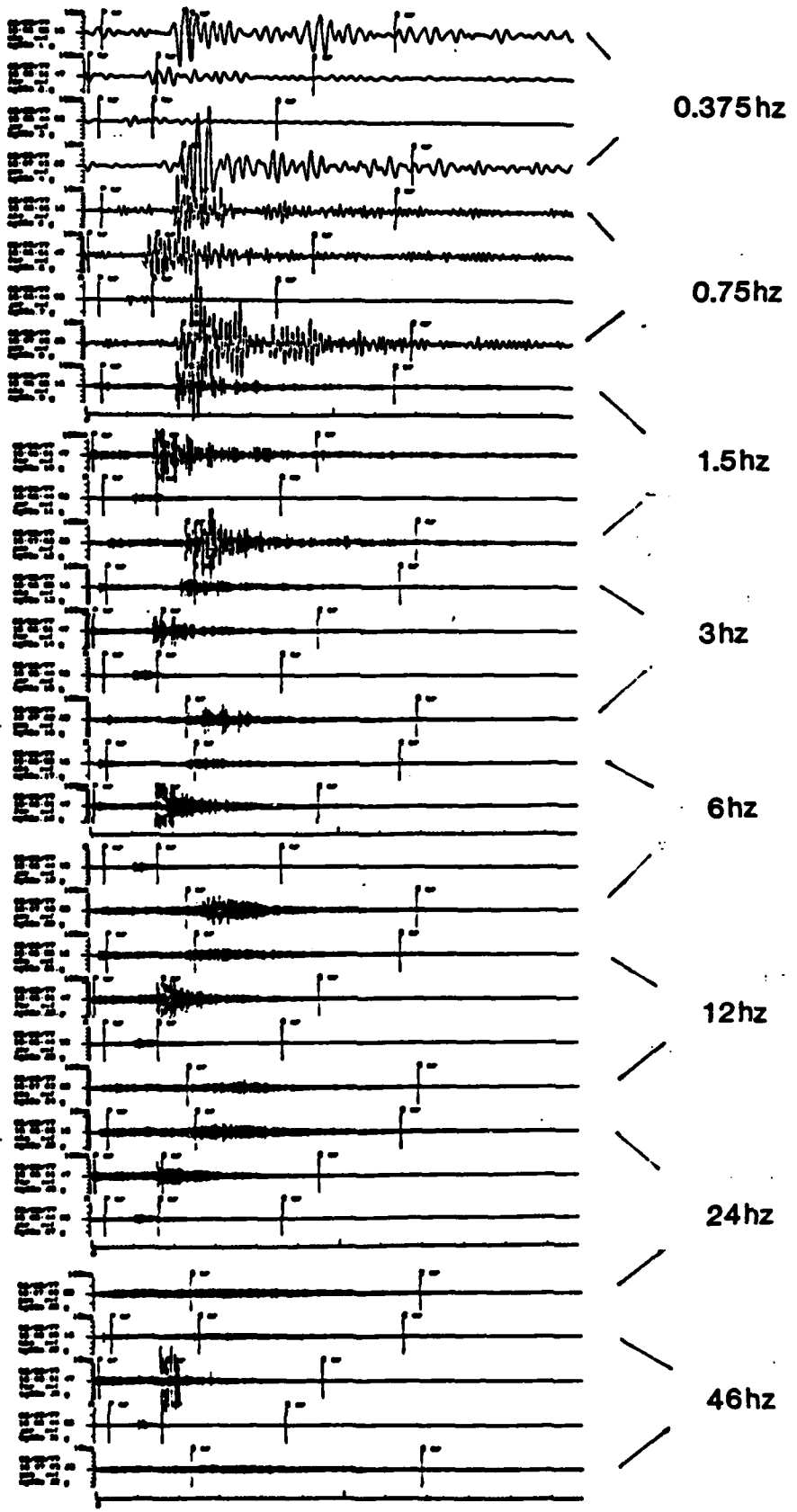
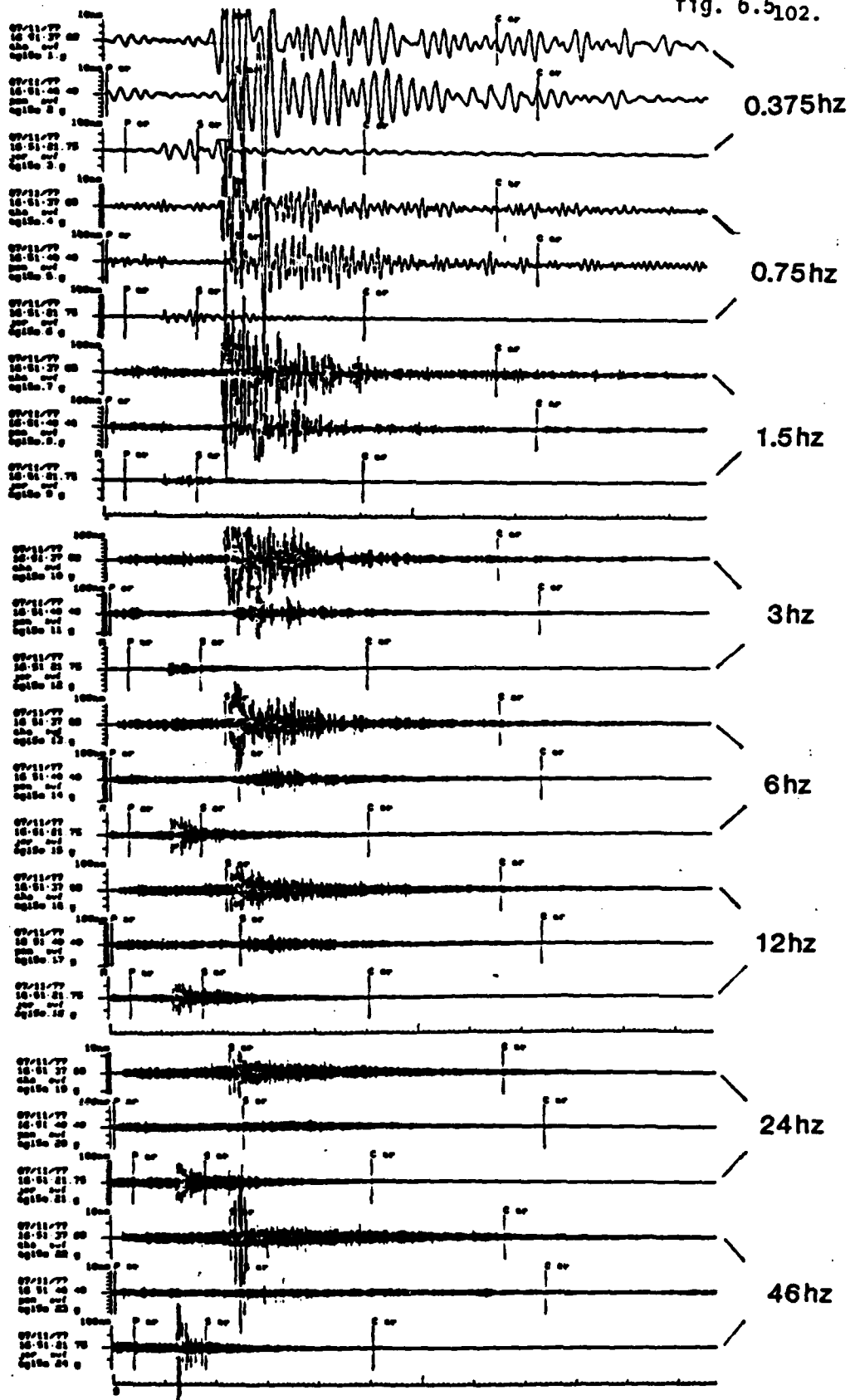
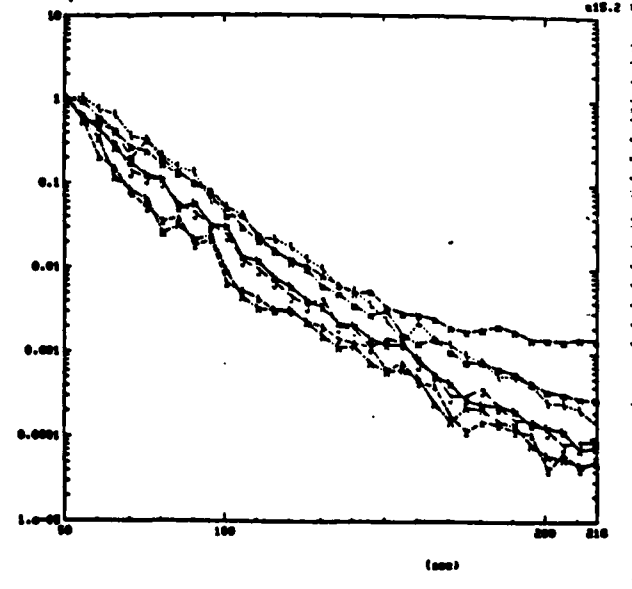
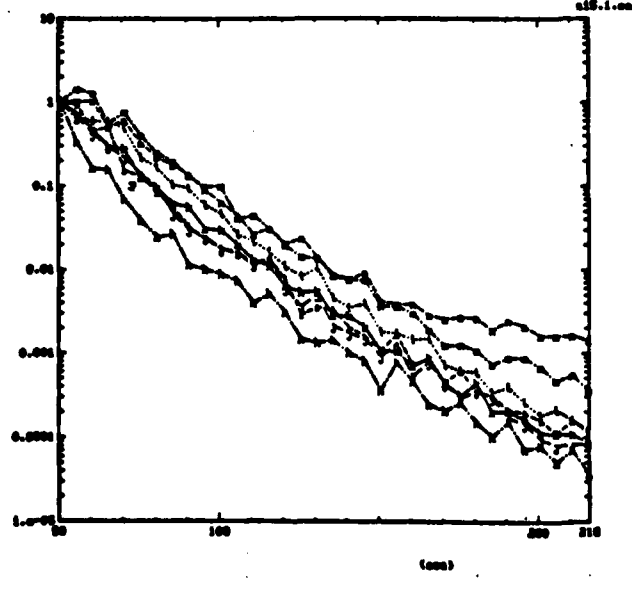
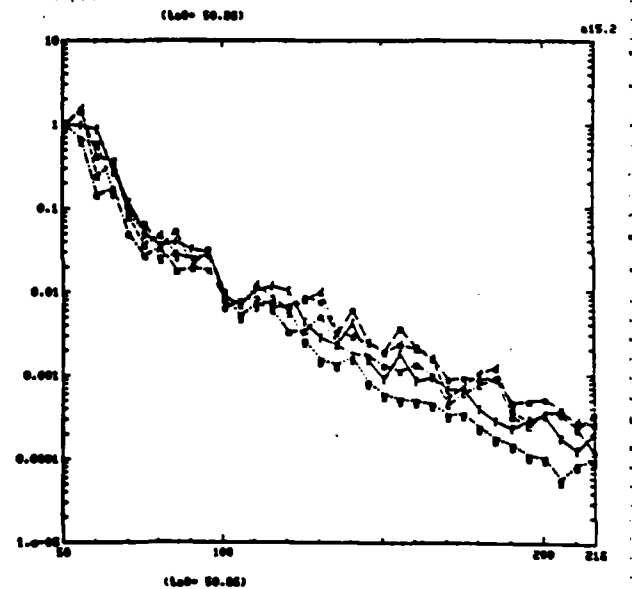
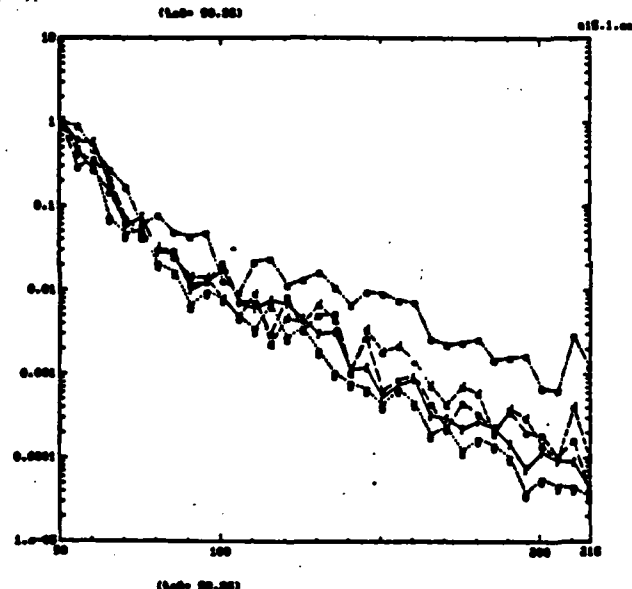
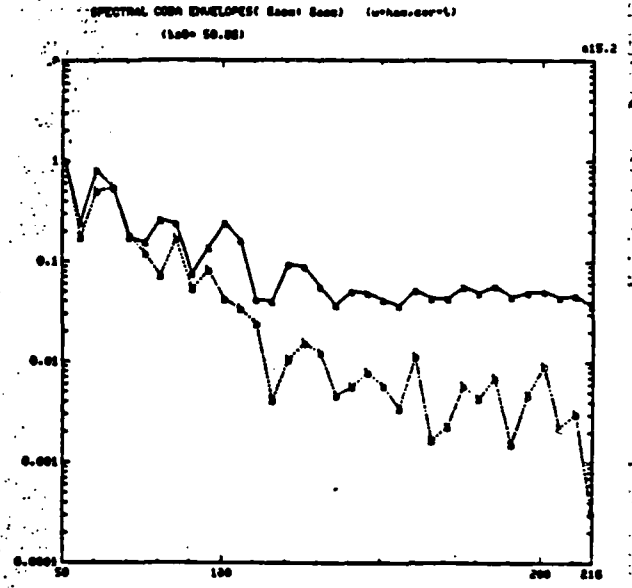
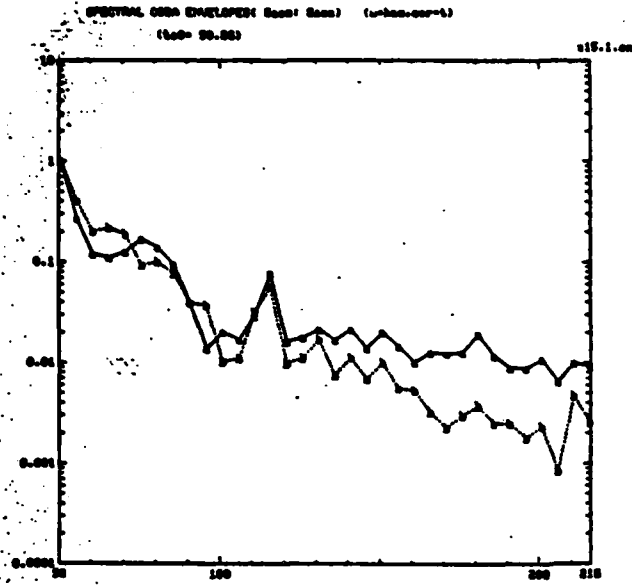


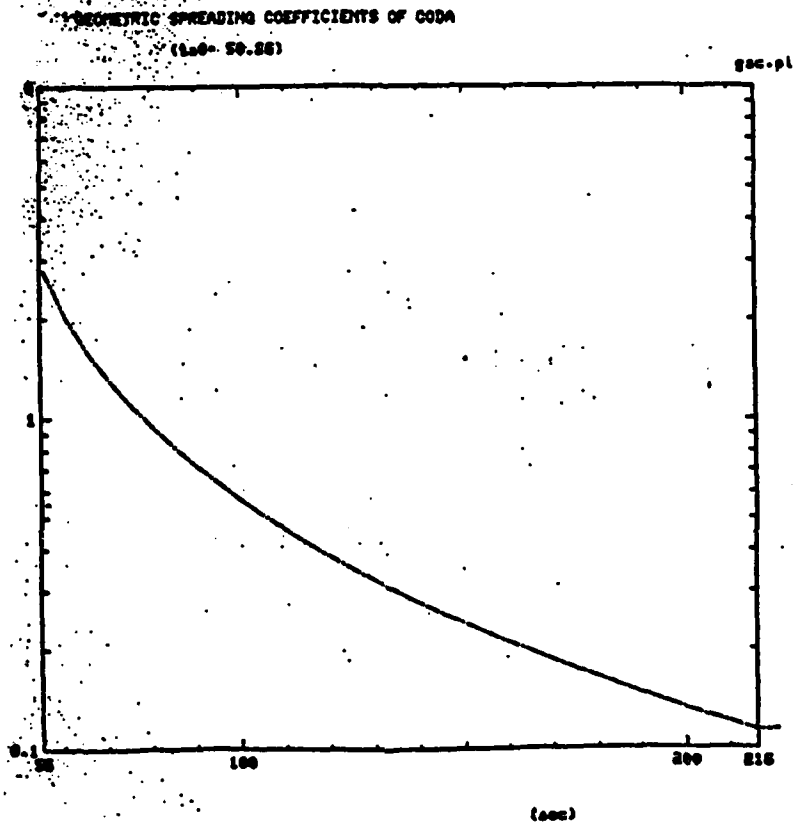
fig. 6.5₁₀₂.





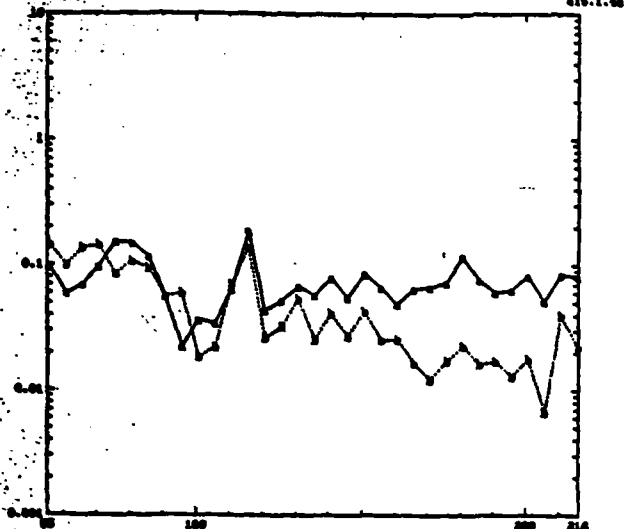
(cm)

(cm)

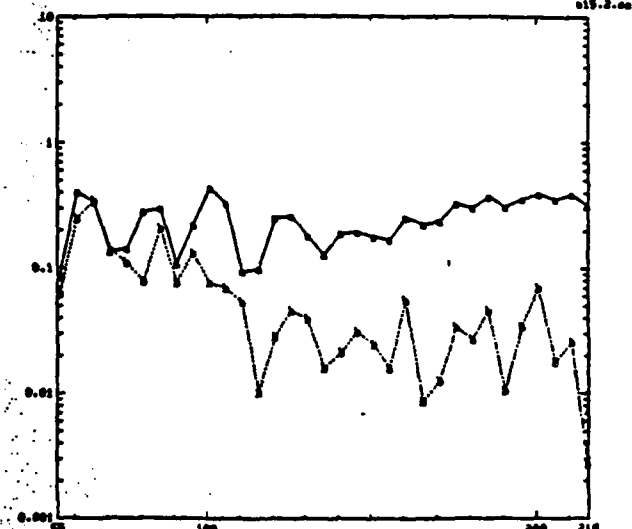


- 6.7 The theoretical envelope decay curve for the single isotropic scattering in a lossless medium according to Sato (1977). The envelope decay is a pure geometric spreading effect. The distance between the source and sensor is taken as 247 km (as the case of A15 to PEN).

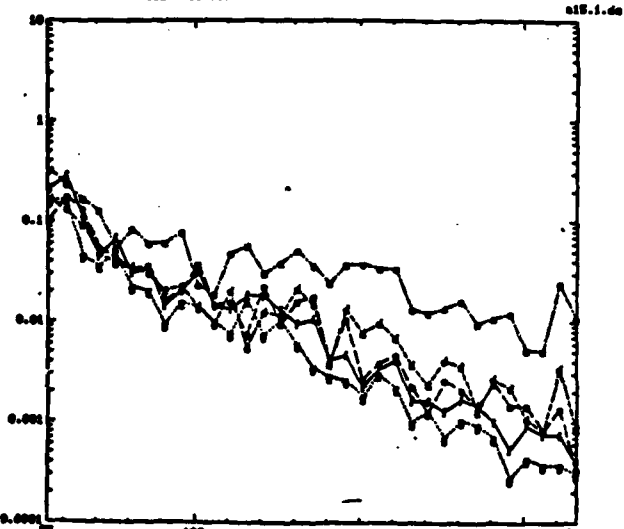
SPECTRAL COBR DECAY (after 600 Jt Soot) (urban,cor=1)
(L=0= 50.00)



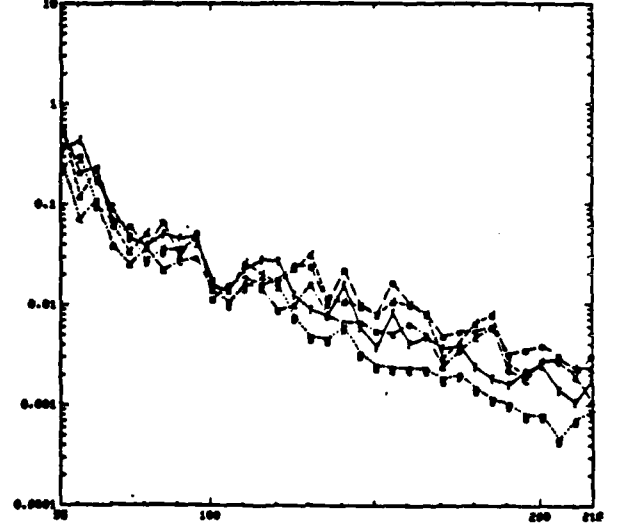
SPECTRAL COBR DECAY (after 600 Jt Soot) (urban,cor=1)
(L=0= 50.00)



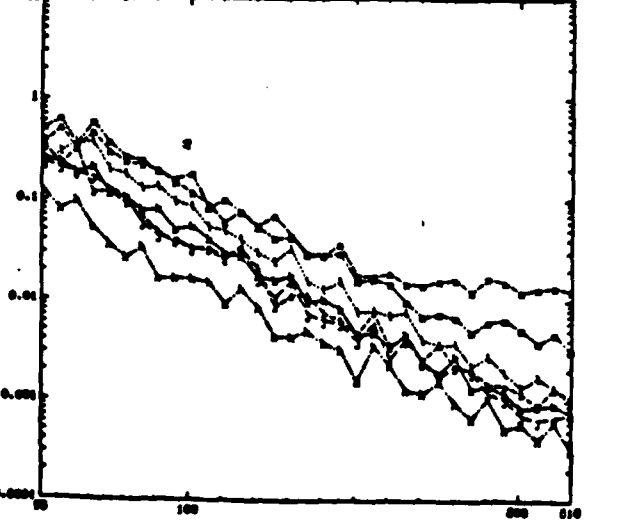
SPECTRAL COBR DECAY (after 600 Jt Soot) (urban,cor=1)
(L=0= 50.00)



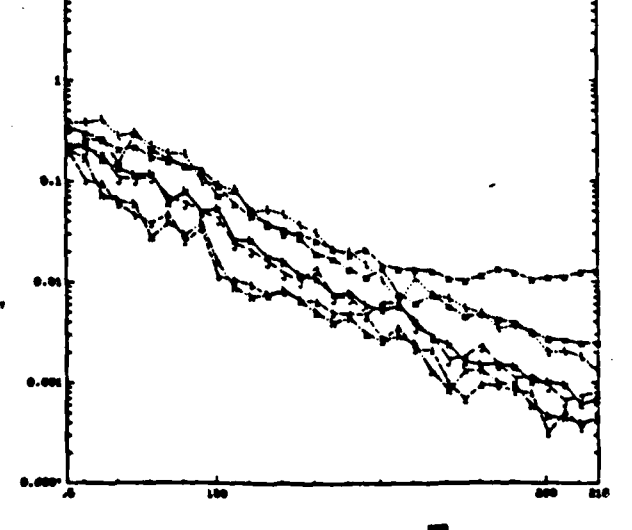
(L=0= 50.00)



(L=0= 50.00)



(L=0= 50.00)



END

FILMED

1-85

DTIC